# Dynamic earthquake source modeling and the study of slab effects

Thesis by

Kangchen Bai

In Partial Fulfillment of the Requirements for the
Degree of
Ph.D. of Geophysics and Seismology


CALIFORNIA INSTITUTE OF TECHNOLOGY
Pasadena, California

2019
Defended June 1st, 2018

Kangchen Bai
ORCID: 0000-0002-9788-6404

# ACKNOWLEDGEMENTS

First of all, I would like to thank my research advisors without whose support this work would never have been possible. Prof. Jean-Paul Ampuero introduced me to the topics of dynamic rupture and earthquake cycle simulation which greatly practiced analytical skills and opened my eye to the area of super computing. His deep understanding of those topics and his brilliant physics intuition enabled us to pierce through the complications and grasp the underlying simplicity. Prof. Don Helmberger introduced me to global seismology. His great enthusiasm and passion on seismograms really inspired me towards making discoveries from waveforms. He also has masterful skills in modeling which I hope that I could have learned more.

I thank my past and present advisory committee: Rob Clayton, Jean-Philippe Avouac and Jennifer Jackson and my minor program advisor Thomas Hou for their helpful advises on course development and guidance at every critical stage of my doctoral study. My attitude goes to Victor Tsai for providing me the experience as a teaching assistant that greatly improve my skills to communicate abstract concepts and make rigorous explanation. I also thank Jean-Philippe Avouac and Zhongwen Zhan for fruitful discussions I had with them on my research projects. I thank Mike Gurnis, Mark Simons, Nadia Lapusta, Joanna Stock for teaching me Geodynamics, Geodesy, Fracture dynamics and Plate tectonics which completes my knowledge in other apsects of Geophysics.

I am grateful to a lot of former seismolab students and postdocs: Daoyuan Sun, Shengji Wei, Han Yue, Dunzhu Li, Yiran Ma, Asaf Inbal, Yingdi Luo, Yihe Huang, Daniel Bowden and Vish Ratnaswamy for their helpful advices on my research and career development. I thank my office mates: Yiran Ma, Semechah Lui, Voonhui Lai, Jorge Castillo, Zhichao Shen and Valere Lambert for a lot of fun chats and discussions. I am fortunate to have Xiaolin Mao as my classmate, together with whom we overcame a lot of difficulties and challenges. I thank my friends who are also pursuing Ph.D.s all around the globe: Xiaopeng Bian, Qingyuan Yang and Hongyu Zeng for their companion during the highs and lows.

I thank Priscilla Mclean, Sarah Gordon, Donna Mireles, Kim Baker-Gatchalian, Rosemary Miller, Michael Black and Naveed Near-Ansari for caring about administrative businesses and computational facilities.

I am deeply indebted to Xiaodong Song, Mingjie Xu and Ning Mi who are my geophysics teachers at Nanjing university for introducing me to the area of geophysics.

My attitude also goes to my mentors in Schlumberger Houston namely, James Xu, Kun Jiao, Xing Cheng, Dong sun and Denes Vigh, with whom I spent two summers doing an intership. Our seamless collaborations led to considerable progress towards new imaging techniques during which I learned a lot of valuable knowledge about seismic imaging and industrial programming.

Finally, I would like to thank my family, my father and mother, my grandmother and my uncle Ben for their unconditional love and support 10,000 km away across the Pacific Ocean during the five years.

# ABSTRACT

In this Thesis, I report my Ph.D. research on two major issues that are devoted towards constructing more realistic earthquake source model using computational tools: (1) constructing physically consistent dynamic rupture models that include complexities in fault geometry as well as heterogeneous stress and frictional properties inferred from observations; (2) study the effect of subducting slab structure on earthquakes that occur inside it with a special focus on the teleseismic waveforms.

Fault step over is one of the most important geometric complexities that control the propagation and arrest of earthquake ruptures. In Chapter 2, we study the role of seismogenic depth and background stress on physical limits of earthquake rupture across fault step overs. We conclude that the maximum step over distance that a rupture can jump is approximately proportional to seismogenic depth. We also conclude that the pre-stress conditions have a fundamental effect on step over jump distance while the critical nucleation size has a secondary effect.

Seismic wave carries information of source as well as structures along the path it travels. It was found that seismic waves generated by shallow events in subduction zones whose ray path coincide with the down going slab structure display waveform complexities that feature multipathing. In Chapter 3, we study deep earthquakes whose depth phases sample the slab structure on their way up to the surface. Differential travel time sP-P analysis shows a systematic decrease of up to 5 seconds from Europe to Australia and then to Pacific which is indicative of a dipping high velocity layer above the source region. Finite-difference simulations showed that a slab shaped structure that follows the Benioff zone at shallow depth and steepens beyond 400 km produces a model that can account for the sP-P differential travel times of 5 seconds for oceanic paths. In Chapter 4, we design a slab operator that can be applied on the 1D synthetics to generate 2D synthetics with slab structure. We hope this operator can be used for generating more accurate Green's functions that could potentially serve earthquake source inversion.

In Chapter 5, we design a dynamic rupture model of the Mw 7.8 Gorkha, Nepal earthquake. We employ a novel approach of integrating kinematic inversion results which provide low frequency stress distribution and stochastic high frequency stress motivated by earthquake cycle models and observations. By doing this, we are able to reproduce the observed frequency dependent rupture processes, in particular the

concentration of high-frequency radiation in the down-dip part of the rupture.

In Chapter 6, I report my on going work on the spectral element method based earthquake cycle simulator. Large scale earthquake cycle simulation with consideration of complicated velocity structure and fault geometry is a great challenge for numerical modeling. I tried to push forward this boundary by extending the existing spectral element earthquake cycle simulator to enable cycle simulations on bi-material faults. This chapter includes a benchmark test in 2D that demonstrates the correctness of this new algorithm and an application of this method on bi-material fault earthquake cycle modeling.

# PUBLISHED CONTENT AND CONTRIBUTIONS

Bai, Kangchen and Jean-Paul Ampuero (2017). "Effect of Seismogenic Depth and Background Stress on Physical Limits of Earthquake Rupture Across Fault Step Overs". In: *Journal of Geophysical Research: Solid Earth* 122.12, pp. 10, 280–10, 298. DOI: 10.1002/2017jb014848. URL: https://doi.org/10.1002/2017jb014848.

Bai and Ampuero co-designed the study. Bai conducted all the 3D dynamic rupture simulations, analyzed the results. Bai and Ampuero contributed to interpreting the results and writing the manuscript.

# TABLE OF CONTENTS

# LIST OF ILLUSTRATIONS

# LIST OF TABLES

*Chapter 1*

# INTRODUCTION

Dynamic earthquake source modeling could provide key information for prediction of large ground motion and long term fault evolution which is very important for hazard analysis. The foundation of dynamic earthquake source modeling was laid by Kostrov (1964), Burridge and Halliday (1971), Madariaga (1976), and Das and Aki (1977a) who treat the modeling problem as an elastodynamic problem governed by elastic wave equation with a predefined discontinuous plane inside the model domain. The relative motion across this discontinuous plane is governed by friction laws that relate the relative motion to stress (boundary traction). With input from laboratory rock friction experiments (Brace and Byerlee, 1966; Palmer and Rice, 1973; Dieterich, 1994) and earthquake field observations (Stuart, 1979; Stuart and Mavko, 1979) more realistic and robust frictional models (Andrews, 1976; Ruina, 1983) have been included into the simulations. With the advance of both modeling techniques and frictional models, researchers are able to answer some basic questions of earthquake mechanics such as what controls the earthquake rupture speed (Andrews, 1976; Day, 1982; Dunham, 2007) and what controls the high frequency ground motion (Madariaga, 1977; Madariaga, 1983; Madariaga et al., 2006).

With the accumulation of earthquake observations and the fast deployment of super-computing power during the years, numerical simulations of large earthquakes with fine scale details are now possible. The spectral element method was introduced into computational seismology by Komatitsch and Vilotte (1998) and was later developed into a scalable parallel computing software package (Komatitsch and Tromp, 2002) that can model elastic wave propagation within the real 3D earth which further leverages the immense power of GPU computing (Komatitsch et al., 2010). Kaneko et al. (2008) and Galvez et al. (2014) developed a dynamic fault friction solver to couple with this elastic wave propagation software enabling large scale rupture simulations with realistic 3D fault geometry and velocity structure.

Of those fine scale details that influence earthquake rupture propagation, step-over is one of the most common phenomenon that feature large earthquakes. Earthquakes can grow large by jumping from one fault strand to another separated by step-overs.

A lot of modeling work has been done on this topic following the pioneering effort of Harris and Day (1999).

In Chapter 2, I did a series of numerical simulations to probe the factors that control the jump of step-overs for large strike slip earthquakes. In particular, special attention is paid to one controlling factor that has not been studied extensively which is the seismogenic zone depth. If every rupture parameter scales with seismogenic depth, so should the critical step-over width. However, there are some dynamic quantities that don't necessarily scale with seismogenic depth such as the critical nucleation size. How will that affect the scaling relation between step-over width and seismogenic depth? We addressed this issue by exploring the parameter space spanned by these quantities i.e. finding a critical step-over distance for each plausible parameter combination. Our work shows that the scaling relation is approximately true for a large range of parameter combinations. While the critical nucleation size plays a secondary role on the fundamental scaling relation.

In Chapter 5, we conduct 3D dynamic rupture simulations and some following research on the source processes of the Mw7.8 Gorkha earthquake. By incorporating initial static stress from finite fault inversion results and superimposing on it a stochastic stress field at the down-dip portion inspired by the earthquake cycle simulation, we built a dynamic source model whose rupture process is spontaneously governed by friction law. Our dynamic rupture model was able to reproduce the earthquake source moment rate spectra and near field strong motion acceleration spectra that fits the observed data spectra better than the kinematic finite fault model. We also study the resolution issue of the back-projection on high frequency radiations using tele-seismic signals. We found that the back-projection with beam-forming technique is only able to resolve high frequency radiation from a rough rupture that has either rapid varying rupture speed or amplitude but not a smooth rupture.

In Chapter 6, I report my recent work on the spectral element method based earthquake cycle simulator. I extended the work of Kaneko et al. (2011) to enable the simulation of mode II rupture with asymmetric material properties across the fault plane by proposing and implementing a solver for a more generalized fault boundary value problem. I benchmarked this solver with the original work of Kaneko et al. (2011) which confirmed the correctness of the new method. The new method can be applied to solve the problem of bimaterial fault evolution. The Preliminary Reference Earth Model (Dziewonski and Anderson, 1981) provides physics properties of the earth interior such as longitudinal wave (P wave ) speed, shear wave (S wave)

speed and density as a function of the earth radius. The model has been widely used in applications such as locating earthquakes. However, the oversimplified one-dimensional model may not be suitable for locating subduction zone earthquakes. Since the subducted slab is cooler than ambient mantle, it brings in a dipping high velocity structure into the 1D velocity structure which substantially changes the travel time and waveform when the source is inside the slab. In Chapter 3, we study the effect of slab structure on the depth phases, i.e. seismic wave from deep event traveling up to the earth surface taking route inside the slab body. Our differential travel time approach excludes the effect of velocity anomaly on the traveling path except the segment within the slab. In Chapter 4, we develop a slab operator for shallow events occurring inside the slab structures. Convolving 1D synthetics with this operator will generate the correct effect of the slab structure including travel time change and waveform complexity.

*Chapter 2*

# EFFECT OF SEISMOGENIC DEPTH AND BACKGROUND STRESS ON PHYSICAL LIMITS OF EARTHQUAKE RUPTURE ACROSS FAULT STEP-OVERS

Bai, Kangchen and Jean-Paul Ampuero (2017). "Effect of Seismogenic Depth and Background Stress on Physical Limits of Earthquake Rupture Across Fault Step Overs". In: *Journal of Geophysical Research: Solid Earth* 122.12, pp. 10, 280–10, 298. DOI: 10.1002/2017jb014848. URL: https://doi.org/10.1002/2017jb014848.

# ABSTRACT

Earthquakes can rupture geometrically complex fault systems by breaching fault step-overs. Quantifying the likelihood of rupture jump across step-overs is important to evaluate earthquake hazard and to understand the interactions between dynamic rupture and fault growth processes. Here we investigate the role of seismogenic depth and background stress on physical limits of earthquake rupture across fault step-overs. Our computational and theoretical study is focused on the canonical case of two parallel strike-slip faults with large aspect ratio, uniform pre-stress and uniform friction properties. We conduct a systematic set of 3D dynamic rupture simulations in which we vary the seismogenic depth, step-over distance and initial stresses. We find that the maximum step-over distance $H_c$ that a rupture can jump depends on seismogenic depth $W$ and strength excess to stress drop ratio $S$, commonly used to evaluate probable rupture velocity, as $H_c \propto W/S^n$, where $n = 2$ when $H_c/W < 0.2$ (or $S > 1.5$) and $n = 1$ otherwise. The critical nucleation size, largely controlled by frictional properties, has a second-order effect on $H_c$. Rupture on the secondary fault is mainly triggered by the stopping phase emanated from the rupture end on the primary fault. Asymptotic analysis of the peak amplitude of stopping phases sheds light on the mechanical origin of the relations between $H_c$, $W$ and $S$, and leads to the scaling regime with $n = 1$ in far field and $n = 2$ in near field. The results suggest that strike-slip earthquakes on faults with large seismogenic depth or operating at high shear stresses can jump wider step-overs than observed so far in continental inter-plate earthquakes.

## 2.1 Introduction

Earthquakes often occur on fault systems with multiple strands separated by step-overs. These discontinuities can act as barriers that arrest earthquakes ruptures, but this is not always the case: ruptures can also jump across step-overs. For example, the 2013 $M_w$7.7 Balochistan earthquake rupture stopped at a dilational step-over at its southern end (Zhou et al., 2016), whereas the 1992 $M_w$7.3 Landers earthquake breached four major step-overs within the Eastern California Shear Zone (Sieh et al., 1993) .

Understanding the role of step-overs on rupture propagation and arrest has both practical and fundamental significance. An important mechanism by which earthquakes become large is by breaking multiple fault segments, despite the structural barriers that separate them (Meng et al., 2012; Hamling et al., 2017; Sieh et al., 1993). In seismic hazard analysis, the likelihood of multiple fault segments rupturing during a single earthquake is a crucial consideration to determine the largest expected magnitude in a complex fault system (Field et al., 2014). An important goal is to establish quantitative relations between the efficiency of step-over jumps and the geometrical properties of step-overs. Efforts to achieve this goal empirically have yielded seminal results (e.g. Wesnousky, 2006; Wesnousky and Biasi, 2011; Biasi and Wesnousky, 2016) but are ultimately limited by the small number of earthquakes with sufficient rupture and fault observations. Mechanical models can offer a complementary support to such efforts, for instance by providing mechanically-motivated functional forms to guide the development of empirical relations and physically expected bounds to supplement empirical models.

Step-overs and other geometrical features of faults are also the subject of basic research, especially on the relation between the short time scales of dynamic rupture and the long time scales of fault growth. The dynamic generation of damage and branching during earthquake rupture contributes to the long-term evolution of fault zones (Cooke, 1997; Herbert et al., 2014; Ampuero and Mao, 2017). One mechanism of fault growth operates by coalescence of multiple fault segments during which the step-overs are breached (Joussineau and Aydin, 2007). If the two neighboring fault segments interact strongly throughout their earthquake cycles, simultaneous modeling of the whole fault system is required.

Continental strike-slip earthquakes rarely manage to jump step-overs larger than about 5 km (Wesnousky, 2006; Xu et al., 2006; Elliott et al., 2009). This has been also observed in dynamic rupture simulations (Harris et al., 1991; Harris and Day,

1999; Oglesby, 2005; Lozos et al., 2014a; Lozos et al., 2014b), even if the second fault segment is very close to failure. A critical step-over distance $H_c$ = 5 km has been incorporated in seismic hazard assessment models such as the The Third Uniform California Earthquake Rupture Forecast (Field et al., 2014).

However, some recent earthquakes may have jumped step-overs much wider than 5 km. The 2010 $M_w$-7.2 El Mayor-Cucapah earthquake ruptured a 120 km long multi-segment fault jumping through an apparent step-over of more than 10 km with the possible aid of intermediary fault segments (Wei et al., 2011; Oskin et al., 2012) . During the 2012 $M_w$ 8.6 Indian Ocean earthquake, the rupture propagated through a complicated orthogonal conjugate fault system. In the late part of this earthquake, back-projection rupture imaging revealed a step-over jump as wide as 20 km (Meng et al., 2012). The 2016 $M_w$ 7.8 Kaikoura, New Zealand earthquake made an apparent jump through a compressional step-over of 15 km (Hamling et al., 2017) taking advantage of several linking faults which have not been previously mapped for hazard assessment. A common feature of the latter two events is their particularly large rupture depth extent, compared to other strike-slip events. The Indian Ocean earthquake has a centroid depth beyond 25 km; its rupture penetrated into the upper mantle. These observations call for a re-examination of the factors affecting the critical step-over distance. Existing models of the efficiency of step-over jumps do not account for the role of key observable physical parameters, such as the seismogenic depth, and poorly constrained frictional parameters, such as fracture energy. With ongoing advance in earthquake data gathering and source inversion methods, this information can be obtained and help generating a more accurate model.

In this computational and theoretical study, we determine key physical parameters that control the critical step-over distance in large strike-slip ruptures using numerical simulations and asymptotic analysis. We keep the model as simple as possible so that we can use fracture mechanics arguments to gain physical insight on the numerical modeling results.

## 2.2 Model

We consider two vertical, parallel strike-slip faults in a 3D homogeneous isotropic elastic half-space, as depicted in Figure 2.1. The elastic medium has density 2700 kg/m$^3$, P wave speed 6000 km/s and S wave speed 3464 km/s. The faults have length $L$, seismogenic width $W$, step-over distance $H$ (distance between the

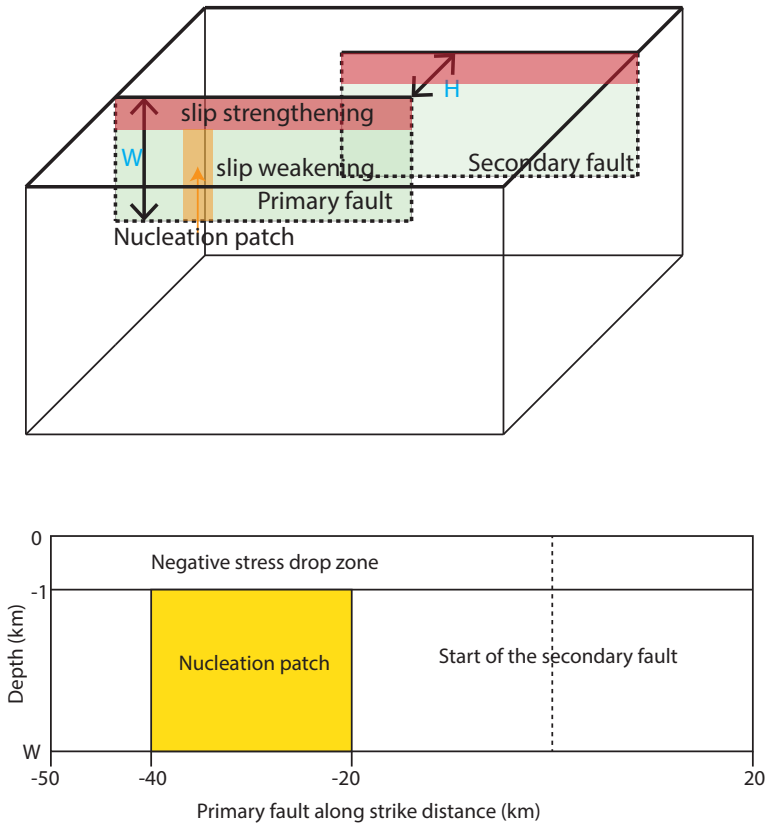


Figure 2.1: Canonical model of two parallel, vertical strike-slip faults with a step-over. Top: 3D view. The step-over distance is $H$ and seismogenic depth is $W$. Bottom: Side view. Nucleation is enforced on the primary fault in a rectangular area that covers the whole seismogenic depth. A shallow zone of negative strength drop is prescribed.

two fault traces), and overlapping length $D$. In our simulations, $L$ and $D$ are fixed while other parameters are variable. We focus on large-magnitude strike-slip earthquakes whose rupture area have large aspect ratio $L/W$. The regional stress is assumed homogeneous, resulting in a uniform normal stress of $\sigma_0 = 150$ MPa on the faults and uniform shear stress $\tau_0$ whose value is a model parameter. The faults are governed by the linear slip-weakening friction law (Ida, 1972; Palmer and Rice, 1973; Andrews, 1976), with uniform static and dynamic friction coefficients $\mu_s = 0.677$ and $\mu_d = 0.373$, respectively, and critical slip weakening distance $D_c = 0.5$ m.

Surface-induced supershear rupture (Kaneko et al., 2008) and nucleation at the free surface on the secondary fault (Harris and Day, 1999) can substantially increase $H_c$ for supershear ruptures (Hu et al., 2016, see also section 2.3). These two phenomena have been reported in numerical simulations but not in earthquake observations. They are thus suppressed in this study by setting a negative strength drop in the top 1 km of both faults. A linear slip-weakening friction with negative strength drop mimics rate-and-state friction with velocity strengthening behavior which Kaneko et al. (2008) adopted to suppress the free surface effect. Laboratory experiments indicate that unconsolidated fault gouge at shallow depth exhibit velocity-strengthening frictional properties (Marone and Scholz, 1988; Ikari et al., 2009).

Earthquake ruptures with large aspect ratio eventually turn into pulse-like ruptures because of the no-slip constraint at the bottom of the seismogenic zone (Day, 1982; Ampuero and Mao, 2017). Their rise time is controlled by stopping phases emanating from the lower limit of the seismogenic layer. Their rupture fronts tend to become straight and vertical at large propagation distance. When such a vertical rupture front suddenly changes speed, especially when it hits the vertical edge of the fault and comes to a stop, it generates stronger coherent high-frequency radiation than for instance a circular front (Madariaga et al., 2006). The short rise time of a pulse-like rupture further enhances its high-frequency radiation. Hence the large aspect ratio of large ruptures exacerbates the dynamic stresses that promote step-over jumps. However, theoretically, when $L/W$ is so large that the rupture becomes a stationary pulse, the radiation strength of the stopping phase no longer depends on rupture length (Day, 1982). Here we are interested in upper bounds on critical step-over distance, hence we consider the limiting case of very elongated ruptures and adopt an artificial nucleation procedure that favors straightness of the rupture front.

To facilitate the application of our numerical model to different scales, we introduce the following dimensionless quantities. The ratio of strength excess to stress drop, as introduced by (Das and Aki, 1977b) ,

$$S = \frac{\mu_s \sigma_0 - \tau_0}{\tau_0 - \mu_d \sigma_0}, \tag{2.1}$$

quantifies the relative fault pre-stress level. The seismogenic depth is characterized by the ratio $W/L_c$, where the length

$$L_c = \frac{\mu D_c}{\sigma_0(\mu_s - \mu_d)} \tag{2.2}$$

is representative of the static process zone size, where shear modulus $\mu = 32.4$ GPa. We fix the ratio $L/L_c$ to a large enough value to allow the rupture on the primary fault evolve towards a nearly constant speed. Increasing the rupture acceleration distance has been previously found to increase the critical step-over distance (Hu et al., 2016). This can be explained by the fact that before reaching stationary propagation, the peak slip rate of the slipping pulse keeps increasing (Day, 1982), making the potential stopping phase stronger as fault length increases.

Ruptures are initiated by an artificial nucleation procedure intended to minimize the curvature of the primary rupture front, which facilitates step-over jumps. We abruptly and simultaneously reduce the coefficient of friction to its dynamic value within a vertical band extending through the full seismogenic thickness on the primary fault . The horizontal width of this initiation band is set to 20 km in this study by trial and error to make sure that the rupture with the largest $S$ ratio considered here ($S = 4$) can successfully nucleate on the primary fault. However, a preferred approach to set the size of the initiation zone can be derived from the accurate theoretical estimates developed for nucleation by over-stressed regions by Galis et al. (2014).

The step-over geometry is characterized by the dimensionless step-over distance $H/W$ and overlap distance $D/L$. A previous study has shown a positive relation between the critical step-over distance $H_c$ and $D$ (Harris and Day, 1999). We fix $D/L$ to a large value (0.4) to ensure that the secondary fault is fully exposed to the stress change caused by the primary rupture. Our choices of values for $L/L_c = 140$ and $D/L = 0.4$ favor rupture across the step-over and are intended to yield an upper bound estimate of $H_c/W$.

Dimensional analysis of this basic problem indicates a relation between dimensionless quantities of the form

$$H_c/W = f(S, W/L_c) \tag{2.3}$$

Here we conduct a systematic set of 3D dynamic rupture simulations to characterize the yet unknown function $f$. We scan a range of values of $H/W$ and $W/Lc$ by varying $W$ and $H$ while holding $L_c$ fixed. For each pair $(H/W, W/L_c)$ we use binary search to find the maximum $S$ ratio ($S_c$) that allows the step-over to be breached.

The main focus of this study is on sub-Rayleigh ruptures (propagating slower than Rayleigh wave speed). For super-shear ruptures (propagating faster than S wave speed), we did not fully explore the parameter space. Super-shear ruptures account

for a small amount of events in earthquake observations and their dynamics can be more complicated. We nevertheless considered several super-shear cases for comparison with their sub-Rayleigh counterparts.

We use the spectral element method software SPECFEM3D (Komatitsch and Tromp, 1999). To enable this work, we extended the dynamic rupture solver implemented by Galvez et al. (2014) to take advantage of GPU acceleration (Komatitsch et al., 2010) which led to a decrease of 90% of the total computation time on Caltech's FRAM cluster. We use 5-th order spectral elements. Far from the fault we use a coarse mesh with element size of 800 m. Within 10 km of the fault plane we refine the mesh down to an element size of 266 m on the fault, equivalent to an average node spacing of 66.5 m. The mesh resolves well the static process zone size $\approx L_c$ (355 m).

## 2.3 Simulation results

### Effects of seismogenic depth $W$ and strength excess ratio $S$ on critical step-over distance

We vary $W$ from 5 to 20 km with increments of 2.5 km and vary $H$ from 0.5 to 3.5 km with increments of 0.5 km. This range of values covers the representative range of most strike-slip earthquakes. For each $(W, H)$ pair, the maximum $S$ value enabling step-over jumps is determined by binary search with an accuracy of 0.1 MPa. The resulting critical $S_c$ values for all $W$ and $H$ are shown in Figure 2.2.

The complete set of simulations includes both ruptures that propagated at sub-Rayleigh speed and at super-shear speed on the first fault. For a given $(W, H)$ pair, as $S$ is decreased the following regimes are observed in most cases: sub-Rayleigh rupture without step-over jump, sub-Rayleigh with jump, super-shear without jump, and finally super-shear with jump. We then report in Figure 2.2 the two maximum $S$ values that yield a step-over jump in sub-Rayleigh ruptures (circles) and in super-shear ruptures (diamonds), respectively. There are also cases where one regime is missing and the sequence at decreasing $S$ is: sub-Rayleigh without jump, super-shear without jump, and super-shear with jump. We did not determine $S_c$ for these cases (open circles in Figure 2.2).

A characteristic pattern is found in the step-over jump behavior of sub-Rayleigh ruptures. The $S_c$ values for the sub-Rayleigh cases are plotted separately in Figure 2.3, which points to a relation of the form $H/W \approx f(S_c)$.

The slope of the contours decreases with $S_c$, indicating that $f$ is a decreasing

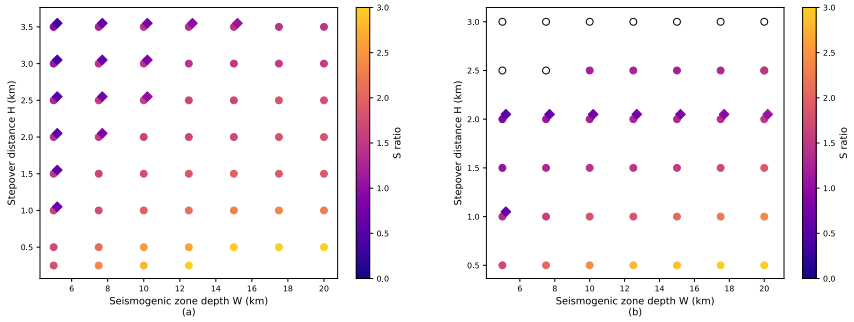


Figure 2.2: Critical values of the ratio of strength excess to stress drop, $S$, that allows ruptures to jump (a) compressional and (b) dilational step-overs with different seismogenic depth $W$ and step-over distance $H$. Each symbol is the result of a suite of simulations with fixed $H$ and $W$, but varying $S$ until the maximum $S$ value required for step-over jump is found. This critical $S$ value is reported by colors. Two different symbols indicate the rupture speed regime on the first fault: sub-Rayleigh (circles) or super-shear (diamonds). Open circles are cases in which only super-shear ruptures can jump through the step-over; we did not determine the critical $S$ for those cases.

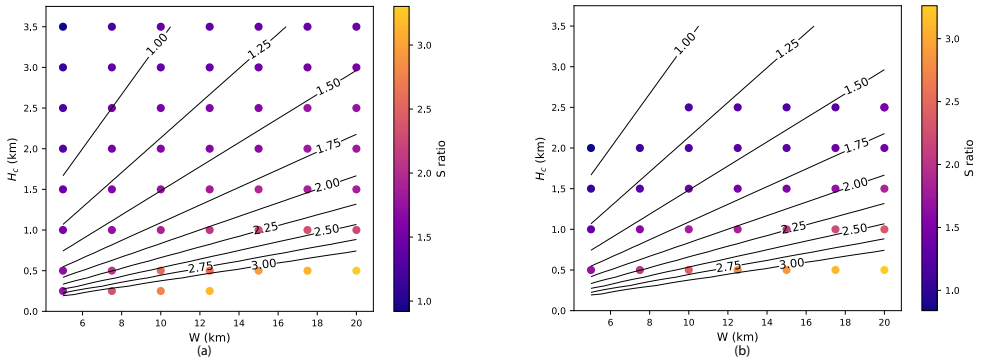


Figure 2.3: Critical step-over distance $H_c$ for sub-Rayleigh ruptures as a function of seismogenic depth $W$ and strength excess ratio $S$ for (a) compressional and (b) dilational step-overs. The solid lines are not contours generated from simulation data, but the contours of critical $S$ predicted by a relation $H_c/W = 0.3/S^2$ inspired by our near-field theory and constrained by our simulation data. They serve as a visual guide here. The contours of $S_c(W, H)$ are roughly linear, pointing to a relation of the form $H/W \approx f(S_c)$.

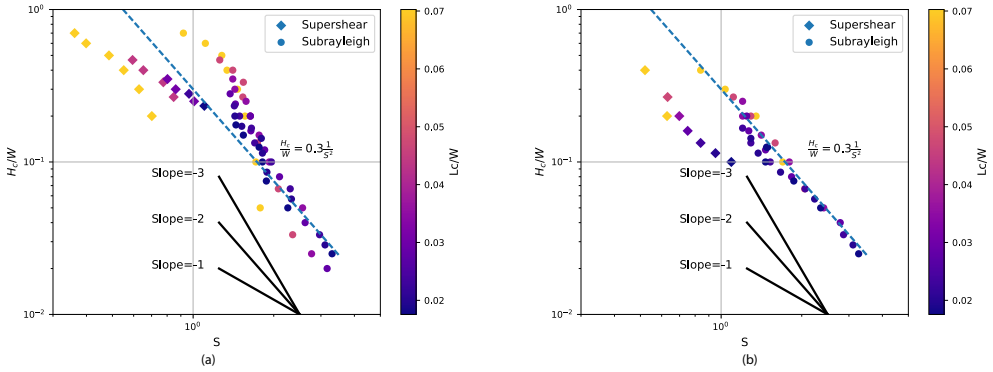


Figure 2.4: Relation between critical step-over distance normalized by seismogenic depth, $H_c/W$, and strength excess $S$ in (a) compressional and (b) dilational step-overs. Simulations span a range of normalized nucleation sizes $L_c/W$ (indicated by colors). Cases with sub-shear and super-shear ruptures on the second fault are distinguished by symbols (see legend). For compressional step-overs, the simulation results are consistent with an inverse quadratic relation $H_c/W \propto 1/S^2$ at large $S > 2$ and an inverse linear relation $H_c/W \propto 1/S$ at small $S < 1.5$. The linear regime has two branches corresponding to sub-Rayleigh and super-shear ruptures on the second fault. For dilational step-overs, the results are consistent with the quadratic relation and also display sub-Rayleigh and super-shear branches. In both compressional and dilational step-overs, sub-Rayleigh ruptures have larger $H_c$ than super-shear ruptures at given $S$. Small values of $L_c/W$ favor super-shear. For a given $S$ value, faults with smaller $L_c/W$ can jump wider step-overs.

function. This result can be re-interpreted as a relation between the critical step-over distance $H_c$ and $W$ for a fixed $S$ value: $H_c/W \approx f(S)$, in which the ratio $H_c/W$ is lower for larger $S$.

Further quantitative examination of the simulation results reveals the dependence of $H_c/W$ on $S$ and $L_c/W$. Based on the results presented in Figure 2.2 and following the dimensional analysis leading to equation 2.3, we present in Figure 2.4 the dependence of the ratio $H_c/W$ on $S$ and $L_c/W$.

In compressional step-overs, we find that $H_c/W$ is roughly proportional to $1/S^2$ when $S$ is large. At low $S$ the sub-Rayleigh and super-shear cases are clearly separated: for a given $S$ value, sub-Rayleigh ruptures have larger $H_c$ than super-shear ruptures. The super-shear subset has $H_c/W$ roughly proportional to $1/S$, and the sub-shear subset shows a hint of a similar trend at the lowest $S$ values. The boundary between the $1/S^2$ and $1/S$ regimes is close to $S = 1.5$ and $H_c/W = 0.2$. In dilational step-overs, the $H_c/W \propto 1/S^2$ regime is also very clear, even within the super-shear subset, but

not the $1/S$ regime. There are fewer cases in our dilational step-over simulations where rupture breaches a step-over wider than 0.2 $W$, so we cannot discard that the inverse linear regime exists outside the parameter ranges we explored. Also in dilational step-overs, for a given $S$ value sub-Rayleigh ruptures have larger $H_c$ than super-shear ruptures. The simulation results at small $H_c/W$ or large $S$ in both compressional and dilational step-overs are adequately represented by the relation $H_c/W = 0.3/S^2$ (dashed lines in Figure 2.4). There is a slightly larger $H_c/W$ on compressional step-overs than on dilational ones, which is consistent with previous findings (Hu et al., 2016).

**Effect of $L_c$ on critical step-over distance and rupture speed**

The ratio $L_c/W$ modulates the relation between $H_c/W$ and $S$ such that for a given $S$, larger $L_c/W$ gives smaller $H_c/W$ (Figure 2.4). The mechanism underlying this observation is that, because the process zone scale $L_c$ is also related to a critical nucleation size (Uenishi and Rice, 2003; Ampuero et al., 2002), a smaller $L_c/W$ facilitates rupture nucleation on the secondary fault.

Apart from a nucleation effect, $L_c$ also affects $H_c$ by affecting the terminal rupture speed on the primary fault. The terminal speed of sub-Rayleigh ruptures on the primary fault depends on $Lc/W$ and $S$. More specifically, it depends on the ratio of fracture energy $G_c = \frac{1}{2}\sigma_0(\mu_s - \mu_d)D_c$ to static energy release rate $G_0 \approx \frac{W\Delta(\tau_0 - \mu_d\sigma_0)}{2\mu}$, which is proportional to $(1+S)^2 L_c/W$. The smaller the ratio $G_c/G_0$ is, the larger the terminal rupture speed can be. In Figure 2.5 we show that the relation between $V_r$ and $G_c/G_0$ obtained in our simulations is consistent with the theoretical expectation from fracture dynamics (Weng and Yang, 2017).

A more prominent effect of $L_c$ on step-over jumps is related to its effect on super-shear transitions. The critical $S$ ratio necessary for super-shear transition increases as $W/L_c$ increases, consistently with results of previous 3D studies (Madariaga and Olsen, 2000; Dunham, 2007). Previous numerical simulations (Lozos et al., 2014a; Hu et al., 2016) have shown that super-shear ruptures can breach a wider step-over than sub-Rayleigh ruptures. In particular, when the $S$ ratio decreases to around 0.45, a step-over wider than 10 km can be breached by ruptures that have undergone super-shear transition assisted by free-surface effects (Hu et al., 2016). On the contrary, in our simulations with free surface effect suppressed by a shallow layer of negative stress drop, super-shear ruptures have shorter $H_c$ than sub-Rayleigh ruptures at given $S$ (Figure 2.4). We observed that during super-shear transition, the

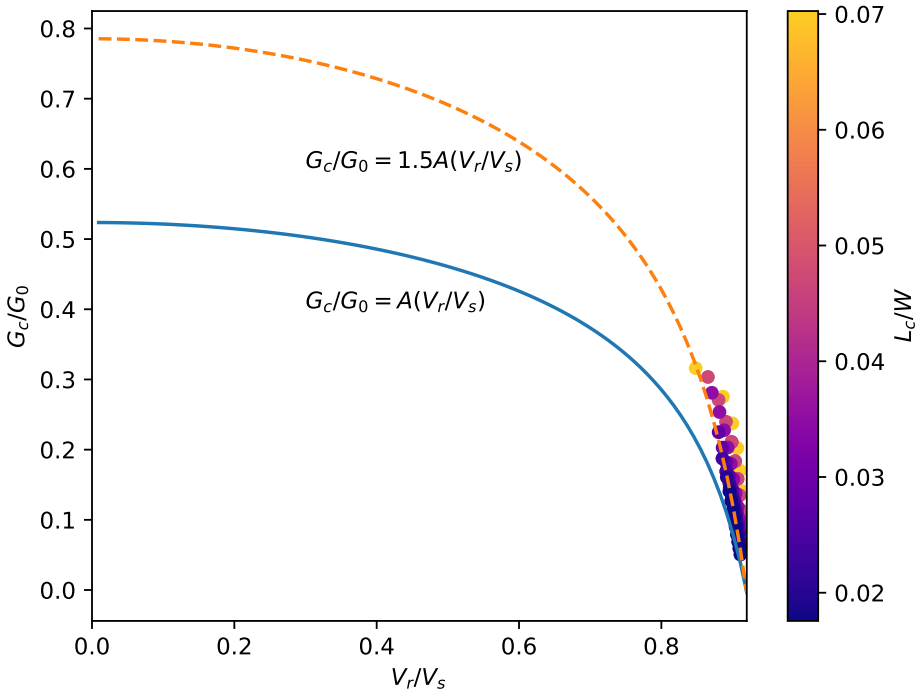


Figure 2.5: Final rupture speed on the first fault as a function of the ratio between fracture energy $G_c$ and static energy release rate $G_0$. Rupture speed $V_r$ is normalized by shear wave speed $V_S$. The blue solid line is the theoretical curve for 2D mode II cracks with constant rupture speed. A constant factor of 1.5 is introduced to account for 3D effects, such as curvature of the rupture front.

rupture front splits into a super-shear rupture front and a sub-Rayleigh rupture front following the Burridge-Andrews mechanism (Andrews, 1976). These two fronts are weaker than the original sub-Rayleigh front, hence less efficient at inducing step-over jumps (Figure 2.6).

For most values of $H$, we find two critical $S$ ratios for step-over jump, a larger $S_c$ for sub-Rayleigh ruptures and a smaller one for super-shear ruptures. However, there are cases in the dilational step-overs where the step-over jump happens only when rupture on the first fault is super-shear. In these cases, there is only one critical $S$ ratio, the one corresponding to super-shear ruptures (open circles in Figure 2.2).

**Effect of dynamic stresses**

In principle, both static and dynamic stress transfer from the primary rupture to the secondary fault can contribute to step-over jumps. However, 2D simulations

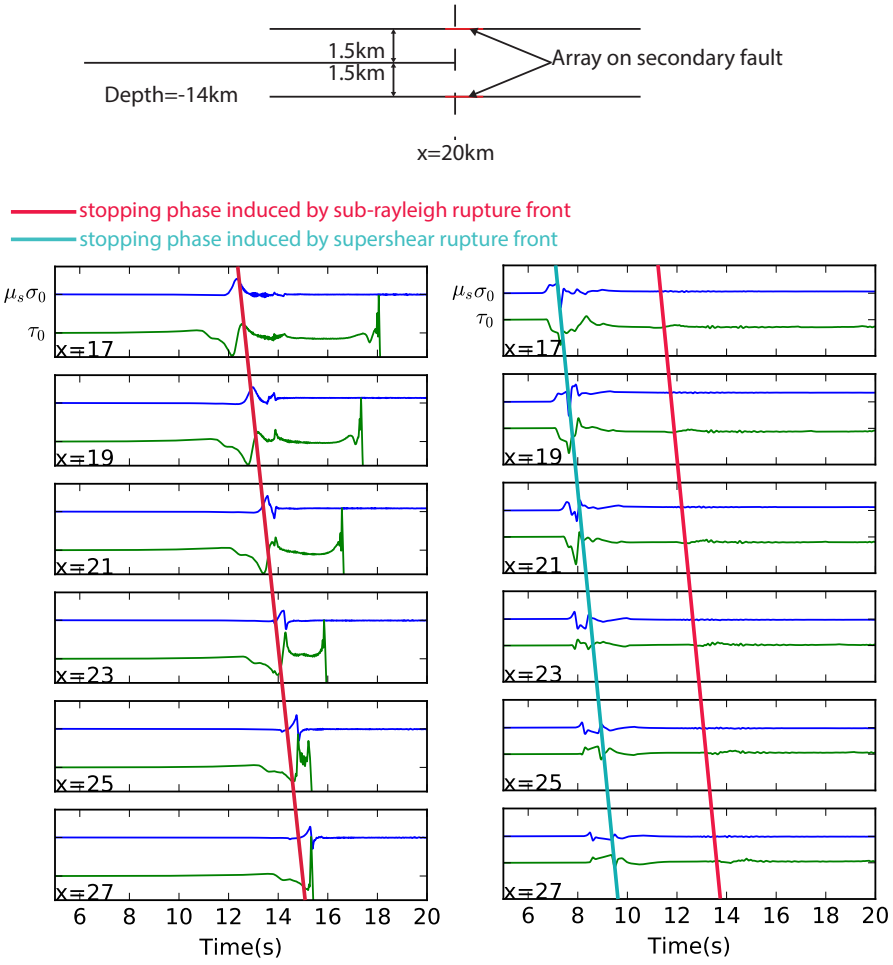


Figure 2.6: Comparison of dynamic stresses between a sub-Rayleigh rupture (left) and a super-shear rupture (right). (a) Map view of the two examples. Both have the same fault system geometry but different $S$ ratio ($S = 1.27$ for the sub-Rayleigh case and $S = 0.64$ for the super-shear case). An array of receivers (red) is placed along the second fault near the end point of the first fault, between $x = 17$ km and 27 km and at a depth of 14 km. (b) Transient shear stress $\tau(t)$ (solid green) and static strength $\mu_s\sigma(t)$ (blue) on the second fault of the sub-Rayleigh case (left) and super-shear case (right). Each panel corresponds to a different location along the second fault ($x$ position indicated by label). Stopping phases generated by sub-Rayleigh and super-shear fronts are indicated by red and yellow lines, respectively. The super-shear rupture did not breach the step-over because splitting of the rupture front weakens the peak amplitude of the stopping phase.

by Oglesby, 2008 indicate that dynamic stresses, especially high frequency stress peaks, are the dominant factor controlling the step-over jump behavior. He observed that the critical step-over distance depends on how sharp the initial stresses taper at the end of the primary fault, which determines the abruptness of rupture arrest and consequently the amplitude of stopping phases. In 3D, this effect of stopping phases can be more complicated because the shape of the rupture front can vary depending on $S$, $W$ and nucleation processes, generating multiple high frequency radiation phases when rupture fronts hit the boundary of the seismogenic region. The analysis of the effect of stopping phases in 3D is made more tractable here by forcing the rupture fronts to be straight, reaching the lateral end of the primary fault almost simultaneously at all depths (section 2.2). As will be discussed in section 2.5, the straight rupture front assumption will generate an upper bound estimation on $H_c$ due to the constructive interference of the stopping phases.

To demonstrate the predominance of dynamic stresses over static stresses, we show that dynamic stresses are much larger than static stresses in our long rupture models, in which the terminal rupture speed on the first fault is usually close to the Rayleigh wave speed. We select a pair of compressional and dilational step-over simulations with the following parameter settings: $S = 1.27$, $H = 1.5$ km and $W = 15$ km (Figure 2.7).

Static stress analysis would suggest that a dilational step-over is easier to breach because the second fault is unclamped (subjected to normal stress reduction) by rupture of the primary fault. However, when we consider the dynamic stresses, results are much more complex. In the compressional step-over, static normal stress increases in the second fault but a high frequency peak in dynamic stress brings it to failure. In the dilational step-over example, the static normal stress on the second fault decreases, lowering its strength and thus favoring the step-over jump, but the high frequency dynamic stress peak is not sufficient to bring the fault to failure. In both cases, static stresses alone are not sufficient to breach the step-over, because of their relatively small amplitude compared with dynamic stresses. A slightly larger compressional step-over jump than a dilational one is also observed in most of the examples presented by Hu et al., 2016 and in some of the cases in Lozos et al. (2014a) and Ryan and Oglesby (2014), especially in the sub-Rayleigh rupture cases. This implies that the step-over distance $H_c$ can be underestimated if only static stress are considered, especially for a compressional step-over. Moreover, dynamic Coulomb stresses carried by stopping phases have a different angular pattern than

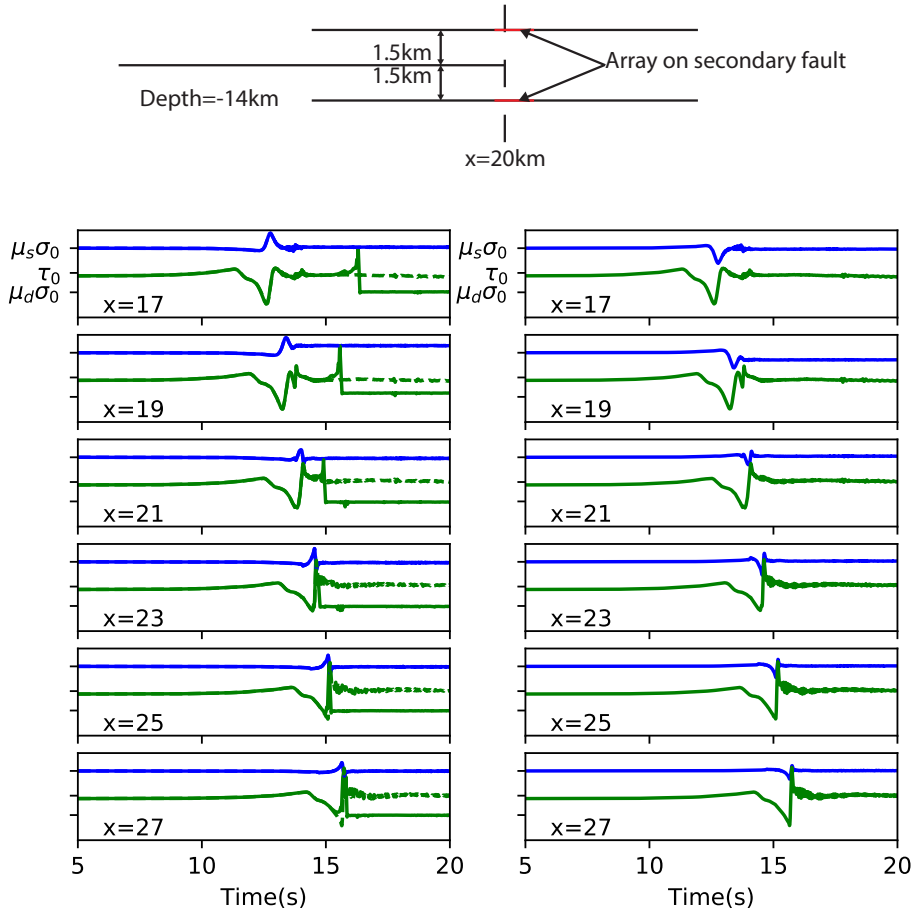


Figure 2.7: Comparison of dynamic stresses between compressional step-over (left) and dilational step-over (right). (a) Map view of the two examples. An array of receivers (red) is placed along the second fault near the end point of the first fault, between $x = 17$ km and 27 km and at a depth of 14 km. (b) Transient shear stress $\tau(t)$ (solid green) and static strength $\mu_s\sigma(t)$ (blue) on the second fault of the compressional step-over (left) and dilational step-over (right). Each panel corresponds to a different location along the second fault ($x$ position indicated by label). Dashed green curves are shear stresses computed in separate simulations assuming the secondary fault remains locked.

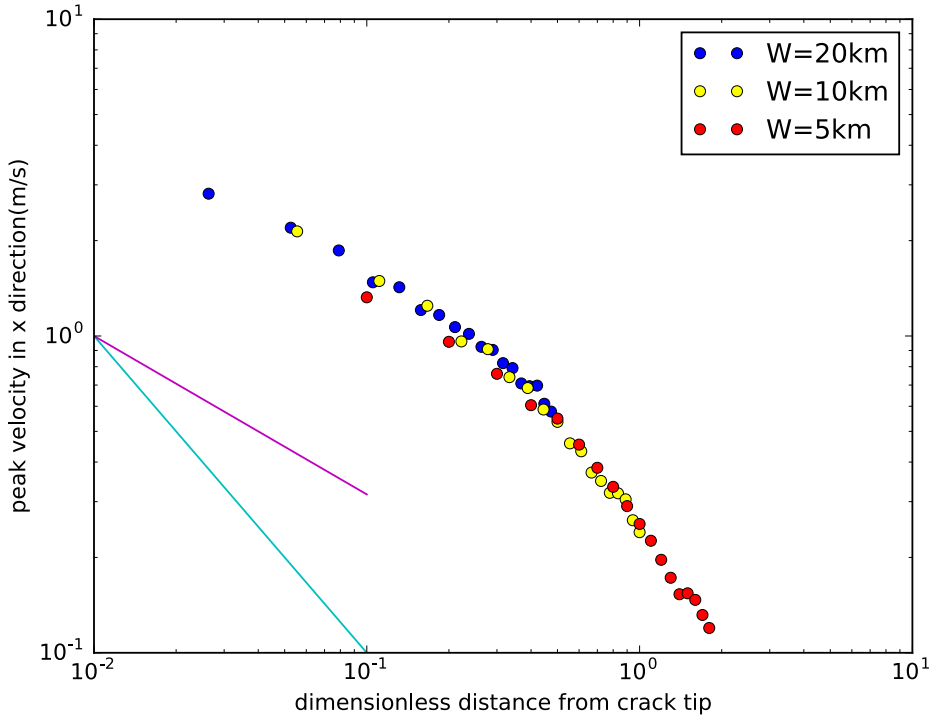


Figure 2.8: Peak ground velocity in the $x$ direction at 90 degree azimuth from the end of the first fault, as a function of distance to the end of the first fault normalized by seismogenic depth. Three cases with different seismogenic depth $W$ are considered (see legend).

static Coulomb stresses. This pattern is determined by rupture speed and will be discussed in section 4 and Appendix B.

### 2.4 Theoretical relation between $H_c/W$ and $S$

The theoretical relation between $H_c/W$ and $S$ cannot be derived analytically in 3D dynamic rupture problems. However, asymptotic 2D analysis provides a good approximation to the problem. When a straight rupture front hits the lateral edge of the seismogenic zone producing a line source of length $W$, the stopping phase it radiates can be approximated as a cylindrical wave in the near field ($0.01 < r/W < 0.1$), whose amplitude decays as $\frac{1}{\sqrt{r}}$, and as a spherical wave in the far field ($r/W > 1$), decaying as $\frac{1}{r}$ (Figure 2.8). Relations between the wave amplitude in these two distance ranges, fault geometry and dynamic rupture properties are derived in Appendix A.

The relations show that the maximum distance at which the Coulomb failure thresh-

old can be reached is proportional to $W/S^2$ in the near field and proportional to $W/S$ in the far field. This asymptotic analysis of maximum Coulomb failure distance under cylindrical and spherical wave approximations roughly explains what we have observed in the simulations: $H_c/W \propto 1/S^2$ when $H_c/W < 0.1$ (near field) and $H_c/W \propto 1/S$ when $H_c/W > 0.2$ (far field).

The previous analysis of peak dynamic stresses provides a necessary condition for step-over jump to happen. Lozos et al. (2014a) found qualitatively in 2D simulations an inverse relation between $H_c$ and the critical slip weakening distance $D_c$ which is proportional to critical nucleation size. Treating the step-over jump problem as a static stress triggering problem, they proposed that Coulomb failure has to be reached within an area larger than the critical nucleation size on the secondary fault to successfully initiate rupture. Here, we further investigate the problem by analysis of the nucleation criterion for 3D ruptures. The stopping phase of the primary rupture induces a stress pulse traveling at $S$ wave speed on the secondary fault. This pulse has a large aspect ratio, it extends vertically across the whole seismogenic depth but has a short width in the along-strike direction. Galis et al. (2017) found that if the nucleation zone has an aspect ratio greater than 10, spontaneous runaway rupture happens only if its shortest edge length exceeds a critical nucleation size. If $S \leq 3$, this critical nucleation size is independent of $S$ and is equal to the critical nucleation length by Uenishi and Rice (2003), which is close to $L_c$. If $S > 3$ the nucleation condition does not depend on the aspect ratio, it is equivalent to a critical nucleation area rather than a critical length. However, the very low initial stress when $S > 3$ correspond to cases where $H_c < 0.03W$ in our simulations. Such small step-overs are usually ignored in fault trace mapping and hazard analysis due to the higher likelihood of connection at depth (Graymer et al., 2007) promoting through-going rupture. Thus, for cases of interest, the critical nucleation size $L_c$ of Uenishi and Rice (2003) is an appropriate criterion. Therefore, increasing $L_c$ tends to decrease $H_c$ (Figure 2.4 color coded by $L_c/W$). This effect is weak when $L_c/W$ is small. Our previous analysis based on the maximum distance for Coulomb failure to occur hence provides an upper bound on $H_c$.

## 2.5 Discussion

### Comparison to empirical observations of $H_c$

From the analysis of simulation results, we find that the critical step-over distance $H_c$ depends primarily on seismogenic width $W$ and strength excess ratio $S$. In addition,

it is slightly modulated by the nucleation size $L_c$, which is explained by the effect of nucleation on the secondary fault by dynamic stresses carried by stopping phases.

Our modeling results are in first-order agreement with empirical estimates of critical step-over distance (Wesnousky, 2006; Wesnousky and Biasi, 2011; Biasi and Wesnousky, 2016). The ratio of shear stress to effective normal stress on the San Andreas fault and other major inter-plate faults has been inferred to be around 0.2 to 0.3 (Noda et al., 2009), which indicates an $S$ ratio to be greater than 1.5 considering a dynamic friction coeffcient of 0.1 and a static friction coefficient of 0.6.

When $S > 1.5$, our simulation results for both compressional and dilational step-overs are well represented by $H_c/W \approx 0.3/S^2$, and hence $H_c/W < 0.2$. For a typical $W = 15$ km for continental strike-slip faults we expect $H_c < 3$ km, which agrees with previous observations (Wesnousky, 2006) and numerical simulations (Harris and Day, 1999). The above arguments demonstrate that our new model is consistent with the previous "5 km recipe" when applied to typical continental inter-plate strike-slip faults.

However, our results indicate that empirical criteria for step-over jumps may not be readily applied to faults with different $W$ and $S$ under different tectonic settings, such as oceanic and intra-plate strike-slip earthquakes. Our theoretical results provide a more accurate estimate of $H_c$ for given $S$ and $W$. For a specific region, a range of $S$ values can be constrained by information on regional stresses and fault geometry. The stress state of a fault can be estimated by projecting the regional stress tensor onto the fault plane. The seismogenic depth $W$ can be estimated by the termination depth of background seismicity or by geodetic inversion of locking depth. The nucleation size $L_c$ is a more uncertain parameter, which may be inferred from seismological observations of large earthquakes (Mikumo, 2003; Fukuyama, 2003), but has only a second-order effect on $H_c$.

Additional support for the major effect of seismogenic depth on critical step-over distance is provided by the compilation of empirical observations by Biasi and Wesnousky (2016). Their figure 9 shows that longer ruptures with similar rupture depth extent are not necessarily stopped by wider step-overs. This is consistent with our theoretical arguments in which the amplitude and reach of stresses near the primary rupture tip depend on rupture width but not on rupture length.

**Effect of a thick seismogenic layer**

One important factor that challenges the "5 km criterion" is the dependence of $H_c$ on the thickness of the seismogenic layer, $W$. There are several reasons for variability of seismogenic thickness. The first controlling factor is the geothermal gradient, which controls the brittle to ductile transition of the crust and the deep seismic to aseismic transition of faults. Cooling of an old oceanic crust increases this transition depth and makes the seismogenic layer thicker, which is consistent with a large $H_c$ in the 2012 Indian Ocean earthquake (Meng et al., 2012). The Indian Ocean earthquake has an extraordinary penetration depth of 50 km (Yue et al., 2012) which is 2-3 times the depth of an average continental strike-slip earthquake. So we expect the maximum step-over width to be around 10-15 km considering the same $S$ ratio. Moreover, the Indian ocean earthquake is reported to have larger stress drop (Meng et al., 2012) indicating a smaller $S$ ratio, which makes the observed 20 km step-over jump (Meng et al., 2012) a possible scenario. Subduction of an oceanic crust greatly decreases temperature around it, which may deepen the brittle-ductile transition on crustal faults in the over-riding plate. This effect has been proposed to explain a rupture depth of 25 km in the 2016 $M_w$ 7.8 Kaikoura earthquake inferred from geodetic data (Hamling et al., 2017). For the same thermal reason, we expect intra-plate earthquakes to have a thicker seismogenic layer (Copley et al., 2014) and hence a larger $H_c$ than inter-plate earthquakes.

Dynamic processes that promote large rupture width can favor wider step-over jumps. Ruptures can penetrate deeper into the velocity strengthening region where ruptures cannot nucleate spontaneously. Our theory actually relates the critical step-over distance to rupture width, more fundamentally than to seismogenic width. Hence larger step-over distances are expected for large earthquake ruptures that penetrate below the seismogenic depth, for instance due to thermal weakening processes (Jiang and Lapusta, 2016).

Our results on strike-slip faults have implications also for other faulting types. To apply our model to dip-slip faults, we need to replace the Mode II stress intensity factor with the Mode III one, which involves a factor of order 1 that depends on Poisson's ratio. In dip-slip faults, the seismogenic width is larger, $W = h/sin(\alpha)$ where $h$ is the seismogenic depth and $\alpha$ the dip angle. We hence expect $H_c$ to be larger for faults with shallower dip angle $\alpha$. In addition, the step-over distance conventionally defined in map-view is larger than the fault distance defined here in the normal direction to the fault plane. Biasi and Wesnousky (2016) found a larger

critical step-over distance in dip-slip faults, which can be around 12 km.

Relations between fault system geometry and seismogenic depth may complicate the relation between $H_c$ and $W$. Zuza et al. (2017) found that the spacing between strike-slip faults is also proportional to $W$. This means that although $H_c$ is larger in areas with thicker seismogenic layer, the probability of a fault step-over jump is not necessarily larger, because of the sparsity of closely spaced secondary segments.

**Step-over jumps with lower initial stresses**

Our model indicates that ruptures have trouble breaching step-overs at low background shear stress (large $S$ ratio yields small $H_c/W$). On natural faults, we expect $S \gg 1$ to be typical because stress drop estimates are of a few MPa on average and strength drop can be several 10 MPa in the absence of excessive fault zone fluid overpressure. Faults operating at low background stress may have to breach step-overs by localizing slip into a more connected fault system (with narrower step-overs) (Cooke, 1997; Myers and Aydin, 2004).

In addition to a thicker seismogenic layer (Copley et al., 2014), intra-plate earthquakes have average stress drop significantly larger than inter-plate earthquakes (Allmann and Shearer, 2009; Scholz et al., 1986). Moreover, Kato (2009) suggests that, in contrast to inter-plate faults, the loading of intra-plate faults is dominated by regional plate stressing rather than by aseismic slip in deeper extensions of the fault, hence the loading of the seismogenic zone tends to be more spatially uniform than on inter-plate faults. These arguments imply that intra-plate faults can operate at overall smaller $S$ ratio than inter-plate faults, thus allowing for wider step-over jumps during earthquakes.

The possibility of step-over jumps can be affected by relations between seismogenic depth and the long-term average stress at which a fault operates. In earthquake cycle models of faults loaded by deep creep (Kato, 2012), it is found that as $W$ increases the average stress decreases. Fracture mechanics analysis of this problem leads to a relation that can be formulated as $S + 1 \approx \sqrt{W/L_c}$. Together with the relation $H_c/W \propto 1/S^2$ for large $S$ we obtain $H_c \propto L_c$. For small $S$ this model requires $W \approx L_c$ and, considering the relation $H_c/W \propto 1/S$, we obtain $H_c \propto L_c/S$. Hence, the aforementioned class of earthquake cycle models predicts a closer relation between critical step-over distance and nucleation size than suggested by our single-earthquake dynamic rupture models.

**A procedure to assess the potential for step-over jumps**

While our new model incorporates parameters such as $W$, $S$ and $L_c$, it is based on simplifying assumptions that may not be appropriate for all step-over problems. For example, we assume the fault strands to be parallel, which is not always the case. As described in Poliakov et al. (2002), the stress field near a propagating mode II rupture promotes secondary ruptures at an angle with the primary fault that depends on the background stress tensor and on rupture speed. Parsons et al. (2012) proposed to estimate the probability of multi-segment earthquakes by calculating the static Coulomb stress perturbation induced by one segment on all the surrounding segments. This method neglects dynamic stresses and can lead to substantial underestimation of jumping probability, as shown in section 2.3. We propose the following procedure to assess the potential for a step-over jump in a specific case scenario:

1. Run a dynamic rupture simulation on the primary fault.
2. Record the dynamic stress on all secondary faults.
3. Determine if failure is reached over a contiguous zone larger than nucleation size, for given set of initial stresses.

Comparing with the alternative approach of running a dynamic model of the whole specific step-over system, our proposed method is more computationally efficient. A conservative estimate is obtained by assuming a very small nucleation size. In step 3, the initial stresses on the secondary faults can be varied over a range constrained by independent considerations, without the need to repeat step 1.

**Potential limitations**

Here we summarize the main limitations of our model and suggest potential improvements or clarify their effects on the estimations of $H_c$.

We assumed that the initial fault stress results from a homogeneous regional stress field. In reality, fault stresses can be heterogeneous at a step-over due to stress concentrations caused by past earthquakes near fault tips. Others have considered different uniform stresses on the two fault segments (Harris and Day, 1999). Revisiting our derivation assuming the stress states on the two faults are different, we find that our $H_c$ prediction equation remains the same after simply replacing $S$ with the ratio $S'$ between the strength excess of the second fault and the stress drop of

the first fault. Due to residual stresses left by previous ruptures, $S'$ can be significantly smaller near the step-over than our previous estimate of $S > 1$. This allows for larger $H_c$ and reconciles our simulation results with typical observed step-over jumps in the km range even when $S$ is high far from the step-over. The role of stress heterogeneity on step-over jumps can also be addressed through earthquake cycle modeling (Duan and Oglesby, 2006; Shaw and Dieterich, 2007; Yıkılmaz et al., 2014). The fundamental results assuming homogeneous initial stress presented here can help understand the outcomes of such more complete models. For example, we expect initial shear stress to be mostly concentrated near the deep edge of the seismogenic zone due to creep on the deeper portion of the fault (see, e.g., figure 1 of (Kato, 2012)). If this stress concentration is substantial, we should observe a tendency for ruptures on secondary faults to initiate in the deepest part of the seismogenic zone. However, the coarse resolution and small number of finite fault inversion results of earthquakes with step-over jumps (Wald and Heaton, 1994; Yue et al., 2012; Field et al., 2014; Hamling et al., 2017) do not allow to determine if such a tendency occurs in nature.

We assumed a rectangular rupture area and a vertical rupture front. In reality, rupture area and rupture front can have complicated geometries due to fault geometry as well as stress and frictional heterogeneities, which can generate multiple strong phases. In our model, the rupture front forms a perfect line source and is a worst-case scenario because it generates the strongest constructive interference. Our simulation results thus serve as an upper limit estimation of the amplitude of stopping phase radiation.

We assume rupture termination to be very sharp, as if the rupture encountered a steep increase of fracture energy or a sharp decrease in shear stress. In reality rupture arrest can be gradual, for instance if rupture is stopped by an area of smoothly decreasing initial stress (Oglesby, 2008), which leads to weaker stress concentration and stopping phases and hence less efficient step-over jumps. In these regards, our model provides an upper bound on $H_c$, which is useful for a conservative hazard analysis.

Step-over jumps can be facilitated by structural features such as intermediate fault segments (Lozos et al., 2014b) or linking faults (Oglesby, 2005). An important case is a flower structure, in which two fault segments that are separate at the surface merge into a single fault at some depth.

In this case, dynamic rupture simulations by Aochi (2003) showed that ruptures break through the step-over by taking advantage of the deep linkage, regardless of

how wide the gap is at the surface, unless the deep rupture pathway is too narrow due to a linkage depth too close to the bottom of the seismogenic zone. The step-over distance at the surface is proportional to the linkage depth if the average dip angle of the fault branches is controlled by the internal frictional angle of the crust (Naylor et al., 1986; Di Bucci et al., 2006). Thus flower structures could also lead to critical step-over distances $H_c$ proportional to $W$. Distinguishing between the deeply linked faults interpretation and the parallel faults interpretation of the relation $H_c \propto W$ needs further investigation of the geometry of active faults at depth. Sometimes the evidence is not sufficient to determine if a step-over had a linking fault with significant slip over a significant depth range that clearly contributed to the (apparent) step-over jump. In some cases a linking fault with little slip, or too shallow slip, may just be a by-product of the larger scale rupture across the step-over without contributing much to it. The theory we developed provides physical bounds on what is possible without linking faults, and this may assist in the interpretation and discussion of specific cases. For example, applying our theory to a particular (hypothetical) example in which surface rupture on a linking fault is documented, one may be able to argue that, given the background stress, stress drop, seismogenic depth and step-over distance, in principle the rupture could have jumped the step-over even without a linking fault. In such an example, the theoretical argument can motivate further study of the amount and depth extent of slip on the linking fault in order to assess to what extent it contributed to the rupture across the step-over.

We assume that both fault segments are embedded in a homogeneous elastic half-space. However, most fault zones will include a low velocity layer surrounding the fault plane (Lewis and Ben-Zion, 2010; Huang and Ampuero, 2011; Finzi and Langer, 2012a; Finzi and Langer, 2012b). The elastic modulus of this layer adjacent to the primary fault can be smaller than host rock and also different from the elastic modulus of the layer adjacent to the secondary fault. The gradation in the elastic properties in the overlapping region may contribute to the complexity of the radiated field through multiple reflections and transmissions (Ben-Zion et al., 2003; Huang et al., 2014). For certain frequencies, this may lead to amplification of the dynamic displacement and may affect the rupture trigger-ability on the secondary fault.

We assumed a linear slip weakening friction law, i.e. fault strength decreases linearly with accumulated slip. A non-linear slip-weakening law with steeper weakening at small slip facilitates nucleation (Dunham, 2007) and hence can increase $H_c$. As is found by Ryan and Oglesby (2014) in their 2D step-over simulations, the functional

form of a frictional law has only a second order effect on a step-over problem given constant fracture energy. We thus expect our scaling relation derived from slip weakening friction law to hold for rate-and-state friction law.

Ruptures propagating on rough faults decelerate and accelerate non-uniformly leading to enhanced seismic radiation (Shi and Day, 2013). Also, a rupture on a non-planar fault may stop abruptly before reaching the end of the fault due to strong variations in the fault strike or stress heterogeneity. This would also be a source of stopping phases and strong radiation (Madariaga et al., 2006). The former may promote jumping large step-overs by enhancing the high frequency component of the wave field. The latter may be important to investigate in future studies for its implication on earthquake triggering or delayed jumping across fault segments.
Ample evidence from laboratory and numerical studies points to the relevance of enhanced dynamic weakening during fast rupture propagation while rupture nucleation is controlled by rate-and-state frictional behavior (Rice, 2006; Noda and Lapusta, 2013). As a consequence, nucleation sizes on natural faults can be orders of magnitude smaller than what is assumed in the present study. However, as the critical nucleation size decreases towards 0, we expect $H_c$ to increase and converge to an upper bound value controlled by stress amplitude rather than nucleation size. This upper bound is given by the theory developed in section 4 and is close to the value obtained in our simulation results.

To simplify the discussion, we focus our attention on cases with $S < 3$, for which the critical nucleation size has a weak dependence on $S$. For $S > 3$, the critical nucleation size increases rapidly with $S$, and the critical step-over distance could be even smaller than predicted by extrapolating the results presented in Figure 2.4.

## 2.6 Conclusions

The present computational and theoretical study of earthquake rupture on faults with step-overs provides fundamental insights on the physical factors controlling the limits on the step-over distance that a rupture can jump. By conducting a systematic set of 3D dynamic rupture simulations on strike-slip faults with uniform pre-stress and friction properties, we have established theoretical dependencies of the critical step-over jump distance $H_c$ on seismogenic depth $W$, pre-stress level $S$ (the ratio of strength excess to stress drop) and critical nucleation size $L_c$ (the ratio of shear modulus to slip-weakening rate). An understanding of the mechanical origins of these dependencies is obtained by analytical arguments based on fracture

mechanics. A critical step-over jump distance model of the form

$$H_c \propto W/S^n$$

is established where $n = 2$ in the near-field regime when $H_c < 0.2W$ (or $S > 1.5$) and $n = 1$ in the far-field regime when $H_c > 0.2W$ (or $S < 1.5$). Nucleation size has a second order effect on critical step-over distance; increasing $L_c$ decreases $H_c$ mildly.

We estimate the critical step-over distance to be a fraction of the seismogenic depth. This theoretical estimate is of the same order of magnitude as the maximum step-over distances derived empirically for continental strike-slip faults. Our model in particular predicts that earthquakes with exceptionally large rupture depth extension can breach proportionally wide step-overs. This prediction is consistent with observations of earthquakes in regions of thick oceanic lithosphere for which ruptures breaching step-overs wider than 10 km have been reported, such as the 2012 $M_w$ 8.6 Indian Ocean earthquake (Meng et al., 2012) and the 2016 $M_w$ 7.8 Kaikoura earthquake (Hamling et al., 2017). Our results also suggest that the maximum step-over distance widely used in hazard analysis may not be conservative enough for faults that operate at relatively high average stress and have thicker seismogenic zone, for instance intra-plate faults.

*Chapter 3*

# IMAGING SUBDUCTED SLAB USING DEPTH PHASES

# ABSTRACT

A recent study of a shallow Kuril subduction zone event displays significant waveform multi-pathing for paths propagating down the slab towards Europe (Zhan et al., 2014a). Here, we present results from the reverse direction, that is the effects on depth phases of deep events propagating up the slab. Differential travel time sP-P analysis shows a systematic decrease of up to 5 seconds from Europe to Australia and then to Pacific which is indicative of a dipping high velocity layer above the source region. Finite difference simulations indicate that a slab shaped structure that follows the Benioff zone at shallow depth and steepens beyond 400 km produces a model that can account for the sP-P differential travel times of our 5s for oceanic paths.

## 3.1 Introduction

One of the most fundamental achievements produced by the Vela program, i.e. a twenty-five year program, is that setting off large explosions at known locations and origin times demonstrated that the Earth is not PREM (Kerr, 1985). In particular, the Longshot experiment located on Amchitka Island reveals over 5 seconds anomalies in P-wave travel times along slab paths as discussed by Davies and Julian (1972). Early tomographic imaging suggest that such subduction is not simple in that some slabs flatten-out and some drop into the lower mantle, (Creager and Jordan, 1984), and more recently Obayashi et al. (2013) and Simmons et al. (2012). While these images and interpretations are generally consistent, they do not produce significant waveform distortions because the anomalies are too small to explain the waveform complexity (Figure 3.1) see Zhan et al. (2014a). Because of the difficulty in knowing the locations and origin times of off-shore events situated along the Pacific Basin, one can examine the waveform shapes directly between an outer-shore event vs. an event in the down-going slab. Obviously, those signatures are distinctly different even though the events are less than 300 km apart (Zhan et al., 2014a). By comparing such an event pair, one can ascribe all the differences in the observed waveform to the source side structure differences.

Here, the waveforms are aligned on the PREM model predictions. A particularly useful method to produce a mechanism is the Cut-And-Paste (CAP) method which was developed by Zhu and Helmberger (1996) for regional phases and Chu et al. (2009) for teleseismic phases. The method breaks-up the synthetic seismograms into segments containing the P and S waveforms and searches for the best shifts required to both fit the time shifts ($\Delta t$) between synthetics and observed waveforms and earthquake source mechanisms (strike, dip and rake). Note that these shifts are relative to the epicenter location and origin time, both are poorly known. Investigators interested in studying distributed sources just apply these shifts manually and search for the fits of the depth phases, i.e. Langston and Helmberger (2007) and (Helmberger, 1983) at all distances. Figure 3.1 shows that two near events, one occurring in the slab, the other an outer-rise event, which display obvious waveform distortions compatible with a slab structure and origin time. Figure 3.1D displays the geometry and 2D simulation for the outer-rise event where the teleseismic phases are less affected by the slab structure. At small distances, i.e. 30°, the paths sample the bottom of the slab, which needs some adjustments as well as the most distant data near 90°. These distances are critical to both core-mantle boundary structure and shallow structure where the phase sP develops, see Figure s1, which displays

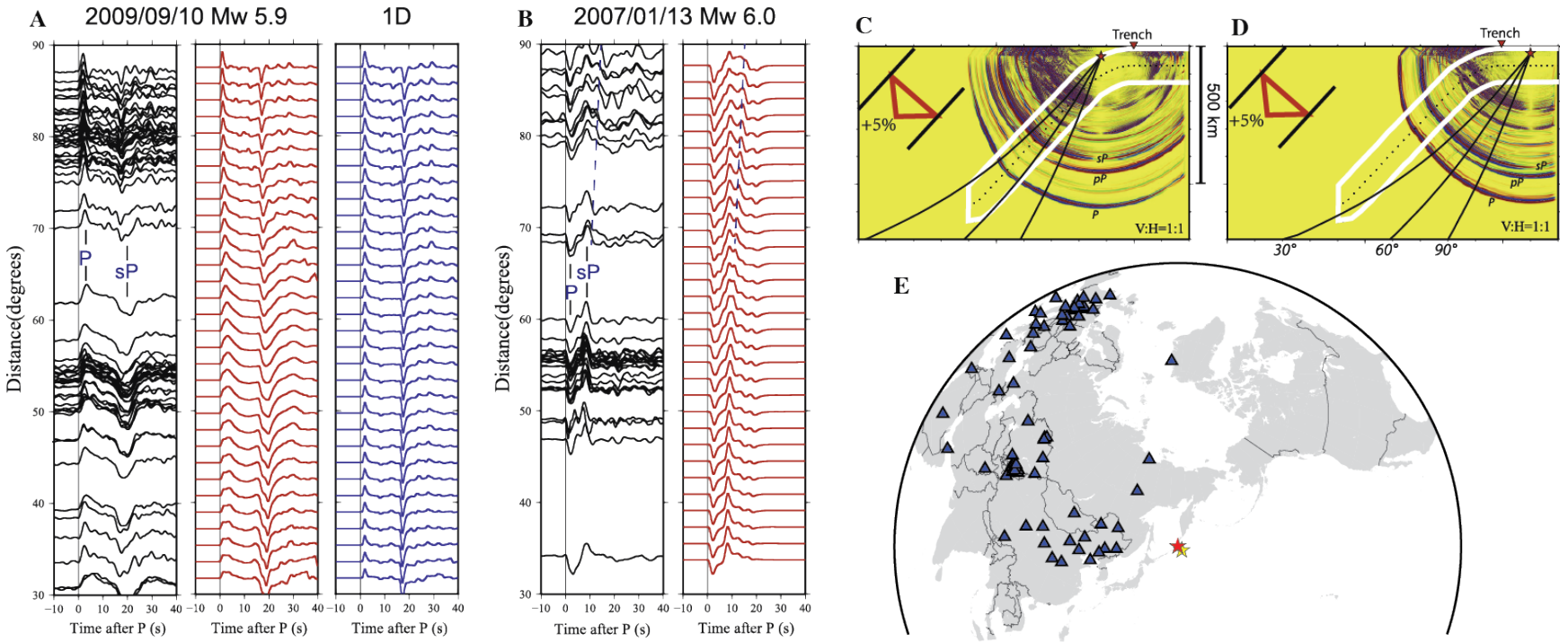


Figure 3.1: Modified from Zhan et al. (2014a). Waveform observations and simulations for the 2009/09/10 $Mw$ 5.9 inter-plate earthquake and the 2007/01/13 $Mw$ 6.0 outer-rise earthquake. (A)Record-sections of observed (left panel, black) and synthetic (right panel, red) seismograms for the 2009 inter-plate earthquake, aligned by the first P arrivals. (B) Similar to (A) but for the 2007 outer-rise earthquake. (C) 2D finite-difference simulation of the 2009 inter-plate earthquake (red star) with a high-velocity slab (outlined by the white line). The inset shows the triangular velocity profile across the slab, with 5% perturbation in the slab center. Black lines display the P wave ray paths to tele-seismic distances of 30°, 60° and 90°, respectively. (D) Similar to (C) but for the 2007 outer-rise earthquake.(E) The red and yellow stars are the interplate and outer-rise earthquakes respectively.

how slab structure affects all distances as discussed in 3D by Lu and Grand (2016). Since such slabs exist, they should affect the depth phases from deep events in the direction of the Pacific, as displayed in Figure 3.2. Ray paths (pP and sP) sampling the slab should be early and distorted, i.e. multi-layered, as displayed in Figure 3.2. Here, we have assumed a mechanism derived for a deep event in this region used in two previous efforts and included in Figure 3.2, Zhan et al. (2014a) and Wei et al. (2013). Note that a thrust mechanism generates a strong PP phase, which can interfere with pP at distances less than 50° and sP near 80°, Figure 3.2B. The phase pPcP can also prove troublesome. Therefore, one must be careful to isolate particular arrivals and work with differential measurements such as displayed in Figure 3.2. Moreover, there are issues involving the well-known deeper fast velocities (slab debris) and the mid-Pacific super-plume, the so-called Large Low Shear Velocity Provinces (LLVSP) structure. Differential studies can, hopefully, provide some constrains on the upper slab structure not normally included in tomographic studies.

## 3.2 Waveform Data and Processing

The May 24 2013 $M_w$ 6.7 sea of Okhotsk earthquake occurs at a centroid depth of 642 km which provided an opportunity to study depth phases that travel upward along the slab. The event has a relatively simple source process and large enough to provide a large enough signal to noise ratio to study. The data used, here, was downloaded from the Incorporated Research Institutions for Seismology (IRIS) by applying standard procedures and plotted as a record section, Figure 3.3. The signals are low pass filtered to below 0.2 Hz to eliminate the supershear rupture directivity effect (Zhan et al., 2014b). We plot these seismograms by aligning them according to their P wave arrival time such that we can easily compare arrival time of other phases with respect to P. The azimuths to the various stations is color coded, where we predict the depth phases should be early (green and blue) towards pacific and normal (red) towards Europe. The sample at red stations are located mostly in non-tectonic Eurasia continental regions while most of the blue traces were recorded by Pacific Island Stations. Note that the noise level is distinctly higher at these stations along with receiver-site waveform complexity in general. Since the pP phase is nodal, the phase sP appears to be the most useful where, for example, TARA and MANU arrive earlier with respect to P arrival than at KEV. Most of the paths sampling between 60°and 70°agree with this assessment, which can be verified by running the CAP code on these records, presented in Figure 3.4A.

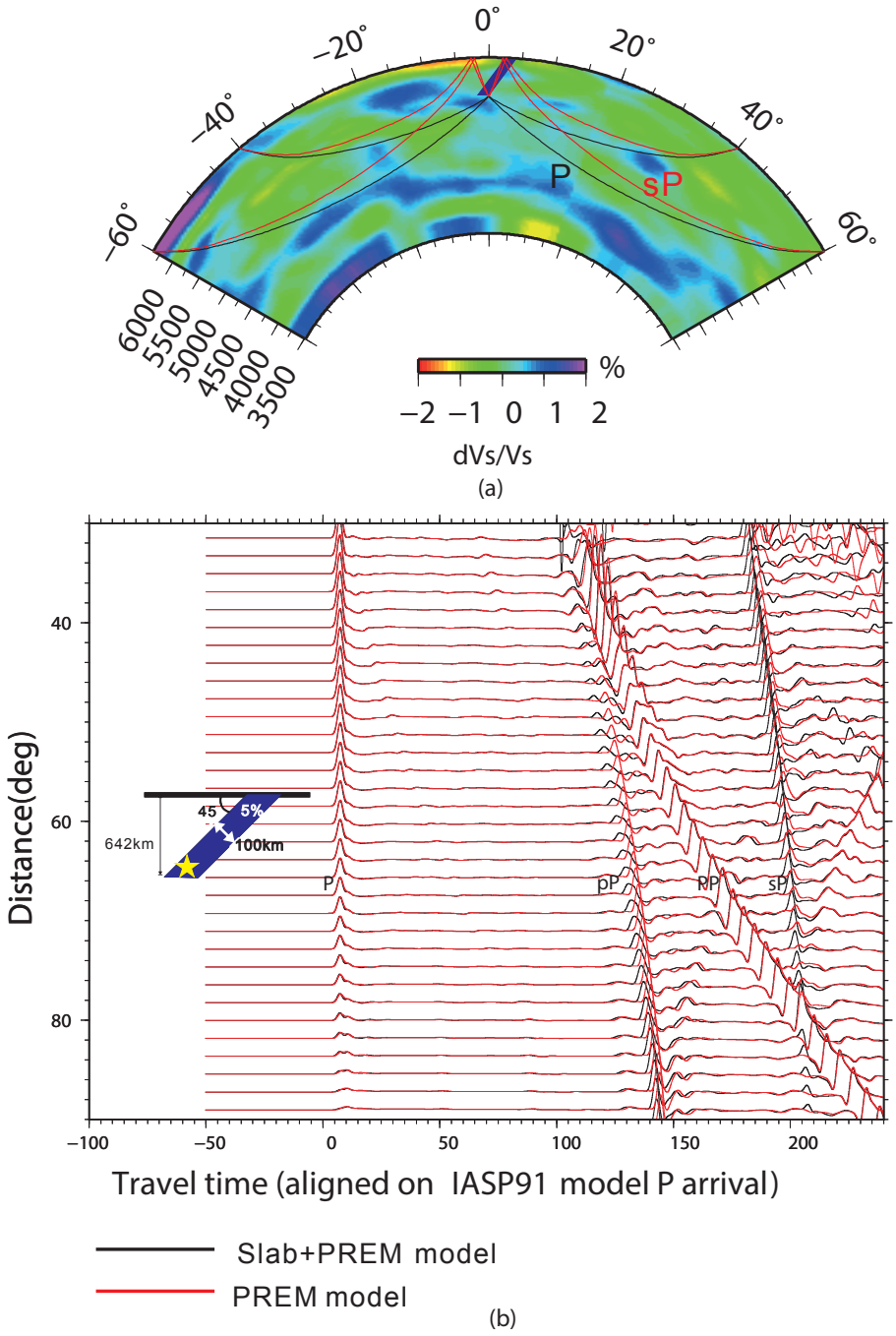


Figure 3.2: (a) PREM model with a 45° dipping slab model inserted in it. Black and red curves are the ray path for the P and sP phases to both Eurasia (negative distances) and Pacific (positive distances). (b) Simulated synthetic seismograms to the Pacific direction with the slab model (black) compared with that without the slab model(red).

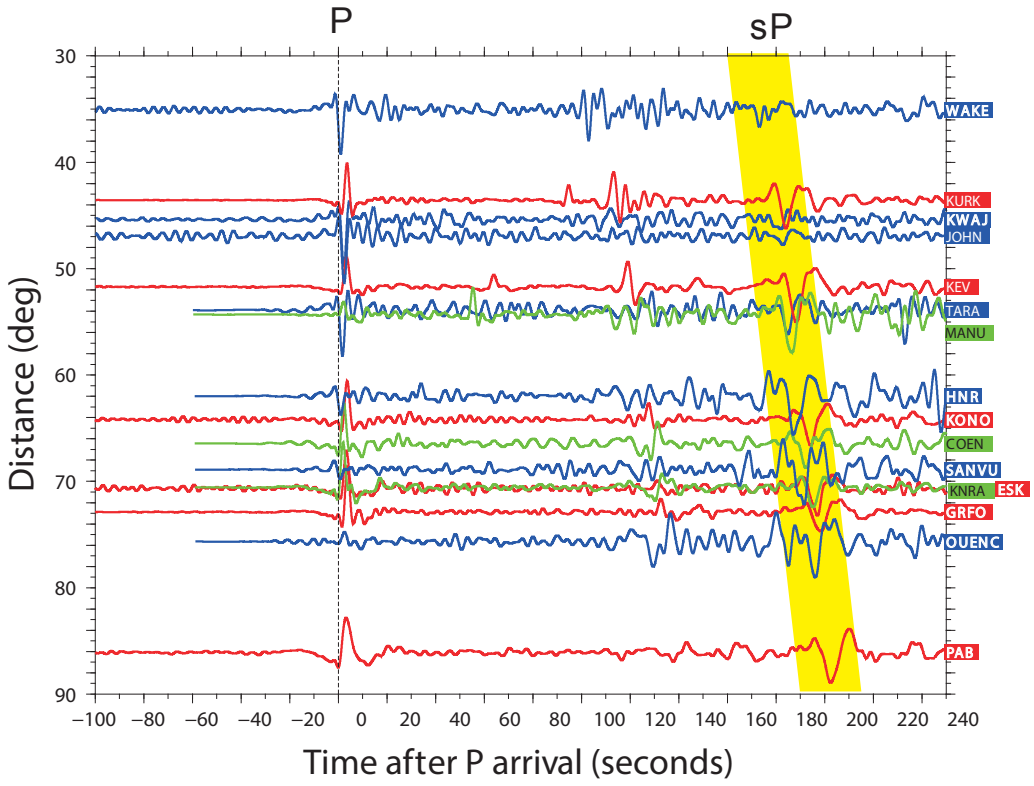


Figure 3.3: Recorded seismograms for the Sea of Okhotsk deep event. The seismograms are filtered to 5s-20s to avoid source directivity effect. Letters in the right text box indicate the global station code. The seismograms are color coded as red for stations in Eurasia continent and blue for stations in the Pacific and green for stations in Australia.

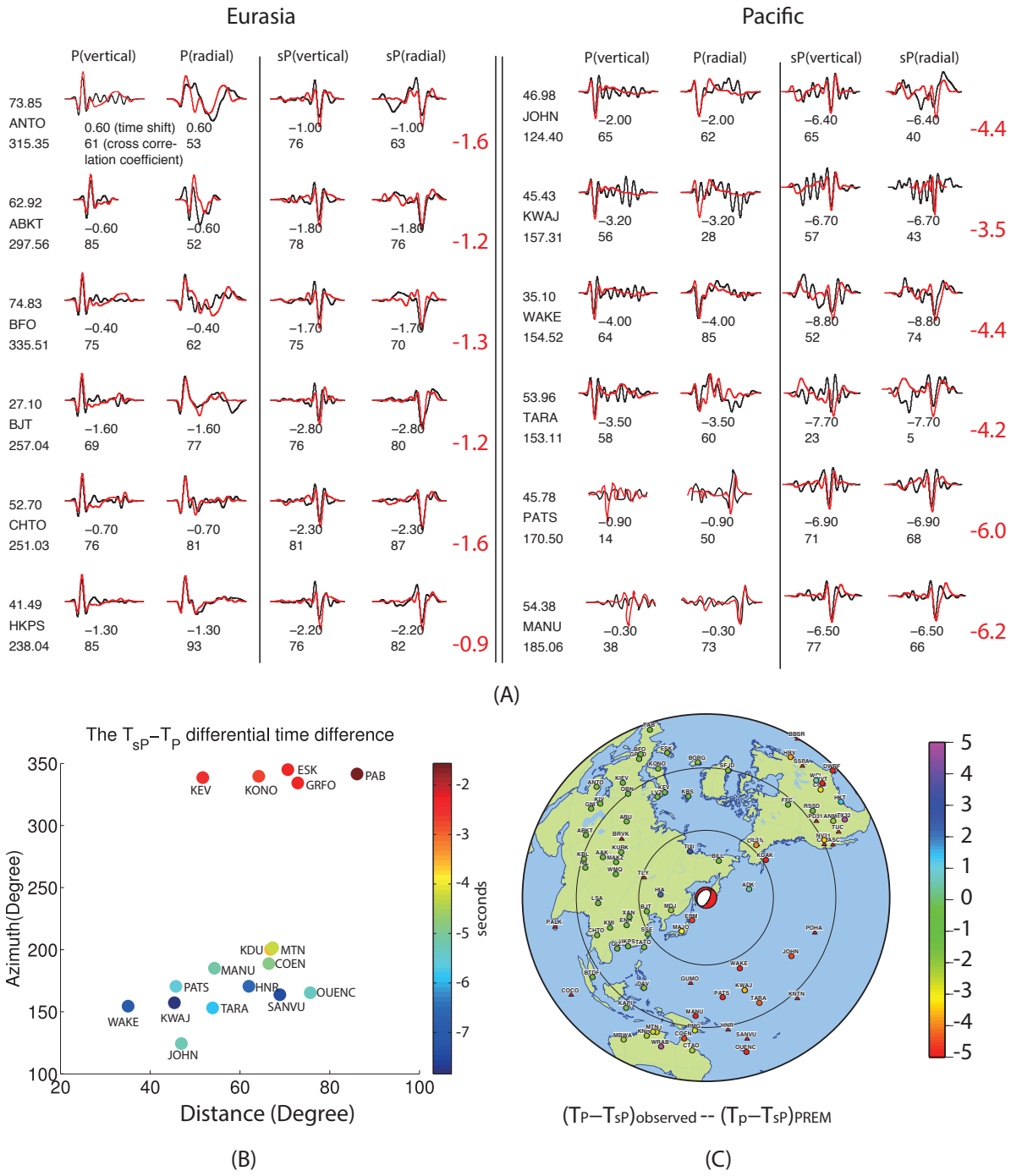


Figure 3.4: A. CAP results of the travel time shifts between observations(black) and synthetics(red) for P and sP phases. The lower red numbers are the calculated double differential travel time $(T_{sP} - T_P)_{observed}$-$(T_{sP} - T_P)_{PREM}$. B.The double differential travel times as a function of distances and azimuths. C. The global map of the differential travel time.

As introduced earlier, the CAP code allows synthetics to shift over a window to obtain the best fits. For example, at station ANTO, the best cross-correlation (CC) as observed on the vertical component was 0.61 and 0.60 on the radial component, with a timing shift relative to PREM of 0.6 second. The sP results are given on right, i.e. $-1.0$ second and with their differential equals $-0.4$ second. The results from the Pacific Island Stations display lower CC's but consistent travel time anomalies as displayed in Figure 3.4B. This relative shift is about 4 to 5 seconds and is independent of origin time and depth estimate issues. The differential timing results are included globally on the station map, Figure 3.4C. However, the waveform shape distortions prove difficult to establish given the noisy signals without removing site effects. In the next section, we will address some progress in matching the data in the two profiles.

## 3.3 Modeling efforts

Earlier we introduced a synthetic record section of using PREM model against adding a slab structure assuming the mechanism of the 2013 event, which dips to the east, Figure 3.2. This produced a strong PP phase and the strength of reflected core phases, i.e. pPcP, relative to weak PcP. In contrast, the radiation pattern produces strong PcP which is apparent at this azimuth, Figure 3.6. Thus, this record section is simpler and since continental site responses are relatively simple as well, such data has been widely used in developing reference models and tomographic models. A prediction from the LLNL model introduced earlier (Figure 3.2) along this 2D section agrees well with the data. We have neglected the broadening of the phase sP due to attenuation. However the timing is matched well for all the phases. In contrast, the profiles to the west are more difficult to model because of the strength of the up-going phases interfacing with the slab and, secondly, the complexity of oceanic site responses. We begin by conducting a series of sensitivity tests.

### Effects of slab width

Here, we returned to the PREM model but allow the slab to have different thicknesses, namely thin (60 km) and thick (120 km). The results plotted relative to pP are given in Figure 3.6. We have included the synthetics for the 1D model as a reference. The nearest ranges show some complexity as the PP phase separates from pP along with the interaction with the 660 km discontinuity. At larger ranges PP is well behaved and crosses the phase sP near 85°. As expected, the phase sP is the most affected by the slab thickness, which is much more obvious with the thicker slab. It also tends to

lower the amplitude because of the multipathing especially at the larger ranges. Note the strength of the core phases, pPcP and sPcP which interact with above phases at crossing distances making a simple analyses difficult. There is, also, the issues of changing slab-dip and upper-mantle phase-transitions producing additional local wavetype secondary reflections as recently introduced by Wang et al. (2014).

**Slab-shape**

The geometry of the slab has a strong effect on the up-going paths in terms of how long the ray path remains in the slab, i.e. Figure 3.5. Note that the core-phases pPcP and sPcP miss the slab since they have relatively steep paths but sample the mantle wedge structure. These are difficult to study because of the lack of data from the Great Pacific Basin. After running a number of test models, we find the best fitting model that steepens within the transition zone as displayed in Figure 3.7. Such a structure is suggested from the seismicity mapping given in slab 1.0 (Hayes et al., 2012). Here, we just inserted the relatively fast slab into the LLNL model as in the PREM reference (1D) model presented in Figure 3.2.

## 3.4 Results

Attempting to match a broadband record section across the southern Pacific proved difficult as expected. It is much easier at periods longer than 20 s where one does not detect the slabs and the Earth looks PREM-like. But, we have some success and learned something about the significant effects of the complexity of radiation pattern in what one observes. The P-wave fits are satisfactory at the smaller distances except for some extended coda such as observed at WAKE. Such features can be observed for other events and is probably a site response issue (Wei et al., 2013). The signals between P and pP appear to be random and are probably oceanic island structures generated noise. Since there is this level of signals occurring before the P-wave although there could be embedded peg-legs caused by upper-mantle reflectors (Revenaugh and Jordan, 1991; Li et al., 2014). The pP phase seems to be fit in timing but the synthetic is too simple which could be caused by the strong directivity downward that splits the pP as discussed by Zhan et al. (2014a) or the surface reflection above the mantle wedge? The pP phase is correct in timing but are complex, observationally as is sP. In short, there is probably a fast dipping slab, but is difficult to accurately model without some stacking which is not possible in the Pacific Basin.

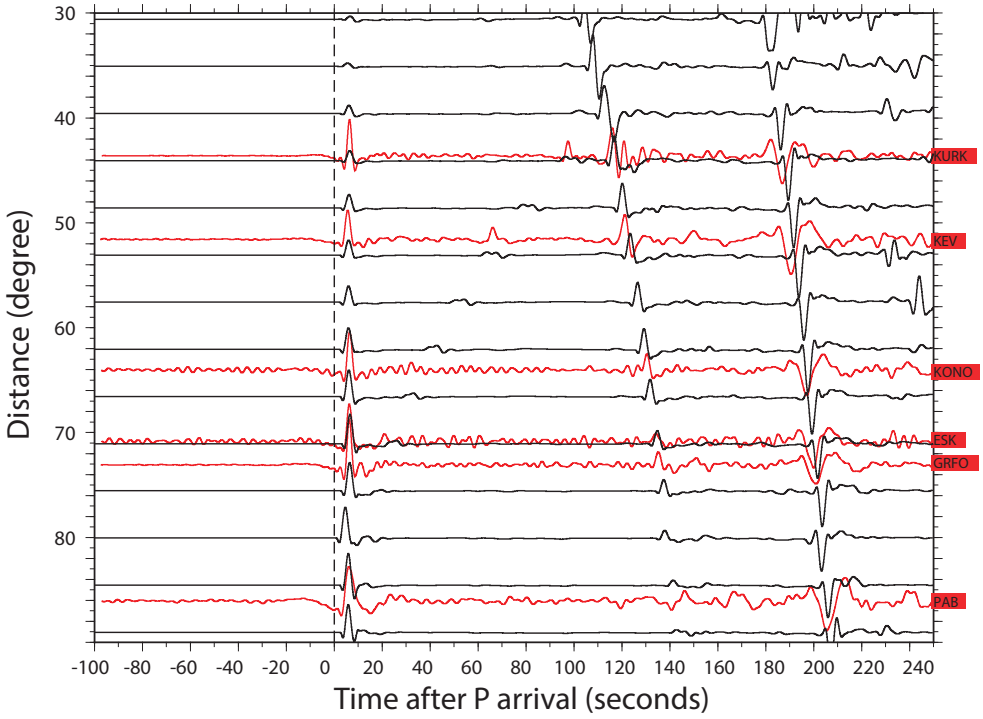


Figure 3.5: Comparison of synthetic predictions from the tomographic model GyP-SuM (Vs) and LLNL (Vp) given in black along with some samples of waveform data displayed in red as displayed in Figure 3.3.

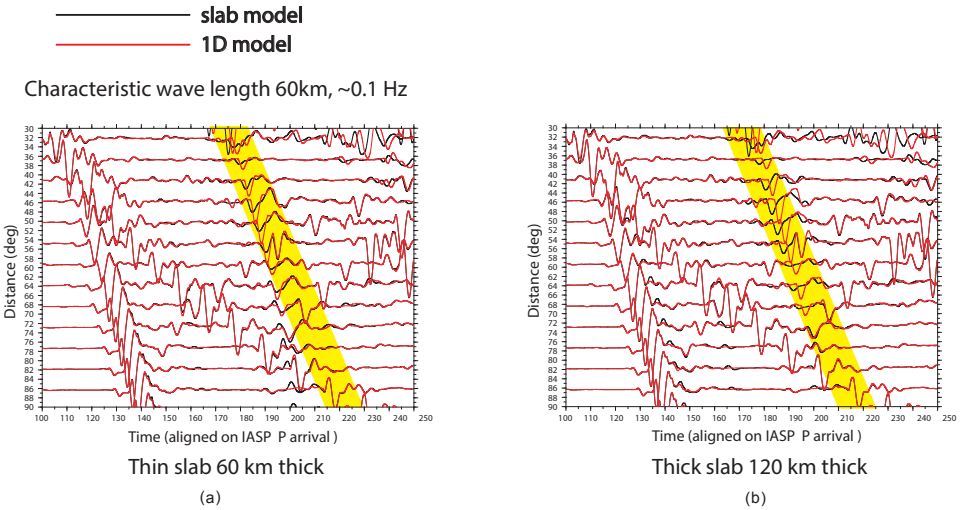


Figure 3.6: We test slabs of different thickness. When the thickness of the slab is comparable with the seismic wave length, the finite frequency effect can be significant due to which travel time shift is very small. But when the slab thickness is doubled in (b) the time shift become evident. Considering our major period of 0.1s in observation, the slab thickness should not be smaller than 60km.

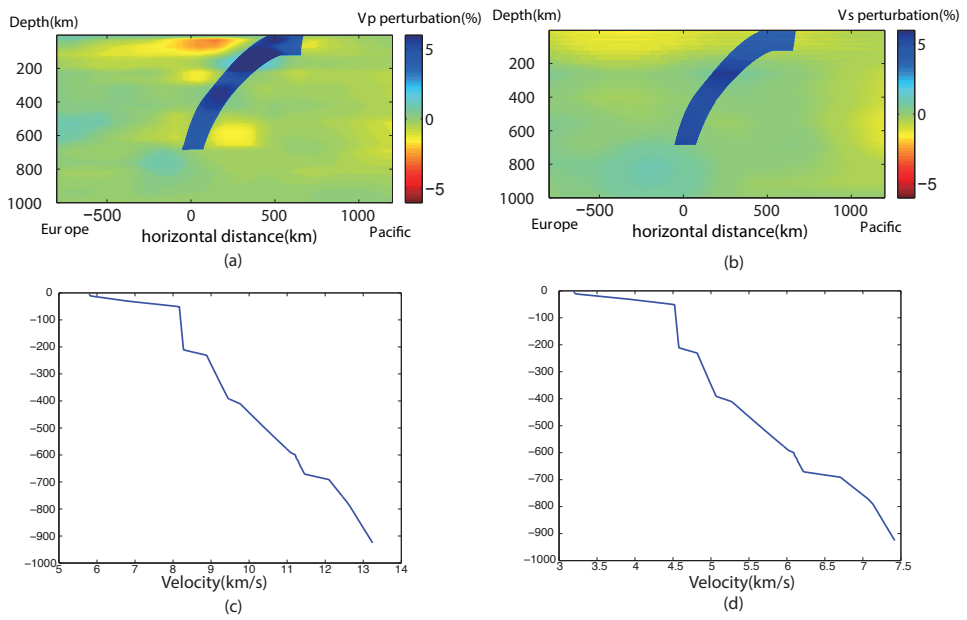


Figure 3.7: A slab model that steepens within transition zone. We here show the preferred model of the slab structure. Because an all 45 degree dipping slab is not able to generate enough time shift due to the steep take off angle of sP phase that are observed in the pacific. We suggest that a slab model that steepens at depth can better explain the observed travel time shift in Pacific region. (a) and (b) are the local zoom in of the preferred $V_p$ and $V_s$ model with slab structure. (c) and (d) are the corresponding 1D model based on which (a) and (b) are built.

**Station residuals as function of depth**

Although we have been focusing on depth phase distortions, the same paths can be investigated by direct phases. In this case, there are not many stations directly above this region. The best instrumented slab is provided by Hi-Net on the Japanese islands. Attempts at inserting slabs into tomographic images have been performed by Zhao et al. (1994). A detailed study of these network recordings of deep events revealed that their slab model needed to be sharpened and enhanced in velocity along with the addition of stronger low velocity mantle wedge zones (Chen et al., 2007). This means that shallow events should display strong azimuth path travel time residues since some paths sense the slabs while others travel through the slow zone. This appears to be the case as displayed in Figure 3.9. These residuals were determined by the CAP code as discussed earlier assuming the PREM 1D models. Generally, both the travel time delays and station amplitudes (AAF's) are well correlated for neighboring events or clusters (Chu et al., 2013). Obviously, in this case the shallow event has amazing residual, along the path to western US, which

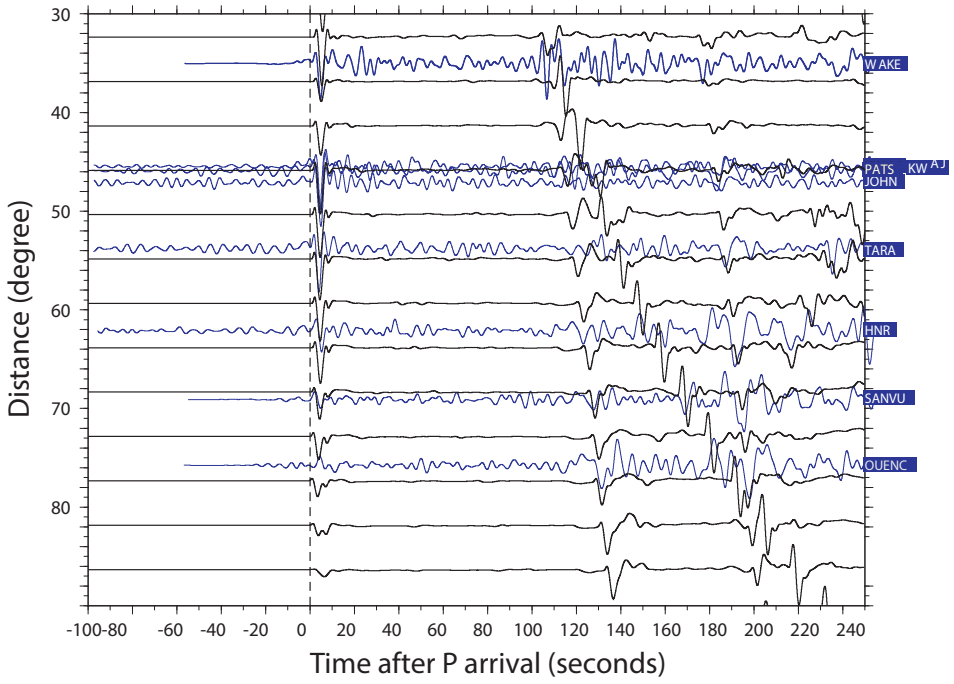


Figure 3.8: Slab model with 5% velocity perturbation that steepens at depth is combined with tomography model. Our model is able to simulate the differential travel time caused by slab structure but the waveform shapes are not well matched of this period.

is not observed for the deep event. Thus, systematically studying these events with depth appears as a promising approach in their relationship to waveform distortions.

## 3.5 Conclusion and discussion

Given the complexity associated with oceanic paths it proves difficult to rely on waveform distortions alone to define slab shapes. Working with larger events may prove useful to avoid noise problems as addressed in this section as well as attempts at refining locations and origin times.

### Modeling large events

The issue of complexity caused by oceanic paths and noise can be avoided by working with larger events because large events' records have higher signal to noise ratio. However, recent studies indicate that such events generally have complex rupture patterns and extended source durations, i.e. (Wei et al., 2013). This particular event,

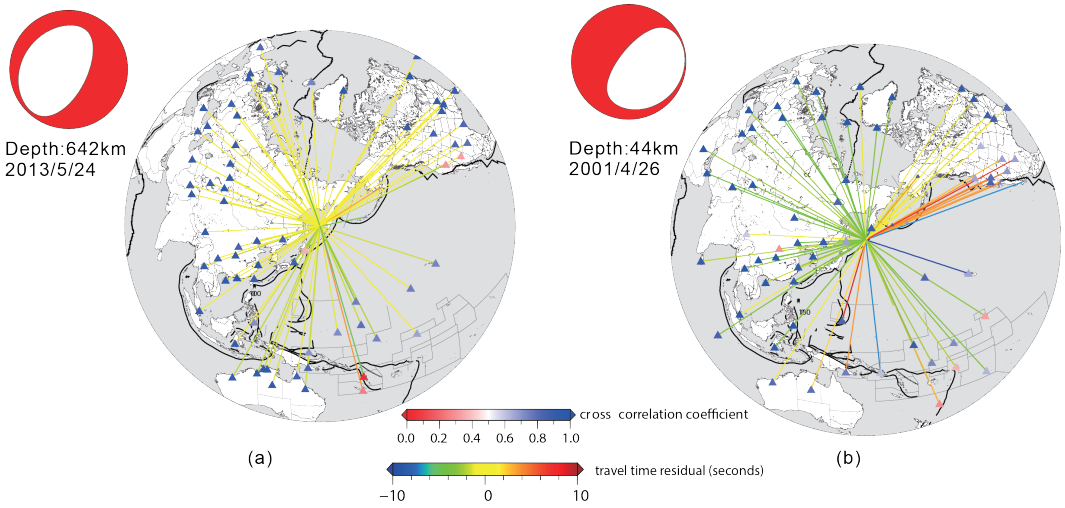


Figure 3.9: The global P wave travel time residual compared with PREM model estimated by CAP in frequency band 0.01 – 0.5 Hz for deep event (a) and shallow event (b). A deep event shows smaller travel time deviation comparing with a shallow event, which may indicate complicated subduction zone structure at shallower depth.

the 2013 Sea of Okhotsk Earthquake reaches a moment magnitude of 8.3 with a complex P-wavetrain, Figure 3.10. Here, we display a few example recordings along these two profiles, Figure 3.10. We have included the PASC recording as an example at other azimuths. In this case, the synthetic is separated into up-going vs. down-going excitation (Saikia and Helmberger, 1997). Note that at this range, the phase pP arrives ahead of PP but forms a complex pattern. This type of interference is obviously sensitive to 3D structure, which can be addressed with array data and complicates the use of depth phases. Nevertheless, the initial beginning of the pP phase samples the slab and arrives early at ranges up to 70° observed at the Pacific stations as predicted from our above results. Normally, distributed sources are modeled with idealized models of the Earth where only the direct P and depth phases are included, which is indicated in the red synthetics. In this particular case, only the direct P waveforms were used in the source inversion because of the concern over slab structural effects. The pP and sP are predicted from the distributed source model. Note that there are no arrivals between pP and sP while the observations display continuous signals starting with pP. The radiation pattern of the main event is similar to that of the aftershock but with a weaker PP. Figure 3.11 displays a comparison of the predicted synthetics for a single event for the PREM model along with the new tomographic model TX 2015 (Lu and Grand, 2016). Note that in this particular model, the upper part of the slab has been inserted and the tomographic

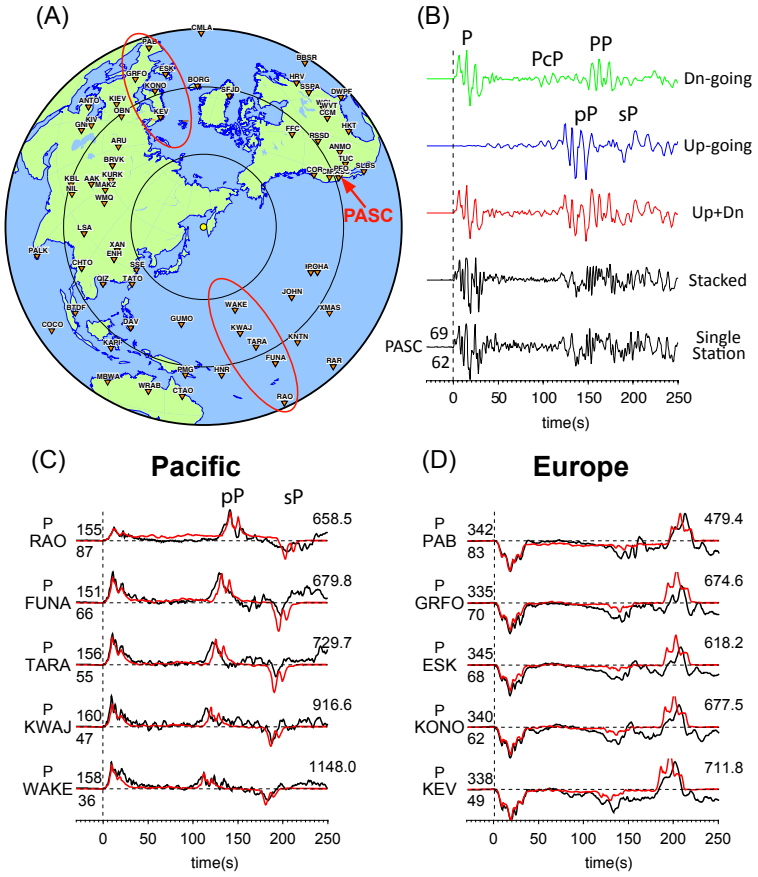


Figure 3.10: (A) Map view of the epicenter (yellow circle) and station distribution for the 2013 Sea of Okhotsk Earthquake. Stations toward Pacific and Europe are highlighted and shown in (C) and (D). (B) Vertical velocity waveform at PASC with data in black (single station and stacked) and the FK synthetics are shown in red (up+down), blue (up-going) and green (down-going). Station azimuth (upper) and distance (lower) are shown at the beginning of the data. (C), (D) show the displacement waveform of data (black) and synthetics (red) with station names indicate at the beginning of each record. Peak motion (in micro-meter) of data is shown at the end .

images adjusted accordingly. The 2D section displays the well-known fast velocities descending around the edge of the circum-Pacific along with the Large Low Shear Velocity Province (LLSVP). There is another slab-like structure near 110° since the path crosses the Fiji-Tonga region. Figure 3.11CDE displays the synthetics predicted from this 2D section. There are many small arrivals between P and pP caused by up-going reflections of both P and S waves into down-going precursors to pP, see Li et al. (2014). More important, secondary arrivals are the core-reflections as labeled. Note that the amplitudes are normalized to P by trace which makes the latter arrivals appear strong at the larger distances where P becomes weak moving into the shadow zone. The differential travel times (pP-P) from this model are similar to PREM because of the fast velocity corridor below the source effecting P more than pP. Thus more detailed studies will be needed to refine the slab structures which will probably require including the source information from larger events. For example, for the case of the large event, the 2013 $Mw$ 8.3 event, displayed in Figure 3.10 , one can perform a CAP analysis on the direct P and depth phases pP and sP. As in Figure 3.4 for the small event, the results of the big event are given in Figure 3.12. Some samples towards the east Europe which are expected to be more PREM-like are given in Figure 3.12A while the samples towards the west Pacific are shown in Figure 3.12B. The data is displayed in two columns for each direction. Note that the depth phases are lagged about 4s relative to the direct P wave in the Europe direction while there is no lag in the Pacific direction. The difference with the small event where there is negative lag in the Pacific direction may be ascribed to the finite source effect of the large event and uncertainties of source locations. But the relative shorter differential travel time in the Pacific direction than in the Europe direction is consistent with the small event. Here only the better waveform fits (high CC's) are included so that the timing shifts are reliable.

The up-going path sampling the slab are displayed in Figure 3.12. In this case, the depth phases are not lagged behind the direct arrivals. The apparent offset is about 4s in agreement with the smaller event, i.e. Figure 3.4. Unfortunately, the source directivity appears to overwhelm the slab waveform distortions.

In summary, we have examined the azimuthal behavior of depth phases and determined that the differential travel times (pP-P and sP-P) appear to be systematically shorter for paths sampling slabs. Secondly, it appears that slab shapes that increase their dip with depth are preferred, which allows the ray paths to remain in the slab longer.

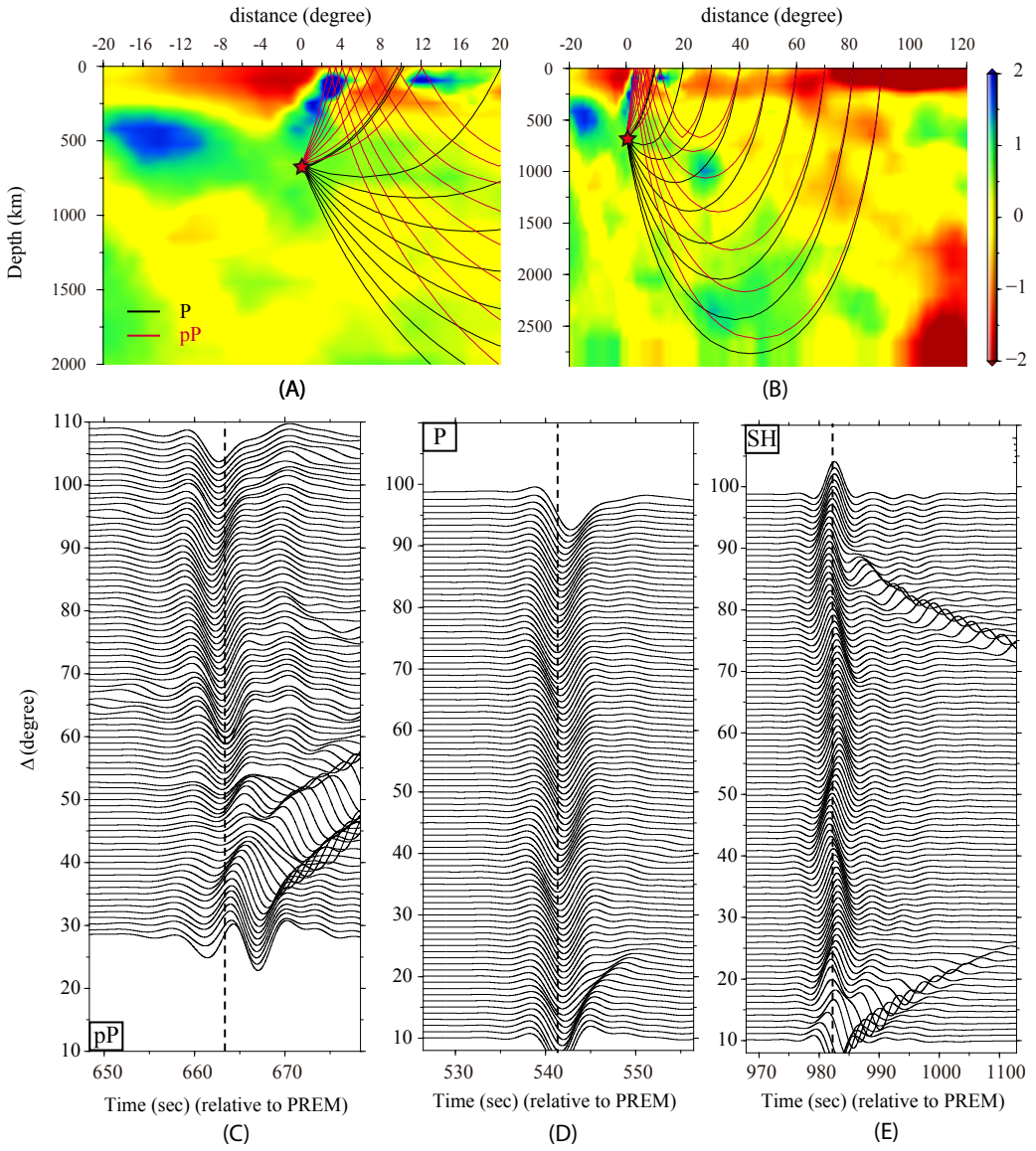


Figure 3.11: Figure 11A and 11B displays 2D cross-section along the pacific paths sampling the slab model embedded in Lu and Grand (2016), along with ray paths. Note the fast velocities sampled by the direct P wave. Figure 11 C,D,E displays the differential travel times normalized to PREM. The pP is not significantly early as suggsted for the aftershock results.

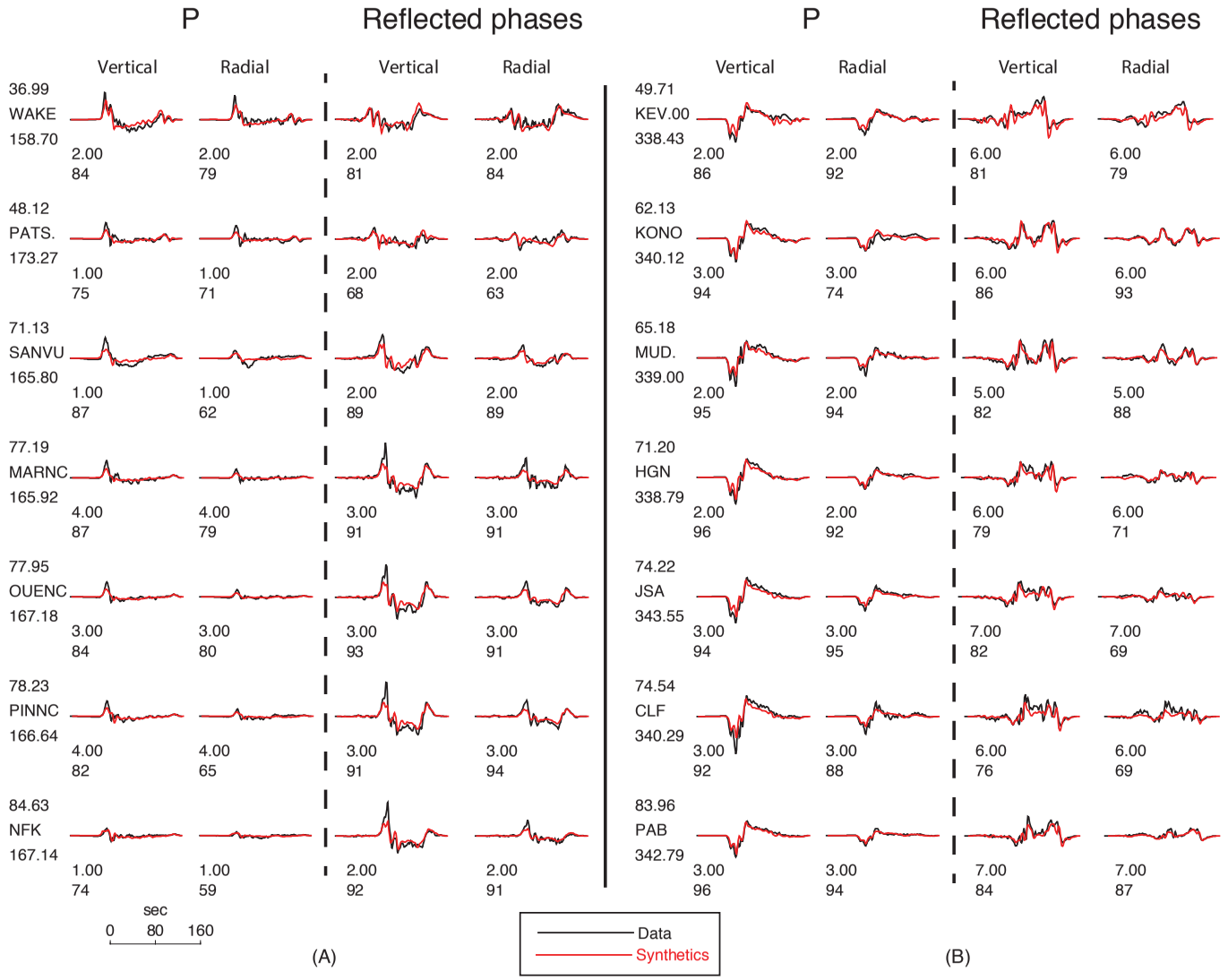


Figure 3.12: Paths towards the east Europe (A) and the west Pacific (B). The differential travel time between depth phases and direct P shows positive anormaly in (A) with depth phases arriving later while in (B) the differential travel time is nearly 0.



.

*Chapter 4*

# PATH CORRECTION OPERATOR

# ABSTRACT

Most finite fault inversions require the generation of a large number of synthetics. This becomes viable by excluding ranges except in the lower mantle where ray paths encounter smooth velocity gradients and become easily approximated at distance 30 degree to 90 degree. Thus, plane-wave approximations in the source region and at the receiver side can be convolved together along with a spreading operator, $Os(t)$, usually assumed to be a delta function along with an amplitude factor to generate synthetics. However the presence of slabs can introduce additional complexity as recently demonstrated (Zhan et al., 2014a). Hence, we develop path correction operators replacing $Os(t)$ that corrects for specific slab geometry and/or tomographic geometries. This procedure allows 1D synthetics to be convolved by this operator before comparing against observations. Numerical tests demonstrates the usefulness of this approach.

## 4.1 Introduction

A major issue in earthquake source inversions of great subduction zone earthquakes is understanding what is caused by rupture complexity and what is caused by earth structure. Both high frequency back projection and finite fault source inversions make unrealistic assumptions about such structure. The former assumes that the earth is a whole-space and does not have a free surface while the latter approximates the teleseismic data (30 °to 90 °) with plane wave geometric ray-optics. However, when we consider shallow earthquakes caused by subducting slabs, free-surface reflected phases interfere with primary arrivals and slab structures induce multi-pathing effects on the wave field which call both methods into problems. This study will address these issues where we introduce path correction operators.

As an introduction, we will give a brief review of the best recorded great event to date, namely the $Mw$ 9 Tohoku earthquake. This event had nearly a thousand high-rate GPS observations along with even more triggered strong motion recordings . However, all of the recordings are one-sided as are most subduction zone events situated on the edge of the Pacific ocean. Preliminary Reference Earth Model (PREM) (Dziewonski and Anderson, 1981) assumes an uniform crustal thickness of 24 km which is not appropriate for the Pacific basin (Figure 4.1). Thus when locating epicenter and determining origin time using teleseismic travel time which is very sensitive to shallow structures , there is a great deal of uncertainty introduced by this 1D approximation.

Chu et al. (2011) shows that improved epicenters can be achieved by using a well located master event which greatly changes the distributed source solution as displayed in Figure 4.3(AB) with a shift of the strongest offsets by over 20 km. Fortunately, this event was recorded by 5 off-shore type observations (Sato et al., 2011) which demonstrates large shallow rupture which confirmed the correctness of the calibrated method. Checkerboard slip modeling demonstrates the importance of this data in locating major rupture zones (Wei et al., 2012). The slip amplitude changes because of the depth dependence caused by the dipping fault structure, which here assumed to be on a 10 °dipping rectangle. Although this dip is likely to be variable with position (Zhan et al., 2012) which is also simulated by Simons et al. (2011). Of course, the main reason for such strong features in the inversion results involves the alignment methods when fitting synthetics to observations which involves timing shifts in the alignment of seismic waveforms. However, doing so will result in a shift of the whole slip patch due to the error introduced by simplifying a slab structure

with a 1D velocity model in the inversion procedure. To get rid of this artifact, one viable solution is to constrain the source location with GPS data.

Because the regional seismic data is the least sensitive to the poorly known velocity structure, Lui et al. (2015) chose a 1D layered model to invert for focal mechanism of small events in this region. Results of such an inversion on all the local seismic data for the big event are presented in Figure 4.1 allowing two distinct types of slip-rate functions, i.e. the simple cosine-half-cycle and the Kostrov like function (Kostrov, 1964) that allows a square root type singularity at the fault edge favored by dynamic considerations in panel B. Excellent results from 0 to 2.5 Hz are indeed produced from the using wavelet inversion scheme introduced by Ji (2002a) and Ji (2002b) without including global data. For the detail of this method see supplementary material (Wei et al., 2012).

In summary, this event is unique for both the information provided about the rupture process but also as an important constrain on seismic effects produced by 3D seismic structure. Since global waveform data was not used and if this source model is accurate, we should be able to predict global waveforms directly with some results highlighted in the lower panel of Figure 4.3.

These predictions are based on idealized assumptions generally used in teleseismic waveform inversions assuming that only the direct P and the depth phases pP and sP reflecting from a free surface control the shape. The phase PcP is weak at the distance ranges approaching 90 °so this is a reasonable assumption, but that is not so for ScS and especially for the radial motions (SV). In general, the fits are quite good at stations in northern Europe (azimuth 331-337) but less good in Southern Europe azimuth (azimuth 299-307) where a strong pulse near 75s occurs which is not predicted. Although an argument can be made that this phase is caused by scattered pP from the ocean bottom interaction with the radiation from the strong asperities, here we will concentrate on expanding the methodology to correct for path effects. We start with a brief review of how finite sources are presently determined following the generalized ray approach. This is followed by an introduction of new simulation methods that can generate short period seismograms. Next, the concept of path correction operators is discussed. We end with a discussion of how well-known finite sources can be used to test 3D earth models.

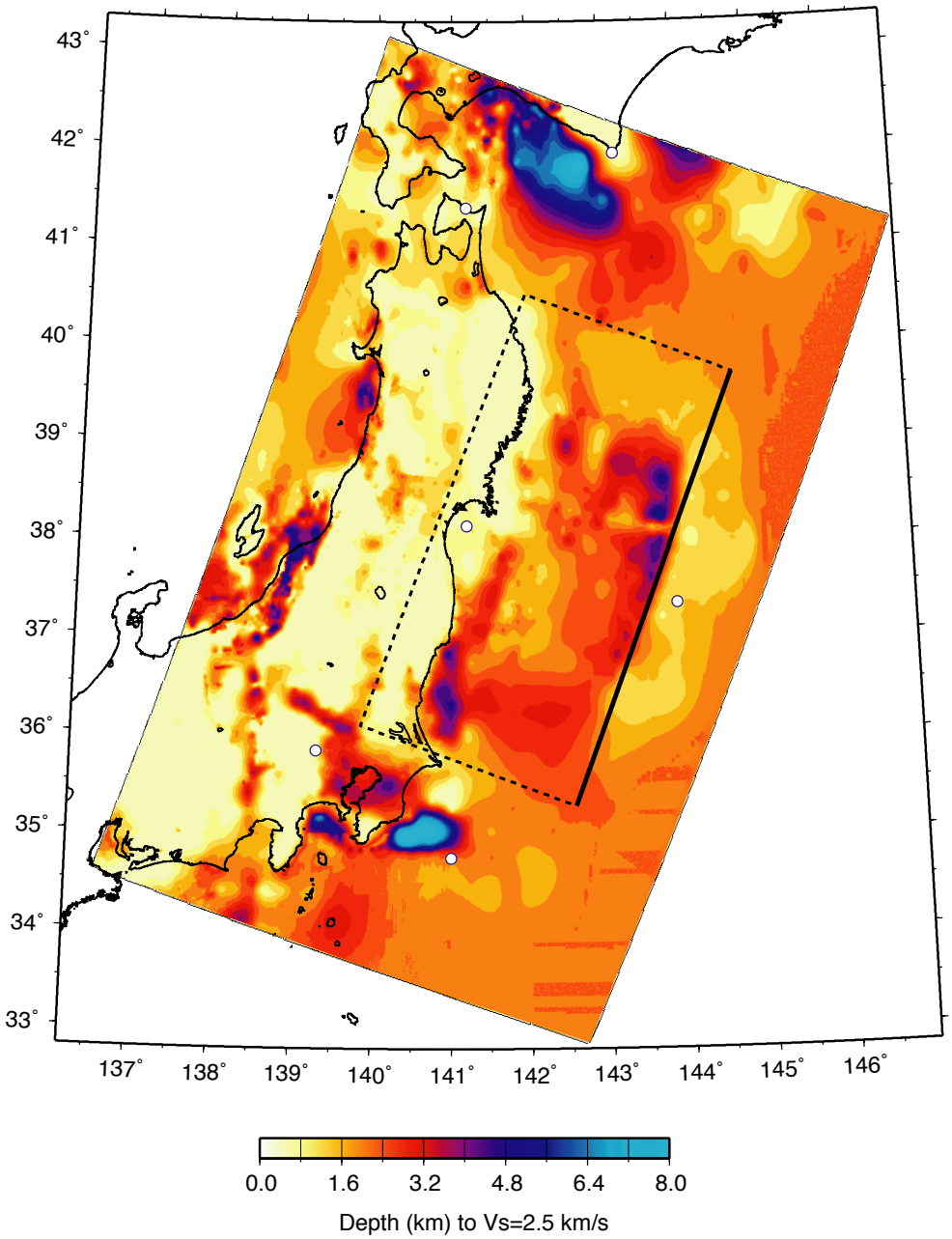


Figure 4.1: Depth of Vs=2.5km/s in the Honshu region, the 3D velocity model is obtained from NIED (National Research Institute for Earth Science and Disaster Prevention). Note the 3D model stops at about 15km, thus we use a 1D model for deeper depth, which is the same as that used during the slip model inversion.

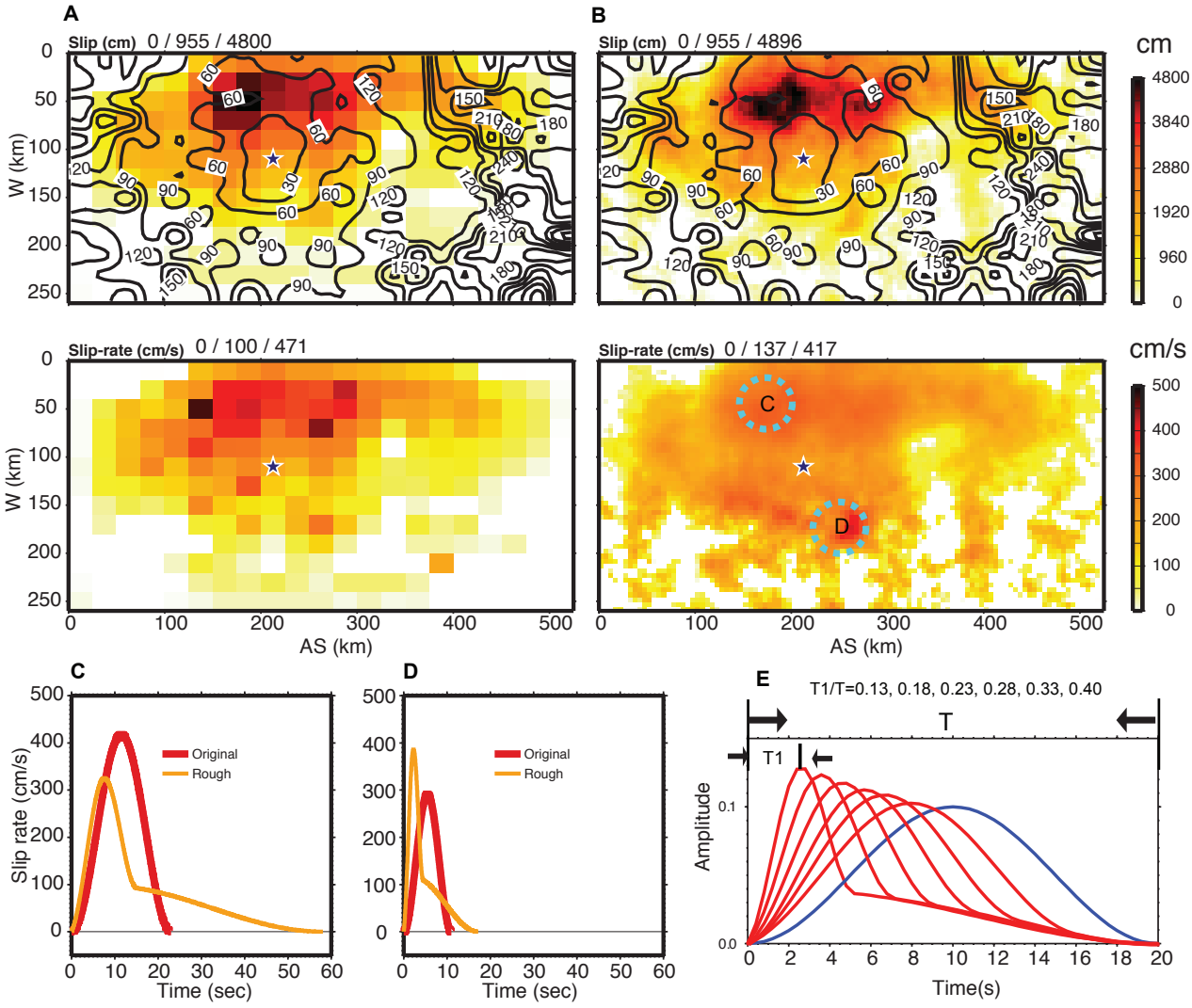


Figure 4.2: (A) Slip model obtained by inversion, the upper panel shows the slip distribution in the rectangle fault plane with contours indicating the rupture time. The lower panel shows the corresponding slip-rate which is defined as the slip divided by the rise-time. (B) The revised slip model based on the scheme described in Graves and Pitarka (2010). The two circles indicate the sub-faults with their source time function shown in (C) and (D). (C) The left panel shows the shape of two source time functions used for the inversion (original) and for forward calculation (rough), respectively. The length of the rough source time function is proportional to the square root of the slip amplitude. The right panel displays the amplitude spectra of the corresponding source time function. (D) Similar as (C), here an extra scaling factor (0.5) is applied to determine the length of the revised source time function (rough), thus this model has larger amplitude spectra at high frequency bands. (E) Source time function with flexible T1/T ratio (red) along with cosine-like source time function (blue) .

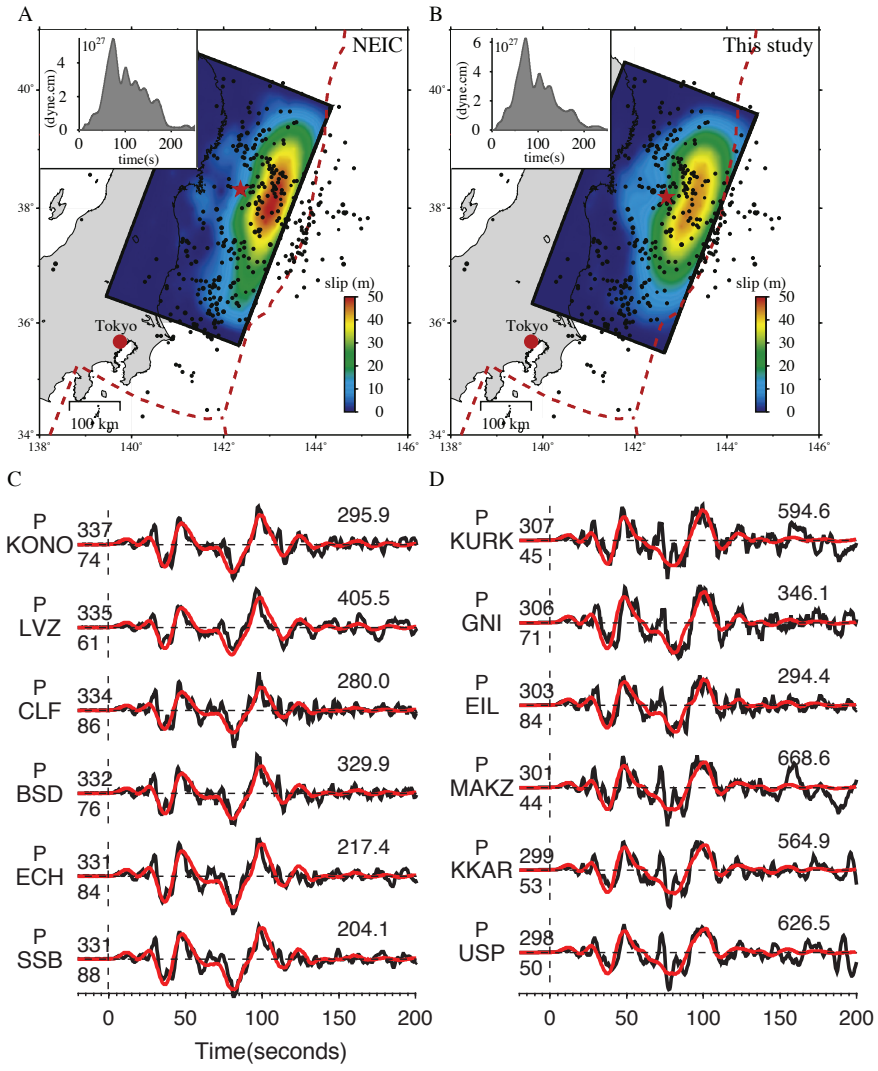


Figure 4.3: Modified from Chu et al. (2011) 0.01 – 0.5 Hz for deep event (a) and shallow event (b). A deep event shows smaller travel time deviation comparing with a shallow event, which may indicate complicated subduction zone structure at shallower depth.

## 4.2 Methodology

Because we are dealing with source inversion, we focuses on body waves (P and SH waves) which are the most commonly used in high resolution source inversions. The earliest efforts involved the importance of including the depth phase and the generation of synthetic seismograms (Langston and Helmberger, 2007). Following this approach, we compute the responses for the three fundamental types of earthquakes, namely a pure strike-slip , a dip-slip and a dip-slip viewed at 45 °. Any other source mechanisms can be obtained by a linear combination of these three fundamental modes. We start with a simple approximation for the vertical component involving a free surface.

$$W(r,z,t) = \frac{M_0}{4\pi\rho_0}\sum_{j=1}^{3}[C_j(p_0)\delta(t) + C_j(p_0)R_{pP}(p_0)\delta(t-\Delta t_{pP}) + SV_j(p_0)\frac{\eta_\alpha}{\eta_\beta}R_{sP}(p_0)\delta(t-\Delta t_{sP})]A_j\frac{R_{PZ}(p_0)}{O_s(t-t_0)} \tag{4.1}$$

with $\eta_\alpha$ and $\eta_\beta$ the vertical slowness for the ray parameter $p_0$ connecting the source and the receiver. The first term represents the direct P-wave, followed by the pP reflection lagged by $\Delta t_{pP} = 2H(\eta_\alpha)$ and reduced by the reflection coefficient $R_{pP}$ and the $sP$ arrival, $\Delta t_{sP} = H(\eta_\alpha + \eta_\beta)$. The $C_j(p_0)$ and $sv_j(p_0)$ represent the vertical radiation patterns while $A_j(\Theta, \delta, \gamma)$ contains the azimuthal correction in terms of strike = $\Theta$, dip= $\delta$ , and rake = $\gamma$ . The $R_{pz}(p_0)$ is the receiver function for arriving P-wave with z(vertical component), see Helmberger (1983) for details. The $O_s(t-t_0)$ represents the decay with distance or spreading factor(SF). $\Delta t_{pP} = 2H(\eta_\alpha)$ , time lag of $pP$ and $\Delta t_{sP} = H(\eta_\alpha + \eta_\beta)$ , time lag of $sP$ .

For a whole space, the $SF$ or $O_s(t - t_0) = \frac{d}{dt}(\frac{H(t-t_0)}{R}) = \frac{\delta(t-t_0)}{R}$ where $t_0$ is the travel time, and $R$ is the distance. Synthetics produced by this generalized ray method demonstrates the adequacy of the geometry spreading approximation which is commonly used, mainly $O_s(t) = (\alpha \tan i)/(r_0^3 \cos(i) \sin\Delta|\frac{d^2T}{d\Delta^2}|)$ $i$ = take off angle , $T$ is the travel time and $\Delta$ the distance in degrees (Bullen, 1965). For distances between 30 °and 90 °, see Helmberger (1983).

Crustal corrections can be added by replacing the simplified depth phases $R_{pp}$, $R_{sp}$ and the receiver function with plane-wave propagators assuming $p_0$ i.e. $K^2$ Although this assumption can fail for deep events when plane-wave theory or first motion approximation breaks down, Helmberger (1983).

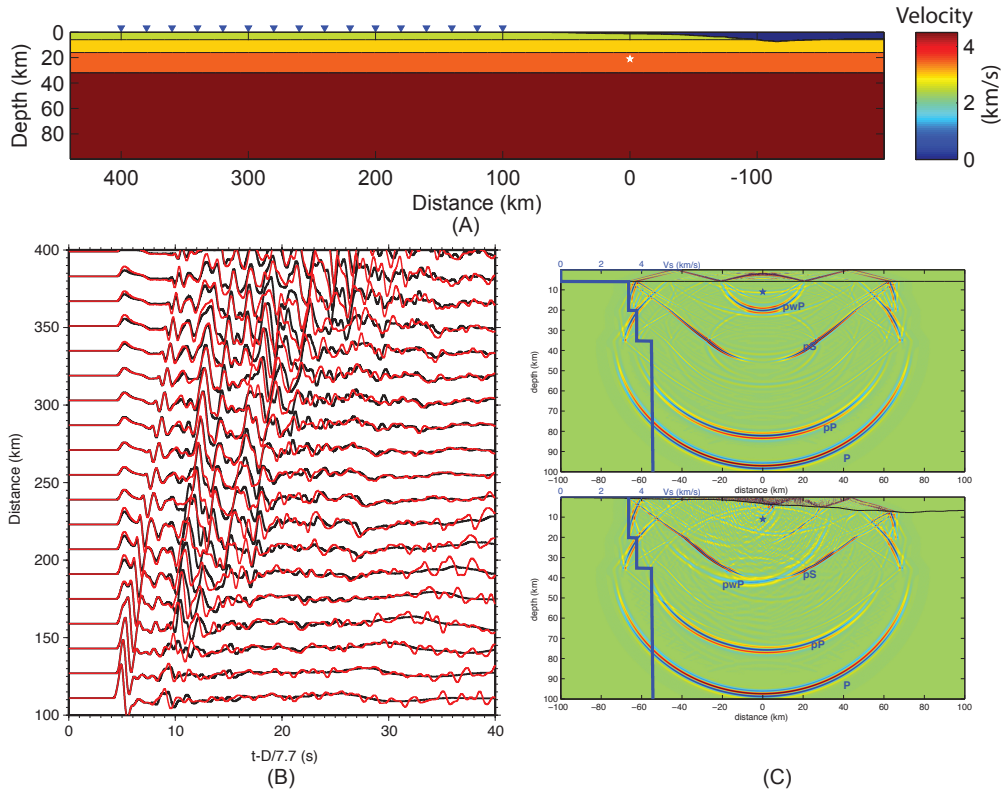


Figure 4.4: (A) Vs model with water layers. White star shows the position of the sources position and triangles indicate the receivers . (B) Vertical displacement for the model with water (red) and without water (black). The waveform looks similar because the arrivals trapped in the ocean are transmitted downward into the mantle and does not go to the local receivers. (C) Snapshot of vertical velocity from a flat water model (top) and a sloping water model (bottom). The source is an explosion. The water phases are clear. A useful procedure for locating off-shore earthquakes is to determine the water depth directly above the event by modeling the various water phase arrivals, PwP etc. Since the water depths are well known, it can help constrain the location (Chu et al., 2011)

## 4.3 Advances in simulation

Global seismic tomography is making major gains with comparisons of 1D and 3D synthetics online for many significant earthquakes assuming RCMT point source excitation . This proves effective at longer period ($> 12s$) applying the 3D Spectral Element Method (Komatitsch and Tromp, 2002). Since synthetic waveforms from 2D cross-sections assembled from 3D models generally agree (Chen et al., 2007). The shorter periods involved in distributed ruptures can be addressed. An example application of the above code is presented in Figure 4.4 for a simplified section containing an oceanic edge. Note that the water bottom arrivals do not reach land but

are deflected to more distant stations as predicted by analytical codes (Helmberger, 1983). This seems to be the reason why simple 1D model are effective in simulation strong motions as in the above Tohoku Earthquake study. However, local ocean bottom structure can greatly complicate their distant arrivals as discussed by Chu et al. (2011). This 2D code has also been used extensively in Chu et al. (2012) with some results given in Figure 4.5.

The panel on the left of Figure 4.5 displays a tomographic image for a 2D cross section along the Washington-Oregon border showing the Juan De Fuca slab after Schmandt and Humphreys (2010) assuming AK135 model. Their model is transformed into the panel on the right that is more consistent with regional travel times along with waveform matching. Note the slab is both fast and sharp.

The model is consistent with oceanic structures on the left and agrees with event seismicity maps indicating the upper slab edge. The structure changes considerably to the north and south in order to satisfy the US array data provided by the well recorded 2008 Nevada earthquake, see Chu et al. (2012). Analytical ray-based methods such as WKM (Ni, 2003) can be used directly on existing tomographic models. The method has been benchmarked against pseudo-spectral methods (Ni, 2003) for 2D models and for 3D, using diffraction corrections, Helmberger and Ni (2005), as reported on Ni et al. (2005) against SEM results.

As global images develop, we can resolve more detailed images of slab structures as they encounter the lower mantle (Sun and Helmberger, 2010; Sun et al., 2016) As global seismic images become better developed, we can resolve a great deal of variation at depth. This means that the geometry involving events and stations becomes particularly important. Note that injecting slabs into reference models produces significant issues, Lu and Grand (2016). They compute global synthetic seismograms down to 12s for apriori slabs which removes slab wave guide distortions, but yields significant source mislocations depending on recording geometry especially for South American events. Testing existing global models maps into errors up to 0.5% in S velocity anomalies even in the lower mantle depending on region and particular methodology used in tomography.

Furthermore, adding Pn travel times along with 3D ray tracing resolves some slabs in the tomographic upgrade by Simmons et al. (2012) and Simmons et al. (2015). In some cases, out of plane model complexity is important. For example, at short periods, evidence of lateral variation rapidly develops. Such characteristics for western United States have been examined in terms of multipathing by Sun and Helmberger

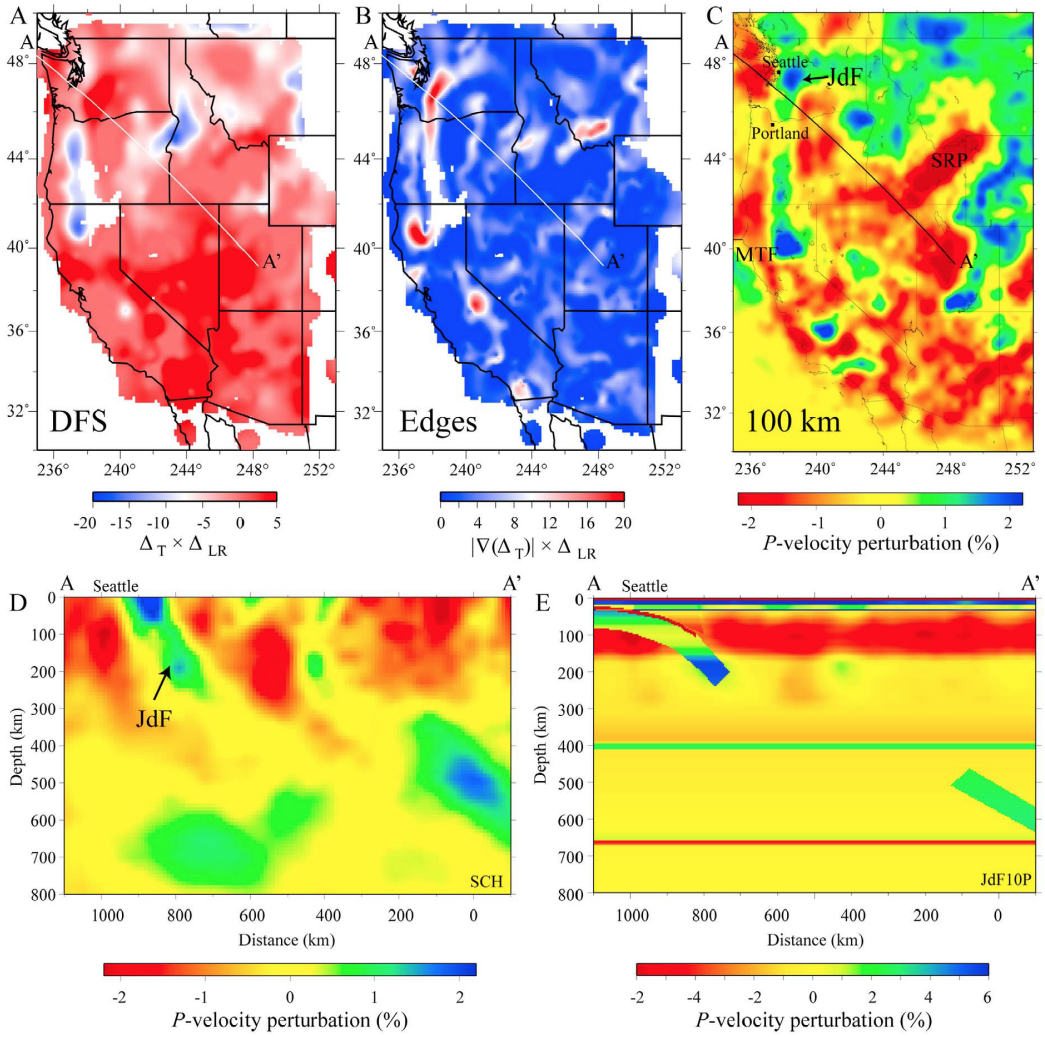


Figure 4.5: Figure modified from Chu et al. (2012). Seismic structures derived from observed waveform complexities showing (a) dipping structure and (b) the edges of the Juan de Fuca Slab (Sun and Helmberger, 2010).(c) Map view of a tomographic image at 100km for the western United States (Schmandt and Humphreys, 2010). The location of JdF slab derived from waveform complexity agrees with the slab from travel-time tomography.(d) We show tomographic P wave velocities of the Juan de Fuca (JdF) slab from Schmandt and Humphreys (2010) and (e) the hybrid model constructed from forward modeling of waveform data and travel times. The location of the cross section is shown as AA' in the map. Note the difference between the color scales in Figure 2d and 2e. In Figure 2c, MTF refers to the Cape Mendocino transform fault and SRP is the snake River Plain.

(2010) , where both in-plane and out-of-plane complexity is observed in the US-Array data for body waves. To model such 3-D features , we can calculate several 2D sections and then combine them using diffraction methods (Helmberger and Ni, 2005). Synthetics generated in this way match 3D SEM results for record section sampling the edges of the African Large Low Shear Velocity Provinces (LLSVP) (Ni et al., 2005). Their model LLNL has been used effectively in developing sharp features in Ko et al. (2017). An example record section connecting a deep event beneath SA to USArray is displayed in Figure 4.6. Here the results from analytical and numerical are in excellent agreement . Adding sharper-edges causes the WKM results to differ which can be fixed as presented by Ko and Zhan 2017. at the AGU fall meeting.

### 4.4 Path correction operator

In this section we address the adaptation of those new methods to generate some new tools for studying earthquake excitation, in particular, those along subduction zones.

For shallow subduction zone earthquakes , the ray paths involving P and surface reflected phases sample similar paths as illustrated in Figure 4.7. Figure 4.7A displays the placing of a slab-like structure into a reference model. Figure 4.7B contains an image of the wavefield with P traveling down the slab followed by the reflected phases. A diagram of the simulation is given in Figure 4.7C which the idealized P pP and sP combination for the reference model on the left being convolved with a slab operator to construct the corrected response. Note that adding up point source solutions to generate a distributed finite source is a simple linear process and such an operator can provide a useful tool for correcting for path effects. In this section, we calculate the effect of the slab structure on the whole seismogram by calculating only its effects on P waveform and make it an operator $O_s(t)$. Then we convolve this $O_s(t)$ with P wave train (including surface reflections for shallow event) of the synthetics calculated by 1D structure (Figure 4.7(C)). Here, all the synthetics are generated by the 2D Finite-difference method (Li et al., 2014).

The finite frequency effect is displayed in Figure 4.8. When the seismic wave length is comparable to the slab width (Figure 4.8C), the travel time effect become blurred and the boundary reflections and refractions merge. At still even longer wavelengths, the slab structure is basically ignored by the wavefield (Figure 4.8D). Only at the shorter wavelength (Figure 4.8B ) does the slab becomes obvious. The sensitivity

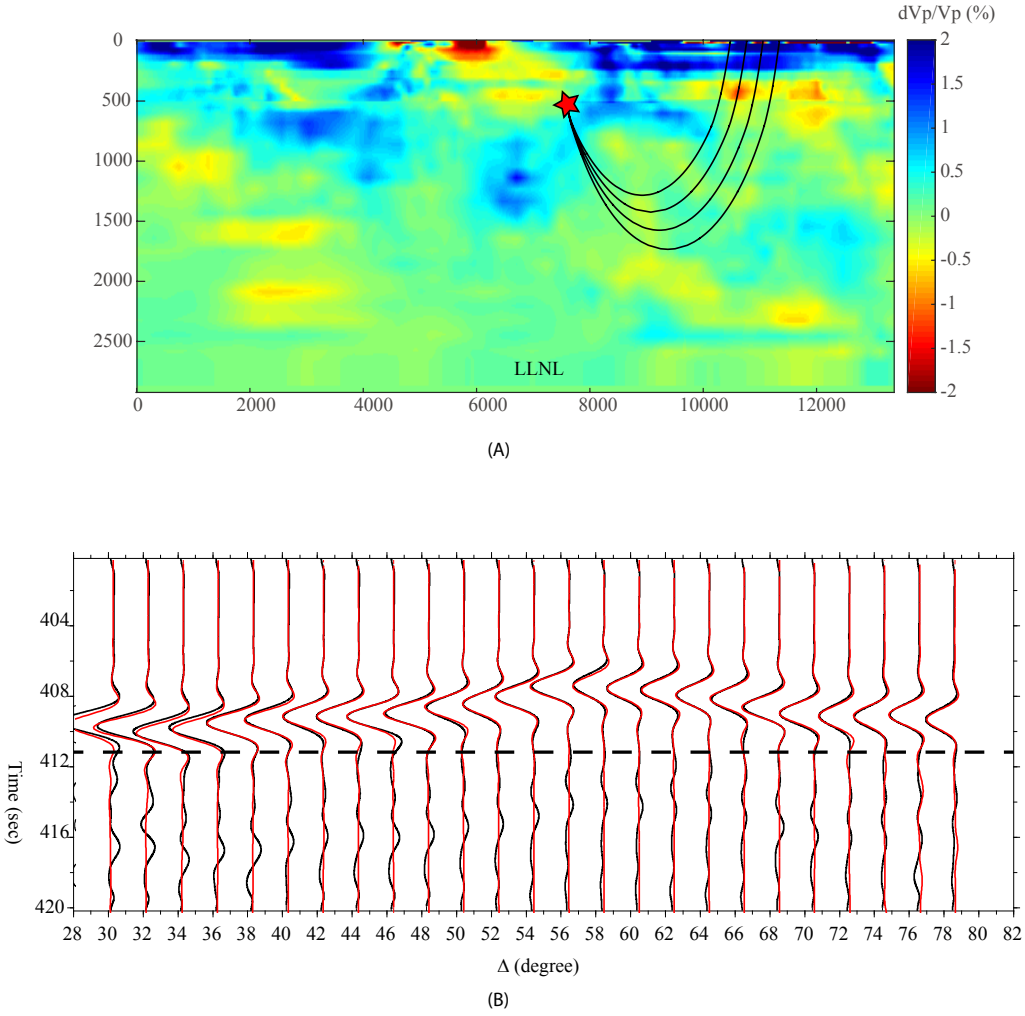


Figure 4.6: 2D model and waveform comparisons. (A) 2-D cross-section of the LLNL model from South America to the USArray. The red star indicates the event location used in the simulation. The black lines represent the 1-D raypaths at 50,55,60,65 degree away from the source.(B) The waveform comparison between WKM (red) and FD (black) using LLNL model. All traces are low-pass filtered with a cutoff frequency of 0.4 Hz.

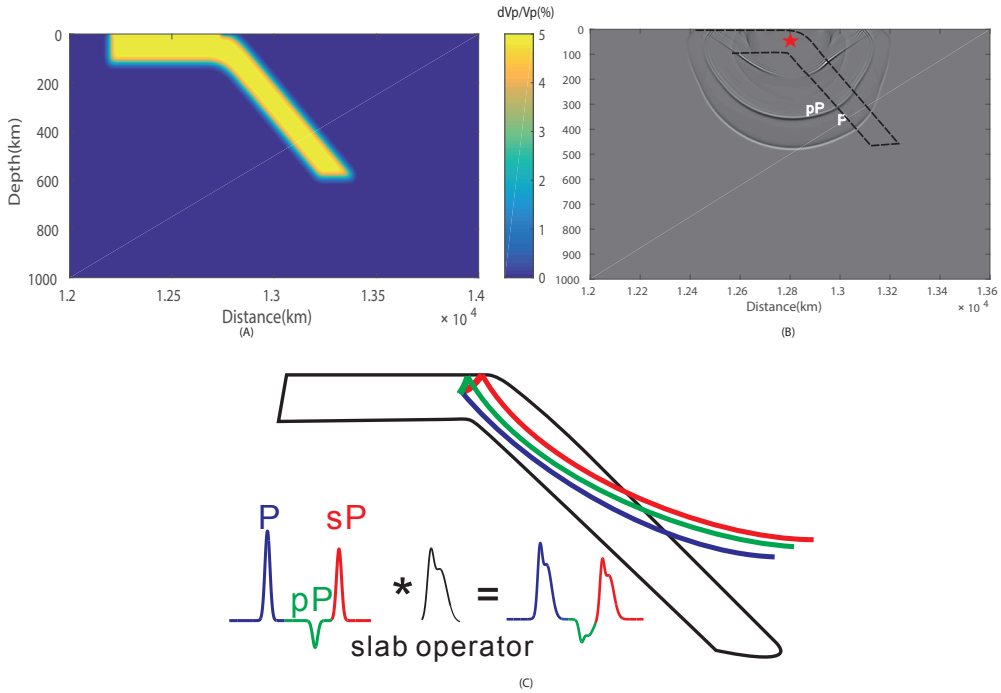


Figure 4.7: (A)(B) For shallow earthquakes, the ray path of the direct phases and surface reflected phases are traveling through similar paths. So we should assume that the slab effect on those phases to be similar. Depending on the detailed geometric structure of the slab, when the ray is entering or leaving the interior of the slab, multipath effect is emphasized. We demonstrate concept of a slab operator in (C).

at sill larger periods in 3D last been explored in Lu and Grand (2016) where the 3D point source approximations or RCMT is assumed.

In Figure 4.9A we present 1D synthetics compared to 2D synthetics computed directly, the slab operator displayed in Figure 4.9B along with a comparison of the simulated slab synthetics in Figure 4.9C. Note that the slab effect develops near 50 ° and less as in the example presented earlier Figure 3B. Changing the dip of the slab shifts the pattern significantly as predicted. The example operators are appropriate for the focal depth of 40 km and 80 km, where the distance travelled along the slab causes the most delay for the shallowest event.

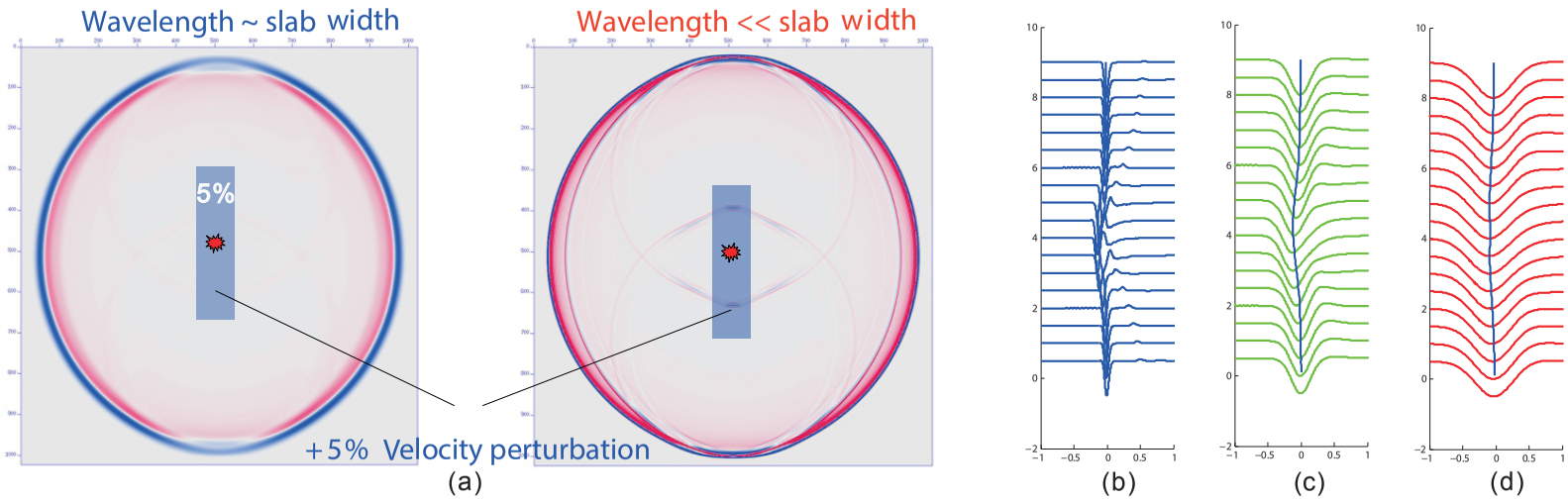


Figure 4.8: Shows the finite frequency effect of a thin high velocity slab on seismic wave field.(a) is a slab model 50km wide with uniform velocity perturbation of 5%. In (b)(c)(d) we use three sources with three different wavelengths:10km, 50km and 200km. At very high frequency(b), the travel time of the slab is very clear. There are also reflected and converted phases generated at the boundary of the slab which can be explained by classical ray theory. When the seismic wave length is comparable with slab width (c), the travel time effect is blurred. At even longer wavelength, the slab structure is ignored by the wave field(d).

## 4.5 conclusion

We reviewed issues encountered in finite source modeling involving large subduction zone events. Essentially, locating the origin and strongest off-set prove difficult without the use of timing corrections and/or complete GPS coverage which is not available for oceanic environments. Moreover, by allowing timing shifts when aligning synthetic seismograms with observed waveforms we lose some more important information. In summary, we need better Green's functions and increased data coverage at all ranges and the ability to include slab effects. Both analytical methods such as WKM (Ni, 2003) and numerical methods such as 2D Finite-difference method (Li et al., 2014) are available to address the issue as introduced. Here, we discuss the development of the slab operators that can be used to account for the first order effects of a dipping slab. This simplification allows present plane wave approximation to be used more effectively. We also introduced possible correction operators where 2D and 3D effects can be applied and used in testing the trade-offs between rupture complexity and the Earth's structure. Some of such applications was included in Chapter 3 in terms of timing shifts for reflected phases i.e. pP and sP where slab effects are obvious.

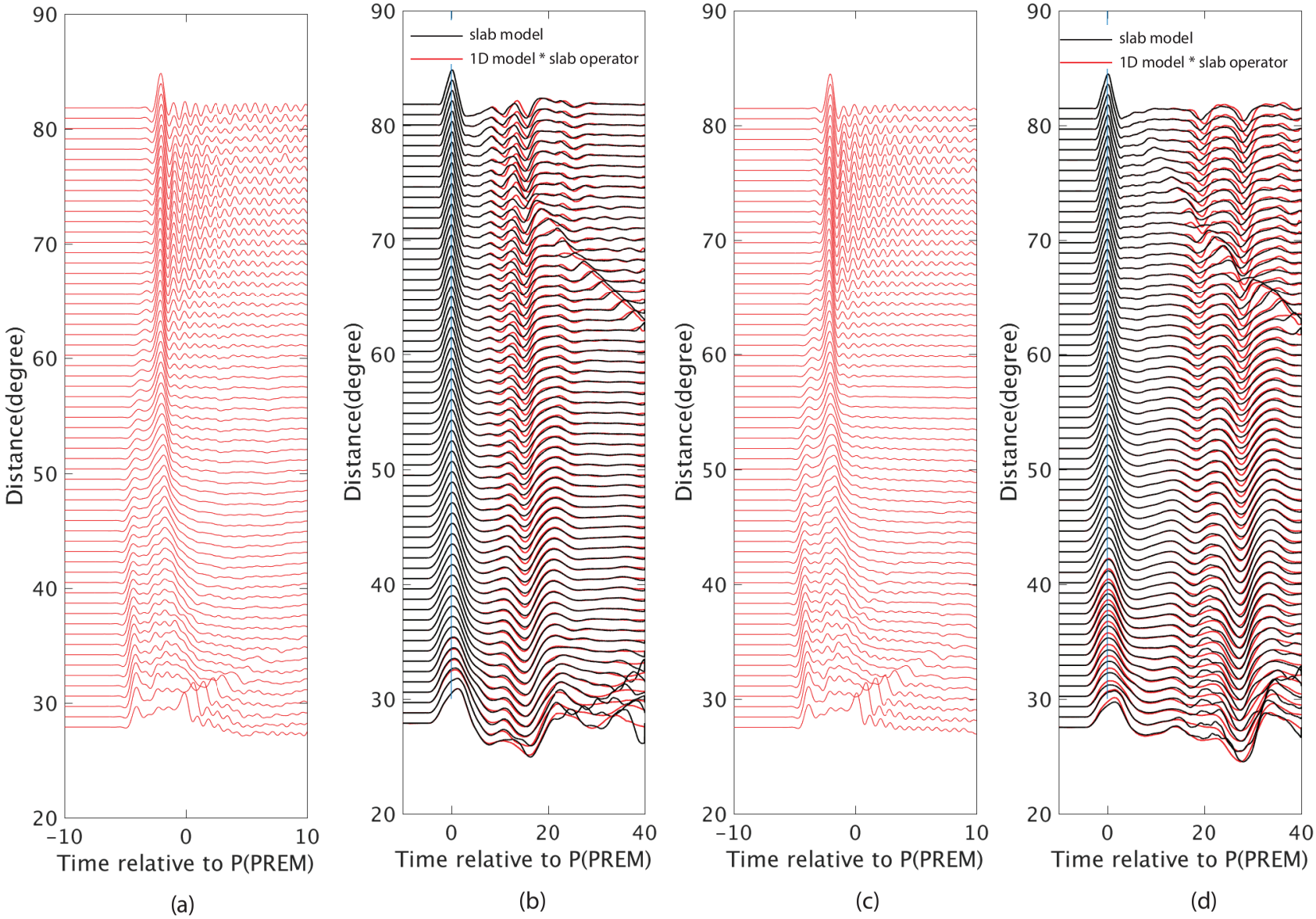


Figure 4.9: (a) (c) Slab operator made by deconvolving P phase generated by slab model from that generated by 1D PREM model. (a) for a source depth of 40km and (c) 80km. (b) (d) Comparison of the slab model synthetics with that generated by convolving 1D PREM synthetics with the slab operator. Here the wavetrain is composed of P pP and sP phases.(b) for a source depth of 40km and (d) 80km.

*Chapter 5*

# DYNAMIC RUPTURE SIMULATION OF THE 2015 MW 7.8 GORKHA EARTHQUAKE

## 5.1 Introduction

High frequency back projection and finite fault inversion have revealed depth dependent rupture processes during the 2015 Mw 7.8 Gorkha, Nepal earthquake. Back projection of teleseismic P waves at frequencies around 1 Hz reveals radiation spots along the down dip edge of the rupture zone identified by finite fault inversions based on teleseismic and local continuous GPS data at much lower frequencies, below 0.2 Hz (Avouac et al., 2015; Yagi and Okuwaki, 2015; Grandin et al., 2015). Bayesian finite source inversion, which provides not only a best fitting model but also the uncertainty around that model, shows that the down-dip portion of the rupture has larger roughness and uncertainty in slip, rupture speed and rise time than its up-dip portion (Yue et al., 2017). Depth dependent rupture processes have been observed in several large subduction megathrust earthquakes (Lay et al., 2012) such as the 2004 Sumatra-Andaman earthquake (Ishii et al., 2005) and the 2011 Tohoku earthquake (Meng et al., 2011). In addition, a broad spectrum of intermingled fast and slow slip processes ranging from non-volcanic tremor to slow slip events (Ide et al., 2007) occur near the seismic-aseismic transition zone, which suggests a complicated mixture of stable and unstable fault zone properties at those depths. Indeed, models accounting for heterogeneous fault properties have reproduced key aspects of this spectrum of slip behavior (Luo and Ampuero, 2017). It is thus suggested that fault heterogeneities play an important role in co-seismic rupture processes. Specifically, they may contribute to stronger high frequency radiation at depth during large earthquakes.

While finite fault inversions can generate source models that explain low frequency data, they face major challenges in simulating high-frequency ground motion, which is of great importance for hazard analysis. For example, Avouac et al. (2015) conducted finite fault inversion based on teleseismic waveforms filtered from 0.01 to 1 Hz and included in the objective function of the inversion method (Ji, 2002a) constraint terms that penalize the high-frequency components of the model. Dynamic rupture simulations, incorporating fault friction derived from laboratory experi-

ments, aim at generating more physically-consistent rupture models and broadband ground motions. Because dynamic rupture simulation needs as input the initial stress distribution on faults at fine scales that are not resolved by stress estimation techniques, previous physics-based studies of near field strong motion used stochastically generated initial stresses (Guatteri, 2003; Liu et al., 2006; Ripperger et al., 2008; Andrews and Ma, 2016). These stochastic stress models (Mai and Beroza, 2002), while statistically consistent with earthquake observations (Andrews, 1980), do not consider stress concentrations at the edge of the asperities which are very efficient in generating high frequency radiation (Madariaga, 1977; Kame and Uchida, 2008). Here we develop dynamic source models combining large-scale features constrained by finite fault inversion and stochastic short-scale features guided by earthquake cycle models.

## 5.2 Model

**Heterogeneous stress model motivated by earthquake cycle simulations**

To gain insight on the key characteristics of stresses on a fault that hosts earthquakes of various sizes, we simulate multiple earthquake cycles on a fault with heterogeneous frictional properties. For computational efficiency we adopt the quasi-dynamic approximation and use the software QDYN (Luo et al., 2017b; Luo et al., 2017a). The frictional behavior on the fault plane is governed by the classical rate-and-state friction law:

$$\frac{\tau}{\sigma} = \mu^* + a \ln(\frac{V}{V^*}) + b \ln(\frac{V^* \theta}{L}) \tag{5.1}$$

where $\tau$ and $\sigma$ denote the shear and normal stress, respectively, $\mu^*$ is the reference frictional coefficient at reference slip velocity $V^*$, $a$ and $b$ are friction parameters, $V$ is slip velocity and $\theta$ the state variable. The latter evolves according to the "aging law" (Dieterich, 1979; Marone, 1998):

$$\frac{d\theta}{dt} = 1 - \frac{V\theta}{L} \tag{5.2}$$

where $L$ is a characteristic slip distance. The fault is said to be velocity-strengthening when $a > b$ and velocity-weakening when $a < b$. We set up a canonical seismogenic zone model with a velocity-weakening zone surrounded by velocity-strengthening zones (Luo et al., 2017b). We set a uniform normal stress $\sigma = 75$ MPa, shear modulus $\mu = 40$ GPa and characteristic slip distance $L = 0.04$ m. We add small circular patches with $L = 0.005$ m at the down-dip portion of the seismogenic zone. A circular asperity exhibits stick-slip behavior if it is velocity-weakening and has

a radius greater than a critical nucleation radius (Rubin and Ampuero, 2005; Chen and Lapusta, 2009; Noda et al., 2013) given by, when $a/b > 0.5$:

$$L_{nuc} = \frac{\pi \mu L b}{4\sigma(a-b)^2} \tag{5.3}$$

In our simulation the critical nucleation radius is 1.255 km in the small circular patches and 10.04 km outside them.

Creep gradually penetrates from the aseismic zone into the seismogenic zone. The small asperities are loaded by the approaching creep front and their response depends on their radius relative to the critical radius (Chen and Lapusta, 2009). Relatively large asperities generate repeating small earthquakes, which leave high residual stresses around the edges of their ruptures and low stresses inside. These stress heterogeneities persist until very close to the occurrence of the next event (Figure 5.1C). The stress inside and around slightly super-critical asperities is smoother, and either lower or higher than the background stress depending on time advance within their cycle (Figure 5.1D). This multi-cycle simulation will serve as a qualitative guide for setting heterogeneous pre-stresses for dynamic rupture simulation in section 5.2.

**Dynamic rupture simulation**

**Model geometry and mesh generation**

We consider a planar 7° dipping thrust fault and high accuracy surface topography (Etopo2, 2006) (Figure 5.2, A and B). We use the spectral element method software SPECFEM3D (Komatitsch and Tromp, 1999). To facilitate this work, we extended the dynamic rupture solver implemented by Galvez et al. (2014) to take advantage of GPU acceleration (Komatitsch et al., 2010) which can usually lead to a 90% reduction in computation time on Caltech's FRAM cluster. We use 5-th order spectral elements. Far from the fault we use a coarse mesh with average element size of 1000 m. Within 10 km of the fault plane we refine the mesh down to an average element size of 330 m on the fault, equivalent to an average node spacing of 80 m. To be consistent with Yue et al. (2017), we use the 1D velocity and density model given by Monsalve et al. (2008). Given the minimum wave speed in the model is 3.2 km/s, we can resolve waves with frequencies up to 10 Hz near the fault and 3 Hz far from the fault with 5 grid points per wavelength. Following Galvez et al. (2014), we wrap the simulation domain by a semi-spherical region in order to more effectively absorb outgoing seismic waves.

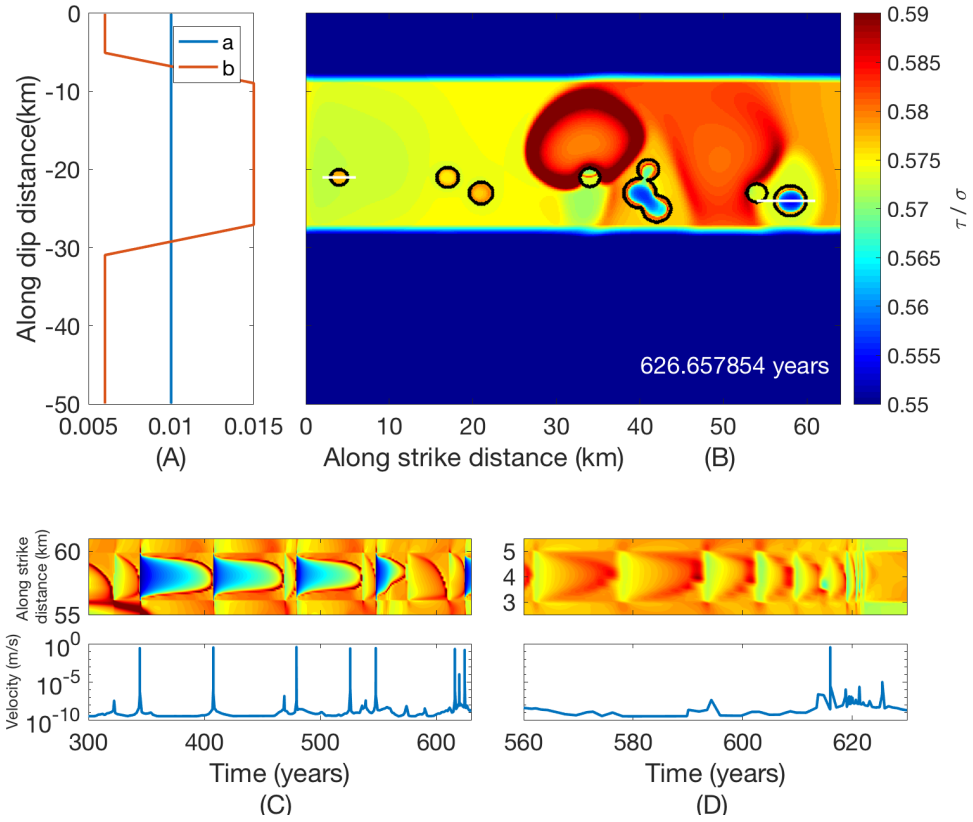


Figure 5.1: Multi-cycle quasi-dynamic simulation on a rate-and-state model of fault containing small asperities. (A) Depth dependence of friction parameters $a$ and $b$. The seismogenic zone is in the depth range where $a < b$. (B) Spatial distribution of shear stress on the fault (normalized by normal stress) right before a large event that ruptures the whole seismogenic zone. (C) Top: Spatio-temporal evolution of shear stress along a horizontal cross-section through a large asperity shown by a long white line in (B). Bottom: temporal evolution of slip velocity at the center of the asperity. (D) Same as (C) but for the small asperity indicated by a short white line in (B).

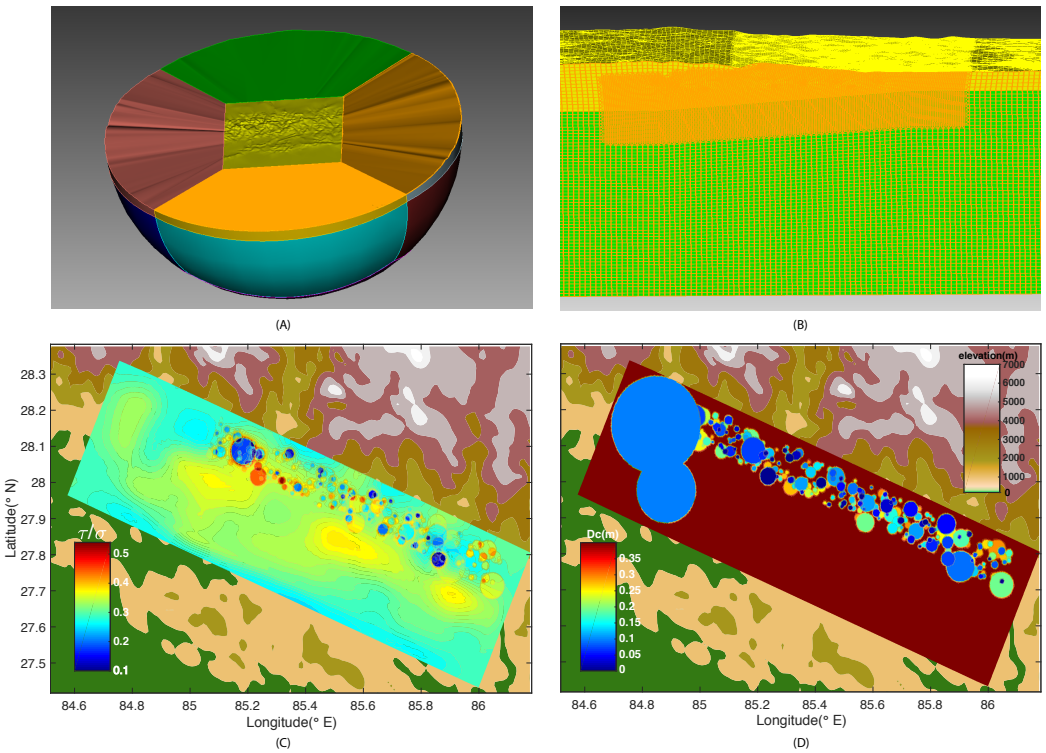


Figure 5.2: Model and initial conditions for the dynamic rupture simulations.(A) simulation region with surface topography in the middle cubic with semi-sphere wrapped regions which is aimed to absorbing out-going seismic wave.(B) Cross-section of the meshed mega-thrust region. The mesh is specially refined near the fault plane. (C) Small stress patches at bottom of the seismogenic zone are superpositioned onto the long wavelength stress field computed from kinematic rupture model. The stress patches are randomly generated with their radius following polynomial distribution with power -2.5. (D) $D_c$ value in these small patches are also stochastically perturbed downward.

### Heterogeneous pre-stress on the fault

We set the large-scale stress conditions before the earthquake based on finite-fault source inversion results and assumed friction strength. We compute the spatial distribution of static stress drop on the fault plane from the Bayesian mean slip model obtained by Yue et al. (2017). We then add the computed stress drnaop to the dynamic friction $\mu_d\sigma$, as an approximation to the initial stress under the assumption that the dynamic overshoot or undershoot is negligible under slip-weakening friction. The settings of $\mu_d$ and $\sigma$ will be described in Section 5.2. To avoid large slip below the seismogenic depth, which is delineated by the termination depth of background seismicity (see Figure 1 of Yue et al. (2017)), we removed a large patch of stress

drop in the northeast part of the fault (Figure 5.2 C and D) and set a small negative stress drop of $-0.1\sigma$ below seismogenic depth.

Motivated by our earthquake cycle simulation results, we add small circular patches at the bottom of the rupture with different frictional properties and pre-stress conditions than in the rest of the seismogenic zone. The size of these asperities is set according to the idea that, if they break in isolation, they should generate earthquakes whose seismic moments $M$ follow the Gutenberg-Richter distribution (Gutenberg and Richter, 1944; Kagan, 2010a):

$$f(M) = \beta M_t^{\beta} M^{-1-\beta}, M > M_t \tag{5.4}$$

where $f(M)$ is the probability density function and $M_t$ is the cut off moment value to guarantee a finite integral of $f(M)$. The exponent $\beta$ can take values between 0.5 and 0.66. Following Kagan (2010b) we take $\beta = 0.5$. For a circular rupture with radius $R$ and moment-independent stress drop $\Delta\tau$, the moment magnitude is proportional to $R^3$. For a collection of such circular ruptures to be consistent with the Gutenberg-Richter law, the probability density distribution of $R$ must be proportional to $R^{-1-3\beta}$. We stochastically generate circular asperities with sizes sampled from a $R^{-5/2}$ distribution ($\beta = 1/2$). This approach makes strong assumptions for the sake of simplicity. It does not account for the fact that asperities can generate repeating earthquakes, whose recurrence time depends on their size, and that clusters of asperities can break together sometimes. A more detailed model accounting for these effects is beyond the scope of this study, as it would not affect the conclusions of this work. Instead of applying pre-defined along strike heterogeneities on material properties, Michel et al. (2017) demonstrates that heterogeneous stress can be spontaneously generated by running an earthquake cycle simulation with a homogeneous velocity weakening region surrounded by velocity strengthening regions, which can be an alternative way of generating short wavelength pre-stress features.

The stresses inside and around asperities are set as follows. For seismic asperities, we use a simplified representation of the residual stresses left by a circular rupture (Dieterich, 1994):

$$\tau(r) = \begin{cases} \Delta\tau((1 - \frac{R^3}{r^3})^{-\frac{1}{2}} - 1) & \text{if } r > R \\ -\Delta\tau & \text{if } r \leq R \end{cases} \tag{5.5}$$

For aseismic asperities, we set uniformly higher or lower stresses than in the ambient seismogenic zone.

We run one model with heterogeneous patches and one without, hereafter referred to as "rough model" and "smooth model", respectively.

### Friction law and related parameters

We use a linear slip-weakening friction law (Palmer and Rice, 1973; Andrews, 1976) with homogeneous static and dynamic friction coefficients, $\mu_s$ and $\mu_d$, respectively. We first set $\sigma = 120$ MPa and $\mu_d = 0.3$. The combination of static friction coefficient $\mu_s$ and critical distance $D_c$ affect the rise time and rupture speed. Decreasing $\mu_d$ or $D_c$ will shorten the rise time since both will decrease fracture energy. We set $D_c = 0.4$ m and $\mu_s = 0.45$ homogeneously in the up-dip portion by trial and error to fit the observation that the rupture has a rise time of around 5 seconds (Galetzka et al., 2015). In the down-dip portion of the rupture area, we decrease $D_c$ by a random portion within each heterogeneous stress patch. The purpose of setting heterogeneous $Dc$ here is not to be consistent with the earthquake cycle model but to create heterogeneous fracture energy which further boost high frequency radiations. We also raise $\mu_s$ to a higher value and/or decrease $\mu_d$ to a lower value in the down-dip portion as needed to guarantee that the pre-stress is between the static and dynamic strengths, $|\mu_s\sigma| > \tau_0 > |\mu_d\sigma|$.

## 5.3 Simulation results

### Sensitivity to model parameters

We determine the best fitting values of the friction parameters $\mu_s$ and $D_c$ by trial and error in order to fit key features of the ground motion recorded at the strong motion station KTP. This record is composed of a major pulse and several later arrivals. Due to its location close to the upper end of the rupture area, the major pulse is sensitive to the smooth rupture on the shallower portion of the rupture but not to the heterogeneities in the deeper portion. We thus use only the smooth models to test the sensitivity of the major pulse to $\mu_s$ and $D_c$.

We show the sensitivity of the vertical velocity record at KTP to the two parameters by perturbing around the best fitting parameter combination, $\mu_s = 0.45$ and $D_c = 0.4$ m. Increasing $\mu_s$ and $D_c$ leads to later arrival time and wider pulse width, which is expected since both operations lead to increasing fracture energy. We give more importance to matching the pulse width rather than the arrival time since the latter can be affected by velocity structure errors. We did not perturb $\mu_s$ towards smaller values than the best fitting value 0.45 since doing so leads to supershear rupture.

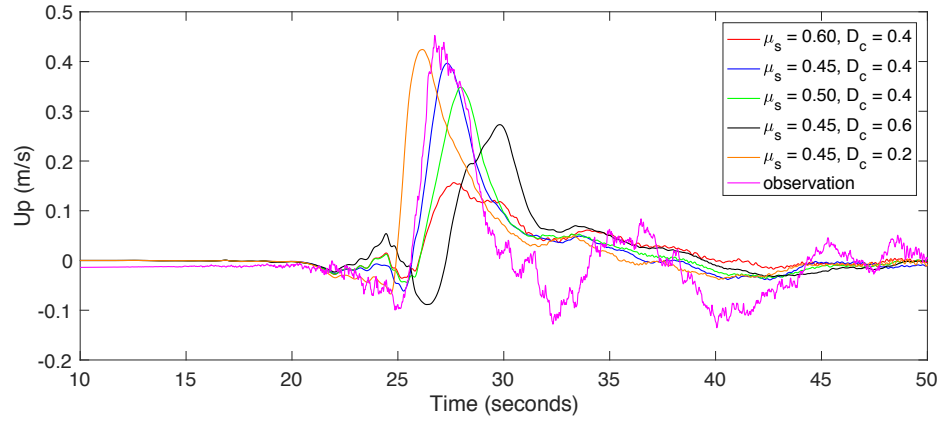


Figure 5.3: Plot of the simulations and data of vertical velocity at the strong motion station KTP. The simulations are those of the smooth models with different combinations of $(\mu_s, D_c)$. The blue line plots the preferred model that will be used to develop the rough model since its pulse width and timing make a best fit to the data (magenta line).

When $D_c$ is reduced to 0.2 m the pulse width does not decrease further nor does the rupture time (Figure 5.3). For the sake of resolvability, we choose a larger $D_c$ value so that the process zone size is sufficiently larger than the mesh size. We note that we did not search across the whole parameter space; other combinations of $D_c$ and $\mu_s$ may fit the observations equally well due to the strong trade off between the two parameters.

**Depth dependent rupture properties**

In general, both the smooth model and rough model achieve a first order fit to the kinematic model in terms of final slip and rupture time. The results of the rough model are presented in Figure 5.4 A and B. The rough model features depth dependent rupture properties. The up-dip portion has smoothly varying rupture speed while the down dip portion has rapidly changing rupture speed ranging from near zero to super-shear speed (Figure 5.4 C). As the rupture front hits the down-dip asperities, it either suddenly accelerates or decelerates depending on whether it is a stress high or stress low. According to Madariaga (1977) and Madariaga et al. (2006), a sudden change in rupture speed results in strong high frequency radiations.

To better demonstrate the depth dependent rupture properties, we record the slip rate functions $f(t)$ on the fault plane and compute their power both in a low frequency band (0.05-0.2 Hz) and a high frequency band (0.5-2 Hz). The spatial distribution of low frequency power exhibits large scale variations only, while the high frequency

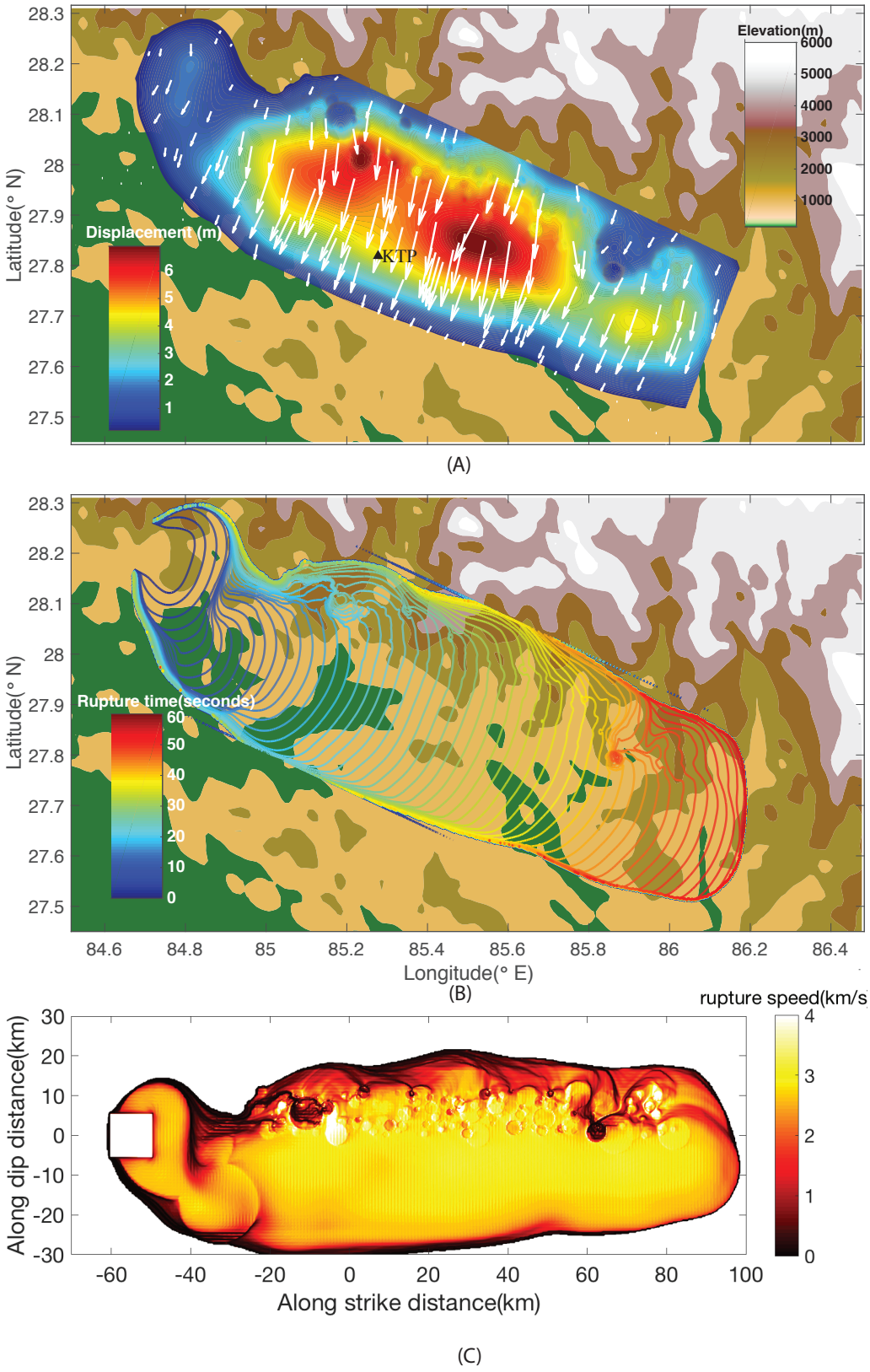


Figure 5.4: Rupture time(A), rupture speed(B) and final slip distribution(C) of the dynamic rupture simulation.

radiation has similar large scale patterns at the up-dip portion and scattered small patches at the down-dip portion. The latter contribute significantly to far field high frequency radiation (Figure 5.5). As will be shown later, the high frequency radiations at the up-dip portion of the rupture is not very well resolved by back projection due to destructive interference.

**Strong motion records at station KTP**

The city of Kathmandu was instrumented with several strong motion stations at the time of the earthquake. While most stations are positioned inside the alluvial deposits, whose records are contaminated by a 5 s basin resonance, there is one rock site station (KTP) whose record captures more clearly the source effects (Rajaure et al., 2017). We thus compare the KTP recording and the synthetics generated at this site by our smooth and rough models. To emphasize the low frequency part of the signal, we integrate the data from acceleration to velocity when making comparisons in time domain. Both models generate a characteristic velocity pulse with a duration of 5 seconds which fits the observation (Figure 5.6). The offset in timing is caused mainly by two factors: 1) our dynamic models have spatially uniform settings of $\mu_s$ and $D_c$ in the up dip portion which leads to relatively uniform rupture speed there, and 2) the velocity model may not be accurate enough. The rough model generates more energy than the smooth model in the frequency band above 1 Hz. In particular, the rough model has multiple wiggles arriving after the main pulse while the smooth model does not. That means small asperities as our model presents are needed to increase the high frequency radiation of the source.

The spectral peak around 0.2 Hz is of great interest (Rupakhety et al., 2017; Galetzka et al., 2015) since it corresponds to a characteristic period of both the source (its rise time) and the basin resonance effect, which cannot be easily separated. We find that our simulation with a 1D velocity structure generates an amplitude of the vertical component comparable with observations but underpredicts the amplitude of the horizontal components (Figure 5.6). A plausible explanation is that the KTP record has a hint of basin effect which amplifies 0.2 Hz frequency waves especially in the horizontal direction. It is shown in Takai et al. (2016) that basin effect involves much stronger amplification in horizontal directions than vertical direction.

**Moment rate function**

The tele-seismic radiation of our models is analyzed here by inspection of their moment rate functions (Figure 5.7-A). We compare their spectra to the moment

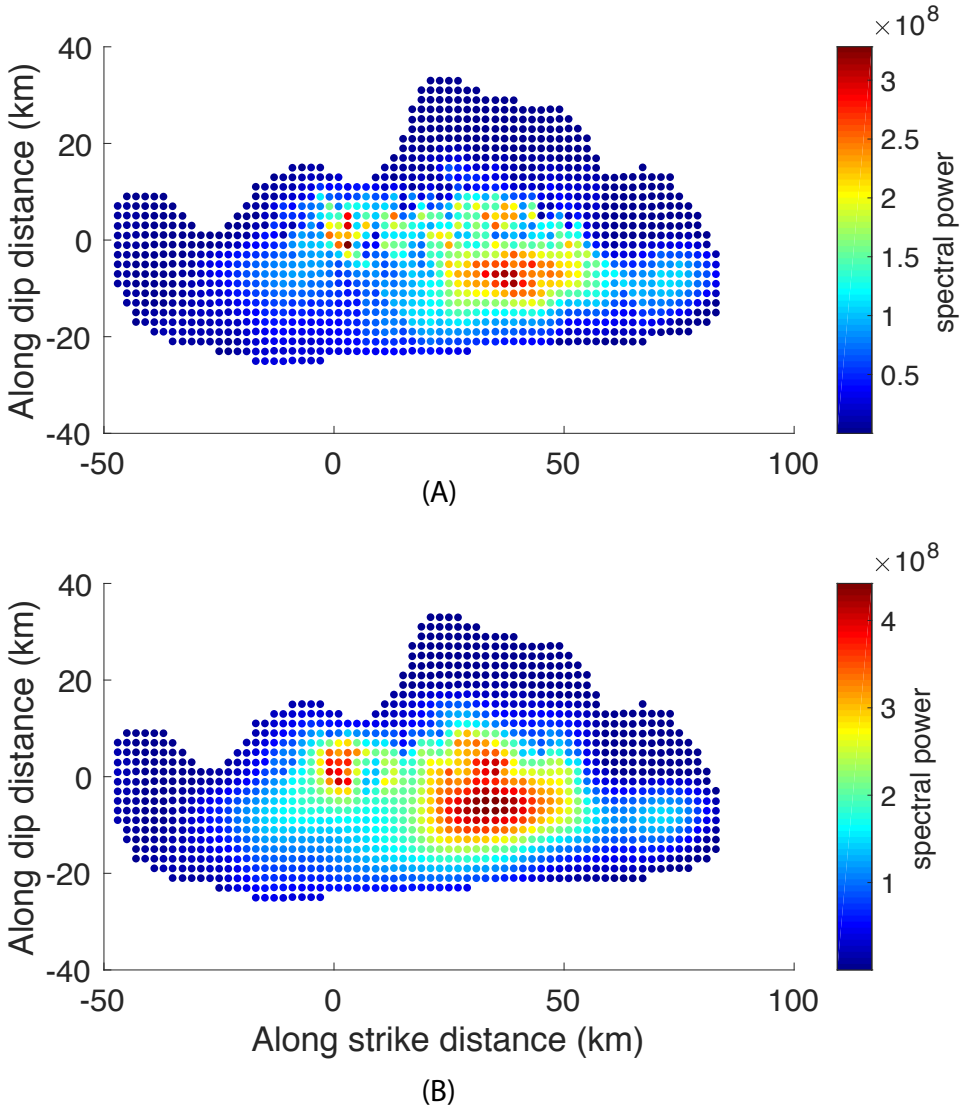


Figure 5.5: . High frequency contents 0.5-2 Hz Low frequency contents 0.05-0.2 Hz

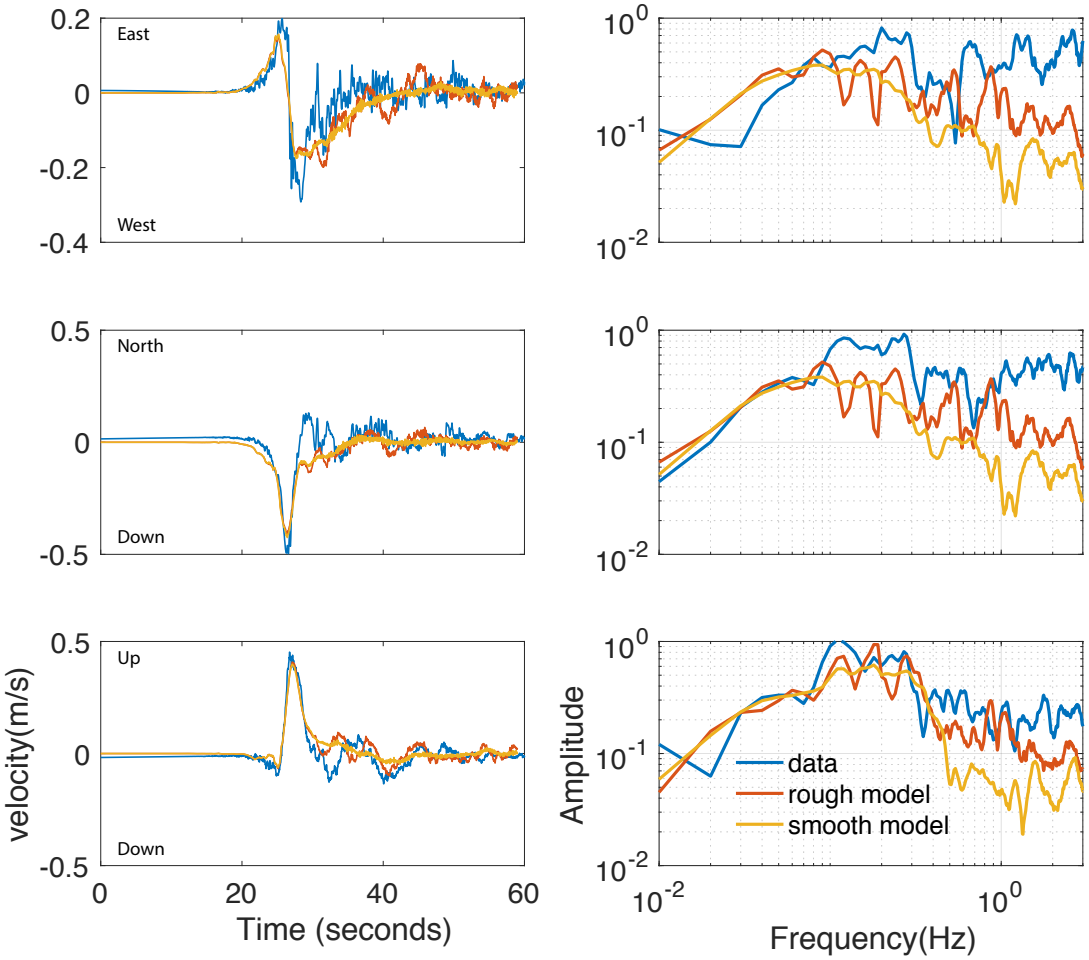


Figure 5.6: A and B. Comparison of data, kinematic model synthetics and dynamic model synthetics in time dimain(A) and spectral domain(B). KTP. Vertical (C) (D) North - South (E) (F) East - West

rate spectrum inferred by Lay et al. (2017) from a combination of finite source inversion at low frequencies and tele-seismic P-wave spectra at high frequencies after compensating for attenuation effects (Figure 5.7-B).

Our rough model has stronger high frequency content in its moment rate function than the smooth model (Figure 5.7). The smooth model does not produce enough tele-seismic high frequency radiation between 0.1 and 3 Hz. The rough model produces a moment rate spectrum much closer to the one inferred by Lay et al. (2017). Some deficiency in high frequency remains, but it is comparable to the uncertainty due to the approximate account by Lay et al. (2017) of the effect of surface reflected phases pP and sP, which can bias high the inference of source spectra, especially at high frequencies, as shown by Boatwright and Choy (1992).

### High rate GPS

There are 5 high rate GPS stations whose sampling rate can be as high as 5Hz (Galetzka et al., 2015). With epicenter distances smaller than 200 km, their velocity records can be simulated by our dynamic model, which are shown in Figure 5.8. Due to the basin resonance at a period of 5 seconds, we filtered the data and synthetics to a frequency band of 0.02 Hz - 0.1 Hz. The addition of down-dip heterogeneities does not change the low frequency synthetics at these high rate GPS stations. This indicates that the low frequency content of the data is not sensitive to small scale heterogeneities at the down-dip portion of the rupture.

## 5.4 Discussion

### Source spectrum

The source spectrum of an elongated pulse-like rupture (a Haskell source model) with rise time $T_{rise}$ shorter than its rupture duration $T_{rup}$, is flat at low frequencies ($\omega < 2/T_{rup}$), decays as $\omega^{-1}$ at intermediate frequencies ($2/T_{rup} < \omega < 2/T_{rise}$) and as $\omega^{-2}$ at high frequencies ($\omega > 2/T_{rise}$). We fit a power-law spectral decay $\omega^{-n}$ to the moment rate spectra shown in Figure 5.7-B in the frequency band $2/T_{rup} < \omega < 2/T_{rise}$. We obtain $n = 1.38$ for the observationally inferred spectrum, $n = 1.84$ for the smooth dynamic model and $n = 1.58$ for the rough dynamic model. The deviation of the decay behavior from the Haskell spectrum model ($n = 1$) is due to the heterogeneity of the source along strike, which is in contrast to the uniform slip, rise time and rupture speed assumed in the Haskell model. The rough model can be seen as composed of several large asperities in the up-dip part of the rupture and many small asperities in its down-dip part. Lay et al. (2017) showed that adding

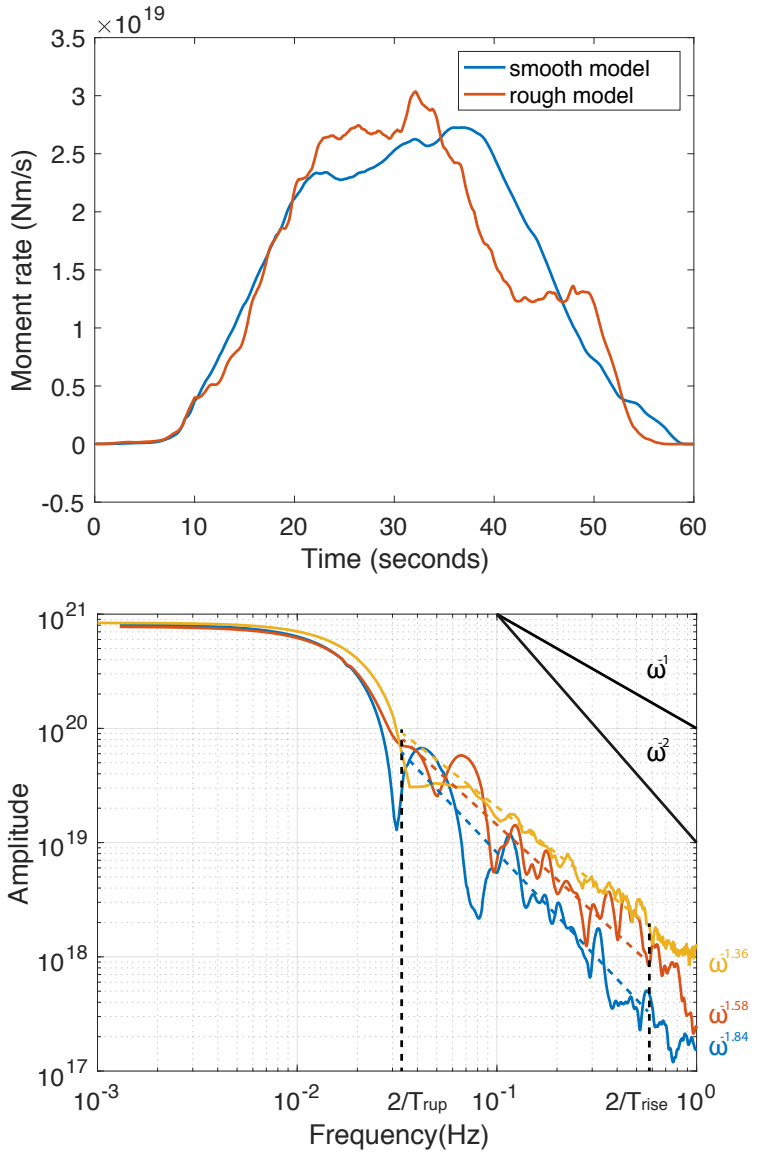


Figure 5.7: A. Moment rate functions generated by our smooth model (blue) and rough model (red). B. Moment rate spectrum generated from the smooth model (blue) and the rough model (red), and inferred from tele-seismic data by Lay et al. (2017) (yellow).

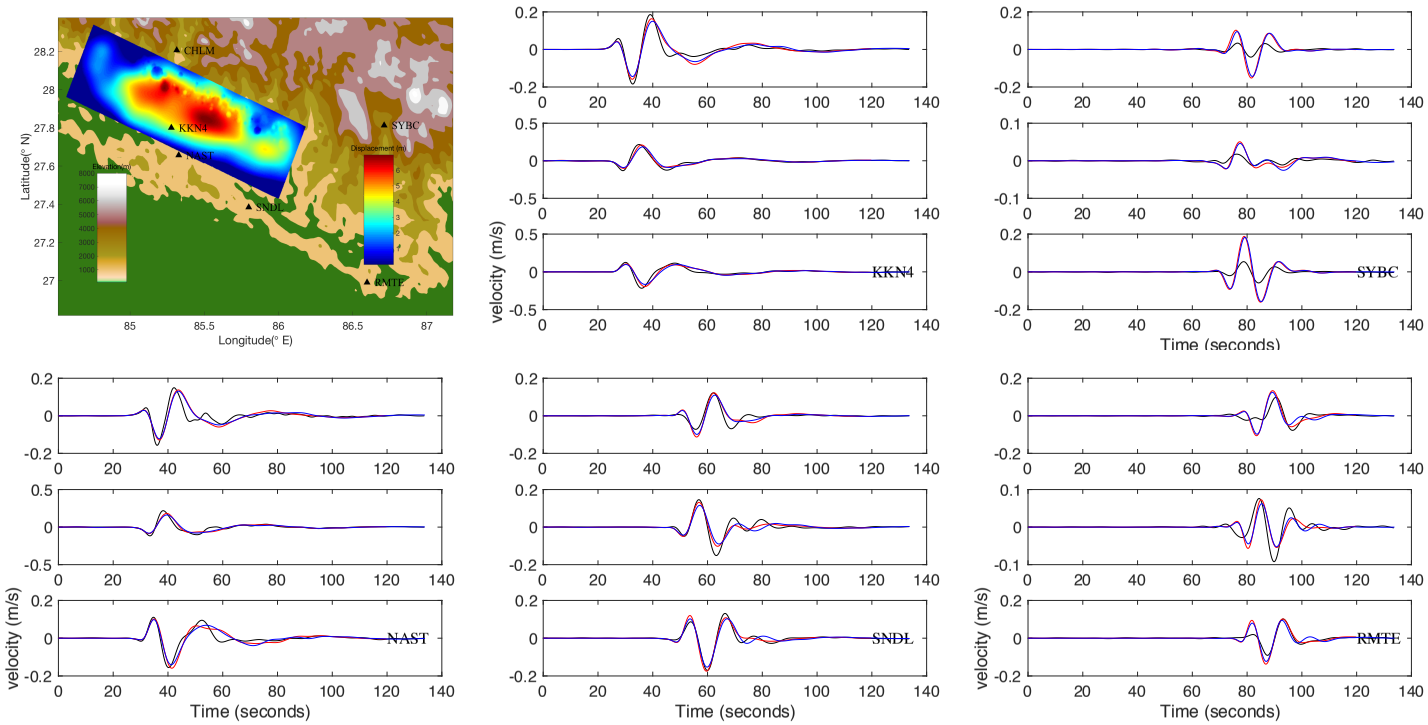


Figure 5.8: Comparison of three component high rate GPS data (black) and synthetics generated by smooth model (red) and rough model (blue). All the time series are filtered to a frequency band of 0.02 Hz - 0.1 Hz to get rid of the basin resonance effect. Data source : Galetzka et al. (2015).

up multiple Gaussian shaped moment rate functions reproduces to the first order the overall spectrum of the event. Our smooth dynamic model with only large asperities in the up-dip part produces a spectrum decay close to $\omega^{-2}$. In the rough model, the small asperities in the down-dip part postpone the onset of $\omega^{-2}$ decay to higher frequencies.

**Near-field high-frequency radiation and damage**

There is an abundance of low-storey buildings in Nepal whose resonance frequency is well above 1 Hz. Instruments that have resolution at high frequencies are only installed near Kathmandu city, which covers a very small area of the rupture, near its up-dip part, and of the damaged area. No recordings are available in the regions right above the down-dip portion of the rupture where strong high frequency radiations are expected to be generated. The peak ground velocity (PGV) distribution calculated by a previous study (Koketsu et al., 2016) using a kinematic source model was limited to frequencies up to 0.4 Hz.

We show the PGV generated by our rough model in both a broad band (0-3 Hz) and a high frequency band (1-3 Hz) in Figure 5.9. Compared with the broadband PGV (Figure 5.9A), the high-frequency PGV (Figure 5.9B) is stronger in the northern part closer to the down-dip asperities. The region with large high-frequency PGV spans the two counties with the highest fatality rate (above 1%) as calculated by Koketsu et al. (2016), but does not include the city of Kathmandu.

**Comparison of near-field and far-field ground motion**

We compare ground velocities produced by our model at different distances from the source in Figure 5.10. Due to the limitation of the finite simulation domain, the largest distance considered is about one fault length away from the source. We find that the spectra at frequencies above 0.3 Hz are very similar and follow a $\omega^{-1.38}$ asymptotic decay. At low frequencies the near-field spectra are flat whereas the more distant spectra increase with frequency. These spectral properties are consistent with a transition from near-field ground velocity roughly proportional to the slip rate in the rupture area closest to the station, to far-field ground velocity proportional to seismic moment acceleration.

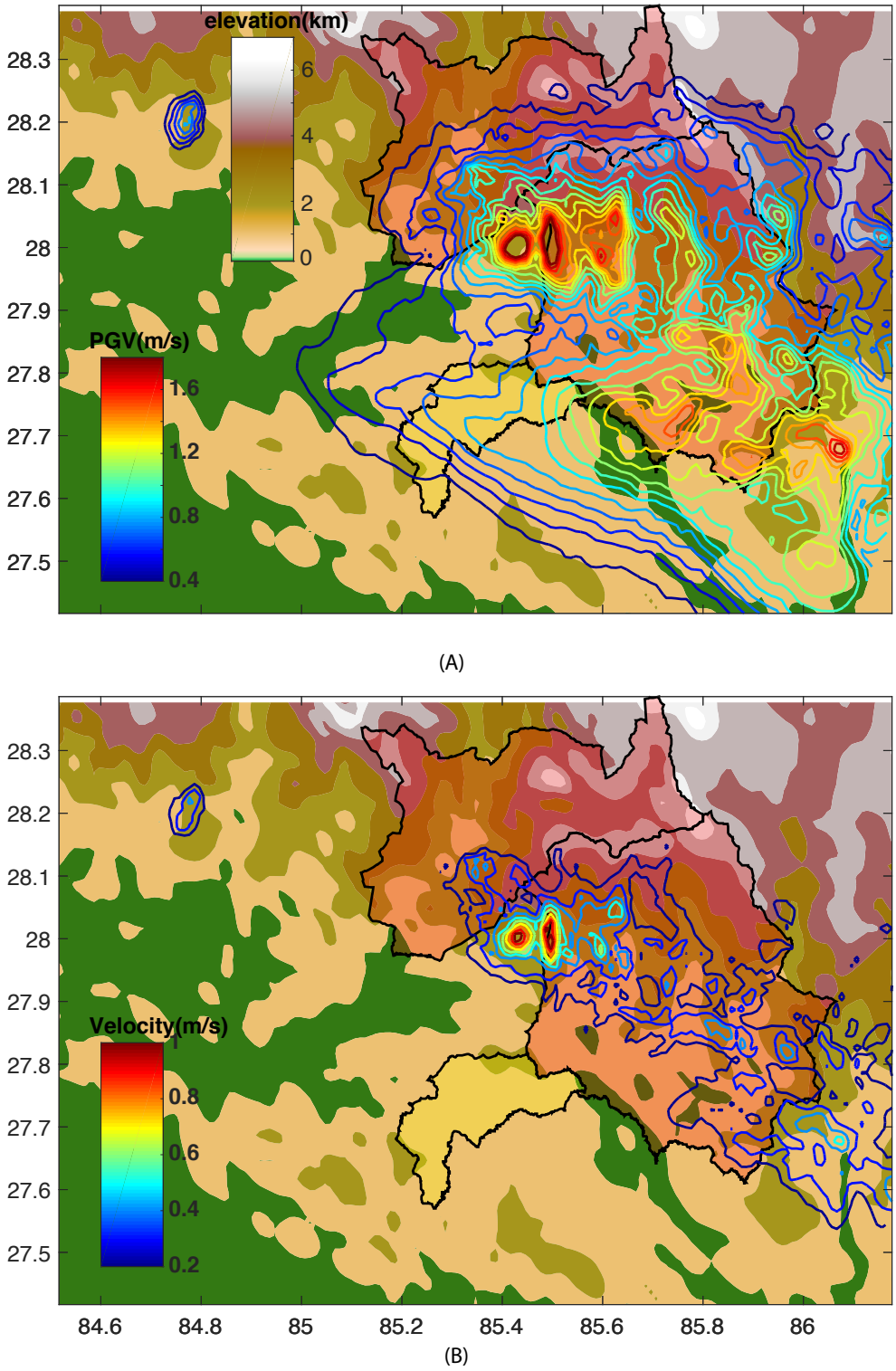


Figure 5.9: A: Distribution of broadband (0-3 Hz) peak ground velocity from our rough dynamic source model. B: High-frequency peak ground velocity (1-3 Hz). The red shaded regions are the only two districts with a fatality rate above 1%. The yellow shaded region is the Kathmandu city region.

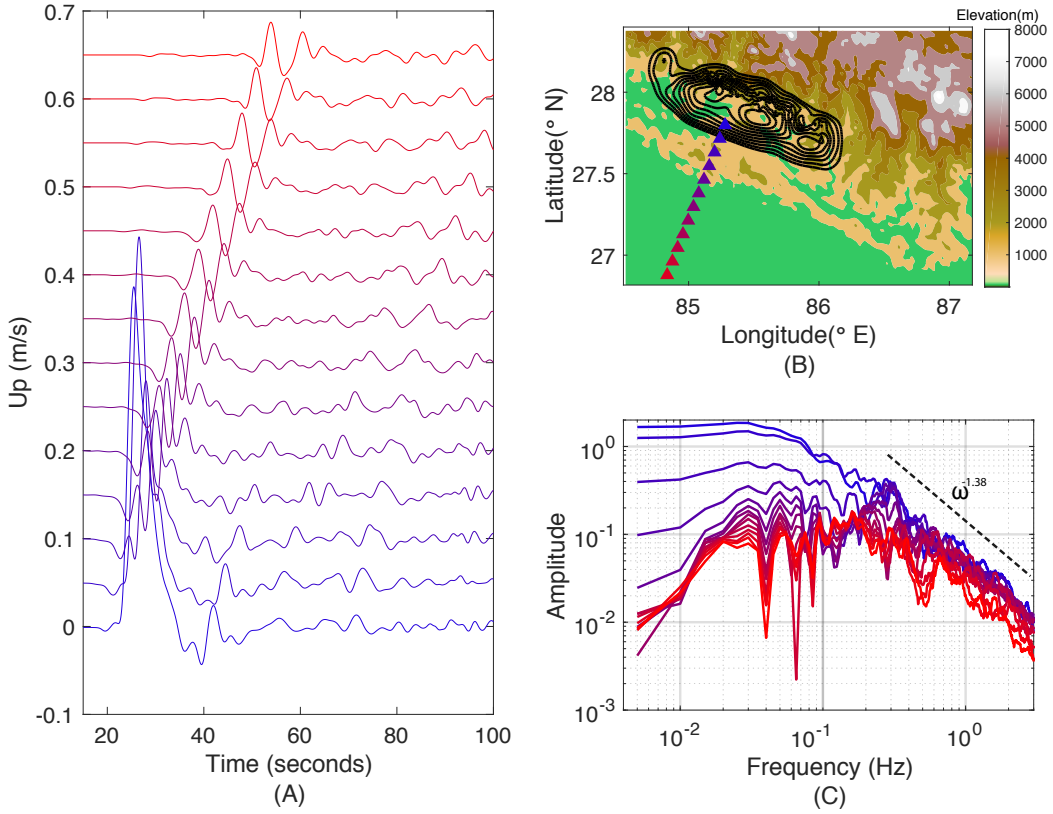


Figure 5.10: Vertical ground velocity time series (A) and spectra (C) produced by the rough dynamic source model at sites located at different distances from the rupture as indicated by blue triangles in the map (B). Curve colors indicate their site-source distance: from blue at near-source distances to red at farther distances.

**High-frequency radiation in the up-dip portion is not visible by teleseismic back-projection**

Destructive interference causes the high-frequency radiation from the up-dip portion of the rupture to be unseen by teleseismic back-projection. Back-projection with beam forming is an array processing technique by stacking closely spaced seismic records shifted by a travel time from a trial source. If the trial source location coincides with the true source location, the stacked signal is much stronger than if the trial and true sources are not coincident. One basic assumption of the beam forming method is that the records stack constructively only if the trial and true source locations coincide (Fukahata et al., 2013; Ishii et al., 2005).

The impulse response of the beam forming processing (also known as the array response function) is peaked at the true source location and has several secondary

maxima elsewhere. The width of the main lobe of the impulse response can be of several wavelengths. A smooth line source, which resembles the smooth rupture processes at the up-dip portion of the rupture, results in a superposition of multiple such impulse response functions with different phase shifts. This causes destructive interference which annihilates most of the beam forming energy throughout the rupture, leaving only two peaks at the beginning and end of the rupture (Figure B.2).

To demonstrate this destructive interference effect on the imaging of the Gorkha earthquake source specifically, we design numerical experiments that back project the seismic wave generated by our dynamic source models at two typical frequencies used by previous studies (Avouac et al., 2015; Yagi and Okuwaki, 2015; Grandin et al., 2015): a low-frequency component of 0.25 Hz and a high-frequency component of 2 Hz. In a real implementation of back-projection, researchers usually divide a frequency band into small narrow bands, and integrate the power generated at each band. The two typical frequencies we chose can represent the frequencies around them. We assume an idealized situation in which the receivers are uniformly positioned globally, with high spatial density and high coherency at all inter-station distances. The finite source is represented by multiple point sources whose rupture time is taken from the rough dynamic model. We simulate seismograms produced by the finite source at all stations and then back-project them on the fault. The forward and backward propagator is a time shift operator with the time shift calculated using the 1D PREM model. We neglect the amplitude decay so that each receiver contribute to the beam-forming energy with the same weight. As shown in Figure 5.11 B and D, the low-frequency back-projection image has energy patches covering the whole seismogenic depth while the high-frequency image has that concentrated at the deeper portion of the seismogenic zone. This can be explained by the analysis in appendix A that back-projection energy is concentrated where there are rapid changes of rupture speed or slip amplitude (Figure B.2).

## 5.5 Conclusion

Our dynamic rupture simulations utilize deterministic long wavelength initial stress from kinematic inversion results and stochastic short wavelength asperities at the down-dip portion of the rupture inspired by earthquake cycle simulations and earthquake observations. This novel approach, with simple dynamic parameter settings, reproduces the frequency dependent rupture process, in particular the concentration of high-frequency radiation in the down-dip part of the rupture. The addition of deep asperities produces stronger high-frequency content both in the strong mo-

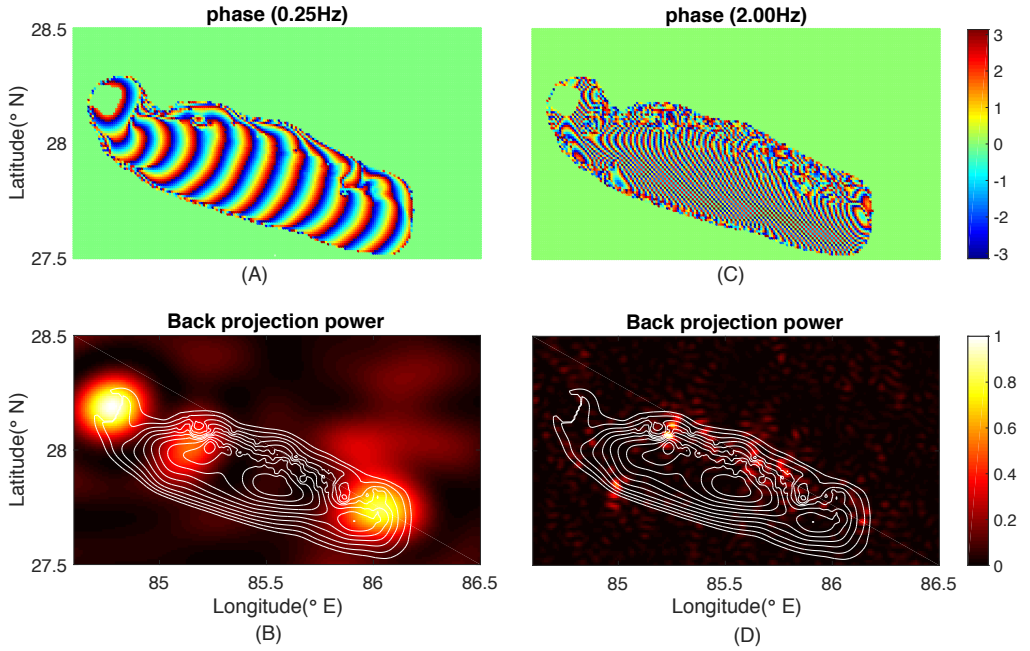


Figure 5.11: Back projection demonstration of single frequency source (A: 0.25 Hz, B: 2 Hz) model generated using amplitude and phase information from the dynamic model. Due to interference of the finite source, constructive interference at 2 Hz only occurs at the down-dip part where source amplitude and rupture speed vary rapidly.

tion at station KTP and in the moment rate, which improves the agreement with observations.

We do a back projection test using our dynamic rupture model in two frequency bands. The 0.25 Hz back-projection image shows energy all across the seismogenic depth while the 2.0 Hz back-projection has energy focused on the down-dip portion of the rupture. These modeling results agree with previous back projection results.

We also model the strong motion distribution in the near source region. The region right above the northern part of the rupture experiences higher peak ground velocity than the southern part. This agrees with the fact that two counties in the northern part have the highest fatality rate.

*Chapter 6*

# SOME ADVANCES ON THE SPECTRAL ELEMENT EARTHQUAKE CYCLE SIMULATOR

## 6.1 Introduction

Simulation of long term fault slip interspersed by seismic events is of great importance for understanding earthquake physics and long term forecasting. A canonical approach of treating the problem as an elastodynamic problem coupled with nonlinear frictional boundary conditions have been established during decades of studies (Shibazaki and Matsu'ura, 1992; Cochard and Madariaga, 1996; Rundle et al., 1999; Kato, 2004; Liu and Rice, 2005; Hillers et al., 2006; Dieterich and Richards-Dinger, 2010). This so called earthquake cycle simulation is a multiscale problem because the fault slip velocity ranges from several milimeters per year which represent the plate moving rate to several meters per second which represent the slip rate during an earthquake. As a result, the simulation time step will have to be dynamically adjusted so as to be computationally affordable. Solving the elastodynamic equations of motion with inertia term using explicit time marching scheme is the most efficient from a per time step perspective. However, that requires the Courant stability condition (Courant et al., 1986) to be satisfied so that the maximum allow time step size is on the order of grid size divided by wave speed which makes the simulation during interseismic period intractable. To tackle this issue, one approach is to replace the inertia term with a radiation damping term (Rice, 1993; Cochard and Madariaga, 1994) such that the equations of motion is converted to equations of equilibrium during interseismic period. This requires a switch that change the simulation from a quasi-static one to a dynamic one which is usually judged by maximum slip rate on the fault (Lapusta and Liu, 2009). So another approach is to use an implicit scheme to solve the equation of motion (Pipping et al., 2016). Boundary integral methods has been successfully implemented to solve this elastic boundary value problem because of its computational efficiency. However, this approach requires that the elastic response (Green's function) between any two points on the fault plane to be available. This usually requires that the material properties inside the bulk to be homogeneous.

With the fast deployment of high performance computing resources and the de-

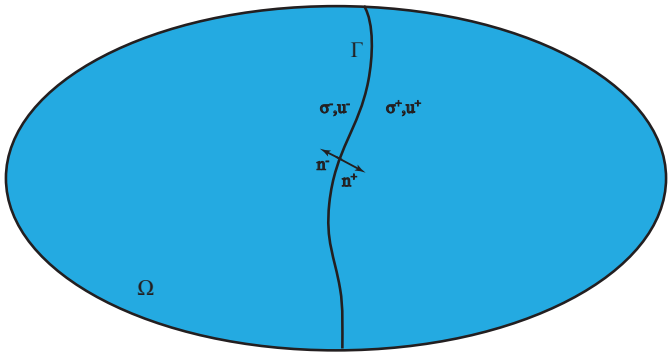


Figure 6.1: Sketch of the elastodynamic boundary value problem. The elastic body is denoted as $\Omega$ while the fault plane is denoted as $\Gamma$. The quantities displacement $u$ and stress tensor $\Sigma$ can be discontinuous across the fault plane.

velopment of sophisticated numerical methods, solving large scale elastodynamic problem with complicated material properties becomes possible. The spectral element method has been successfully applied to solving large scale elastodynamic problems due to the pioneering work of Komatitsch and Vilotte (1998). (Kaneko et al., 2008; Galvez et al., 2014) introduced the dynamic fault solver into the code enabling it to model co-seismic slip during earthquakes. Kaneko et al. (2011) developed a 2D quasi-static solver coupled with the spectral element solver to solve for long term fault evolution. However, their method assumes symmetric material properties across the fault so that the particle velocity on two sides of the fault can be computed by simply divide the slip rate by 2. Also, the normal stress on the fault remain unchanged due to symmetry. These assumptions substantially limit its usage. Here, we develop a new method that removes the symmetry assumption which makes it able to solve generalized long term fault evolution problem with complicated geometry.

## 6.2 The elasto-dynamic problem with boundary conditions

Earthquake cycle simulation involves solving a elastodynamic problem in an elastic body $\Omega$ (see Figure 6.1)

$$\partial_j \Sigma_{ij} + f_i = \rho \ddot{u}_i \tag{6.1}$$

$$\Sigma_{ij} = \frac{1}{2} c_{ijkl} (\partial_k u_l + \partial_l u_k) \tag{6.2}$$

$$\forall u, \Sigma \in int(\Omega)$$

coupled with the following boundary conditions on the fault plane $\Gamma$:

$$T^+ = \Sigma^+ \cdot n^+ = -\Sigma^- \cdot n^- = T^- \tag{6.3}$$

$$u^+ \cdot n^+ = -u^- \cdot n^- \tag{6.4}$$
$$\forall u^{+/-}, \Sigma^{+/-}, T^{+/-} \in \Gamma$$

(6.3) means that the traction on the two sides of the fault plane must be opposite and (6.4) means the normal displacement must be continuous across the fault plane. Additionally, another boundary constraint will be provided by friction law, we here present the general form of the famous rate-and-state friction law:

$$\dot{\delta} = \dot{u}^+ - \dot{u}^- \tag{6.5}$$

$$f(T^+, \dot{\delta}, \theta) = 0 \tag{6.6}$$

$$\dot{\theta} = g(|\dot{\delta}|, \theta) \tag{6.7}$$
$$\forall \dot{\delta}, T^+, \theta \in \Gamma$$

Where $\dot{\delta}$ denotes the slip velocity and $\theta$ denotes the state variable through which the boundary traction $T^+$ depends not only on the current $\dot{\delta}$ but the whole history of $\dot{\delta}$. The functional form of $f$ in (6.6) is as such: we decompose $T^+$ into:

$$\sigma = T^+ \cdot n^+ \tag{6.8}$$

$$\tau = T^+ - \sigma n^+ \tag{6.9}$$

where $\sigma$ and $\tau$ denotes normal traction and shear traction. With the addition of the background stress $(\sigma_0, \tau_0)$, the total stress must satisfy:

$$|\tau + \tau_0| - |\sigma + \sigma_0|(\mu_0 + a\log(\frac{|\dot{\delta}|}{\dot{\delta}_0}) + b\log(\frac{\dot{\delta}_0\theta}{L_c})) = 0 \tag{6.10}$$

Where $f_0$ , $\dot{\delta}_0$ are reference frictional coefficient and reference slip rate.

This problem (1) – (10) is solvable with numerical methods such as finite difference method, finite element methods and spectral element method. However, the elastic wave propagation problem as formulated by (6.1) and (6.2) require a very refined time discretization as governed by the Courant stability condition, which posits that the time step $\Delta t$ have to be smaller than the spatial discretization size $\Delta h$ divided by wave speed $V_p$. Usually , this will result in a time step of a fraction of a second where we would like to model several earthquake cycles that span tens of years .

### 6.3 Quasi-static approximation

Because of the harsh stability condition of the original problem, we reformulate the problem by omitting the inertia term on the right hand side of equation 6.1 such that we assume that the system will reach elastic equilibrium at every time step. We further assume that the body force $f = 0$. Now equation 6.1 is replaced by

$$\partial_j \Sigma_{ij} = 0 \tag{6.11}$$

We employ the following updating scheme for solving equation (6.3)-(6.11), assuming we have $(u_n, \dot{u}_n, \dot{\delta}_n, \tau_n, \sigma_n, \theta_n)$ where the subscript $n$ means the discretized quantity at time step $n$.

(0) Define temporary variable

$$(\tilde{\dot{u}}, \tilde{\dot{\delta}}, \tilde{\theta}) = (\dot{u}_n, \dot{\delta}_n, \theta_n)$$

(1) update state variable $\theta$ using equation 6.7:

$$\theta^*_{n+1} = \theta_n + g(|\tilde{\dot{\delta}}|, \tilde{\theta})\Delta t \tag{6.12}$$

(2) Calculate boundary traction

$$\Sigma^*_{n+1,ij} = c_{ijkl}(u_n + \tilde{\dot{u}}\Delta t)_{k,l} \tag{6.13}$$

$$\sigma^*_{n+1} = (\Sigma^{*+}_{n+1} \cdot n^+) \cdot n^+ \tag{6.14}$$

$$\tau^*_{n+1} = |\Sigma^{*+}_{n+1} \cdot n^+ - \sigma \mathbf{e}_{n^+}| \tag{6.15}$$

(3) Calculate updated $\dot{\delta}^*_{n+1}$ using equation 6.10.

$$\dot{\delta}^*_{n+1} = \dot{\delta}_0 \exp\left(\frac{\frac{|\tau^*_{n+1}+\tau_0|}{|\sigma^*_{n+1}+\sigma_0|} - f_0 - b\log(\frac{\dot{\delta}_0\theta^*_{n+1}}{L_c})}{a}\right) \tag{6.16}$$

(4) Compute the following elastic equilibrium problem to get $\dot{u}^*_{n+1}$

$$\partial_j c_{ijkl}(\partial_k \dot{u}^*_{n+1,l} + \partial_l \dot{u}^*_{n+1,k}) = 0 \tag{6.17}$$

with boundary conditions:

$$n^+_j c_{ijkl}(\partial_k \dot{u}^{*,+}_{n+1,l} + \partial_l \dot{u}^{*,+}_{n+1,k}) = -n^-_j c_{ijkl}(\partial_k \dot{u}^{*,-}_{n+1,l} + \partial_l \dot{u}^{*,-}_{n+1,k}) \tag{6.18}$$

$$n_j^+ \dot{u}_{n+1,j}^{*,+} = -n_j^- \dot{u}_{n+1,j}^{*,-} \tag{6.19}$$

$$\dot{u}_{n+1,\parallel}^{*,+} - \dot{u}_{n+1,\parallel}^{*,-} = \dot{\delta}_{n+1}^{*} - V_{pl} \tag{6.20}$$

(5) update temporary variable

$$(\tilde{\dot{u}}, \tilde{\dot{\delta}}, \tilde{\theta}) = \frac{1}{2}(\dot{u}_n + \dot{u}_{n+1}^{*}, \dot{\delta}_n + \dot{\delta}_{n+1}^{*}, \theta_n + \theta_{n+1}^{*})$$

and loop through (1)-(4) again. Now we assign the value of $(\dot{u}_{n+1}^{*}, \theta_{n+1}^{*}, \dot{\delta}_{n+1}^{*})$ to the variables $(\dot{u}_{n+1}, \theta_{n+1}, \dot{\delta}_{n+1})$ to finish one time evolution step. As for the time step, we use the same method as Kaneko et al. (2011) to adapt the time step size to the maximum slip rate on the fault plane.

This method is similar in idea to the Runge-Kutta method, the difference is that in Runge-Kutta method, one uses only variables in previous time step to calculate variables at future time step. But in this problem, due to the complicated dependence relation between variables, we sometimes use the variable at the the current time step to calculate other variables at the same time step. Of all the evolution steps, step (4) is the most time consuming one which involves solving an elastic equilibrium problem with boundary conditions. We use the spectral element method to solve this elliptic partial differential equation. (equation 6.17 - 6.20)

### 6.4 Spatial discretization: The spectral element representation

The spectral element method is a special kind of finite element method with orthogonal basis functions. For simplicity, here I consider only a 2D problem. To solve step (4) in a discrete configuration, we define $\dot{u}_{n+1}^{*} = [\mathbf{U}, \mathbf{V}]$ which represent the velocity in x,z direction respectively. We further decompose

$$[\mathbf{U}, \mathbf{V}] = [\mathbf{U}_1, \mathbf{U}_2^+, \mathbf{U}_2^-, \mathbf{V}_1, \mathbf{V}_2^+, \mathbf{V}_2^-]$$

The subscript 1 means quantities in the interior of the domain and subscript 2 means quantities on the fault plane. The superscript $+/-$ means the quantities on two side of the fault plane. I write out the discrete form of the elastic equilibrium equation (i.e. equation 6.11)

$$\begin{bmatrix} & & & & & \\ & & K & & & \\ & & & & & \\ & & & & & \\ & & & & & \\ & & & & & \end{bmatrix} \begin{bmatrix} \boldsymbol{U}_1 \\ \boldsymbol{V}_1 \\ \boldsymbol{U}_2^+ \\ \boldsymbol{U}_2^- \\ \boldsymbol{V}_2^+ \\ \boldsymbol{V}_2^- \end{bmatrix} = \begin{bmatrix} \mathbf{0} \\ \mathbf{0} \\ \mathbf{B}\boldsymbol{\tau} \cdot \mathbf{n}_x^+ \\ \mathbf{B}\boldsymbol{\tau} \cdot \mathbf{n}_x^- \\ \mathbf{B}\boldsymbol{\tau} \cdot \mathbf{n}_z^+ \\ \mathbf{B}\boldsymbol{\tau} \cdot \mathbf{n}_z^- \end{bmatrix} \tag{6.21}$$

where $\boldsymbol{K}$ is the stiffness matrix, with the constraint that

$$\boldsymbol{U}_2^+ - \boldsymbol{U}_2^- = \dot{\delta}_x \tag{6.22}$$

$$\boldsymbol{V}_2^+ - \boldsymbol{V}_2^- = \dot{\delta}_z \tag{6.23}$$

and

$$\mathbf{B}\boldsymbol{\tau} \cdot \mathbf{n}_x^+ + \mathbf{B}\boldsymbol{\tau} \cdot \mathbf{n}_x^- = \mathbf{0} \tag{6.24}$$

$$\mathbf{B}\boldsymbol{\tau} \cdot \mathbf{n}_z^+ + \mathbf{B}\boldsymbol{\tau} \cdot \mathbf{n}_z^- = \mathbf{0} \tag{6.25}$$

By eliminating redundant variables in matrix representation: Define a linear transform

$$\boldsymbol{D} = \begin{bmatrix} 1 & 0 & 0 & 0 & 0 & 0 \\ 0 & 1 & 0 & 0 & 0 & 0 \\ 0 & 0 & 1 & 1 & 0 & 0 \\ 0 & 0 & 0 & 0 & 1 & 1 \end{bmatrix} \tag{6.26}$$

Then

$$\boldsymbol{D}^T \begin{bmatrix} \boldsymbol{U}_1 \\ \boldsymbol{V}_1 \\ \boldsymbol{U}_2^- \\ \boldsymbol{V}_2^- \end{bmatrix} + \begin{bmatrix} \mathbf{0} \\ \mathbf{0} \\ \dot{\delta}_x \\ \mathbf{0} \\ \dot{\delta}_z \\ \mathbf{0} \end{bmatrix} = \begin{bmatrix} \boldsymbol{U}_1 \\ \boldsymbol{V}_1 \\ \boldsymbol{U}_2^+ \\ \boldsymbol{U}_2^- \\ \boldsymbol{V}_2^+ \\ \boldsymbol{V}_2^- \end{bmatrix} \tag{6.27}$$

and

$$\boldsymbol{D} \begin{bmatrix} \mathbf{0} \\ \mathbf{0} \\ \mathbf{B}\boldsymbol{\tau} \cdot \mathbf{n}_x^+ \\ \mathbf{B}\boldsymbol{\tau} \cdot \mathbf{n}_x^- \\ \mathbf{B}\boldsymbol{\tau} \cdot \mathbf{n}_z^+ \\ \mathbf{B}\boldsymbol{\tau} \cdot \mathbf{n}_z^- \end{bmatrix} = \mathbf{0} \tag{6.28}$$

So

$$\boldsymbol{D}\boldsymbol{K}\boldsymbol{D}^T \begin{bmatrix} \boldsymbol{U}_1 \\ \boldsymbol{V}_1 \\ \boldsymbol{U}_2^- \\ \boldsymbol{V}_2^- \end{bmatrix} = -\boldsymbol{D}\boldsymbol{K} \begin{bmatrix} \mathbf{0} \\ \mathbf{0} \\ \dot{\delta}_x \\ \mathbf{0} \\ \dot{\delta}_z \\ \mathbf{0} \end{bmatrix} \tag{6.29}$$

equation 6.29 is solvable with conjugate gradient method since $\boldsymbol{D}\boldsymbol{K}\boldsymbol{D}^{\boldsymbol{T}}$ is a symmetric positive definite matrix.

| Parameter | Symbol | Value |
|---|---|---|
| P wave speed | $V_p$ | 4800m/s |
| Shear wave speed | $V_s$ | 2771m/s |
| Poisson's ratio | $v$ | 0.25 |
| Density | $\rho$ | $2670kg/m^3$ |
| Reference slip rate | $\dot{\delta}_0$ | $10^{-6}$m/s |
| Reference frictional cfficient | $f_0$ | 0.6 |
| Characteristic slip distance | $L$ | 84 $\mu$m |
| Effective background normal stress | $\sigma_0$ | 120Mpa |
| Plate moving rate | $V_{pl}$ | $6.342 \times 10^{-11}$ m/s |
| Rate and state parameter a | a | 0.0144 |
| Rate and state parameter b | b | 0.0191(0.0097)* |

Table 6.1: Parameter setting for the benchmark test.

## 6.5 Benchmark test

We modify the work of Kaneko et al. (2011) to enable simulation of a Mode II rupture hereafter referred to as Kaneko 2011. Results given by our new algorithm will be compared against that given by Kaneko 2011. The simulation domain has homogeneous material properties to facilitate the Kaneko 2011 method (Figure 6.2). The loading is applied by letting the upper and lower boundary to slip relative to each other at a constant rate $V_{pl}$. To reduce computational cost, we use an average node spacing of 0.75m. There are two theoretical estimates of critical nucleation size as given by Rice and Ruina (1983):

$$h_R^* = \frac{\pi}{4} \frac{\mu^* L}{\sigma_0 (b-a)} \tag{6.30}$$

and Rubin and Ampuero (2005):

$$h_A^* = \frac{2}{\pi} \frac{\mu^* L b}{\sigma_0 (b-a)^2} \tag{6.31}$$

. Note that for mode II crack, the effective shear modulus $\mu^* = \frac{\mu}{1-v}$ where $v$ is the Poisson's ratio. Using values in Table 6.5, the minimum $h_A^*$ value for this problem is 10.53 m which is 14 times the average node spacing and the minimum $h_R^*$ for this problem is 3.19 m which is 4.3 times the average node spacing. Considering that when $a/b > 0.5$, $h_R$ is a better estimate than $h_A$ (Rubin and Ampuero, 2005), our mesh is fine enough to resolve the physics.

The results of the benchmark test are shown in Figure 6.3 and Figure 6.4.

In Figure 6.3, there is a rupture time difference between the results given by two methods which accumulates to 0.01 year at the fourth cycle. In Figure 6.4, slip

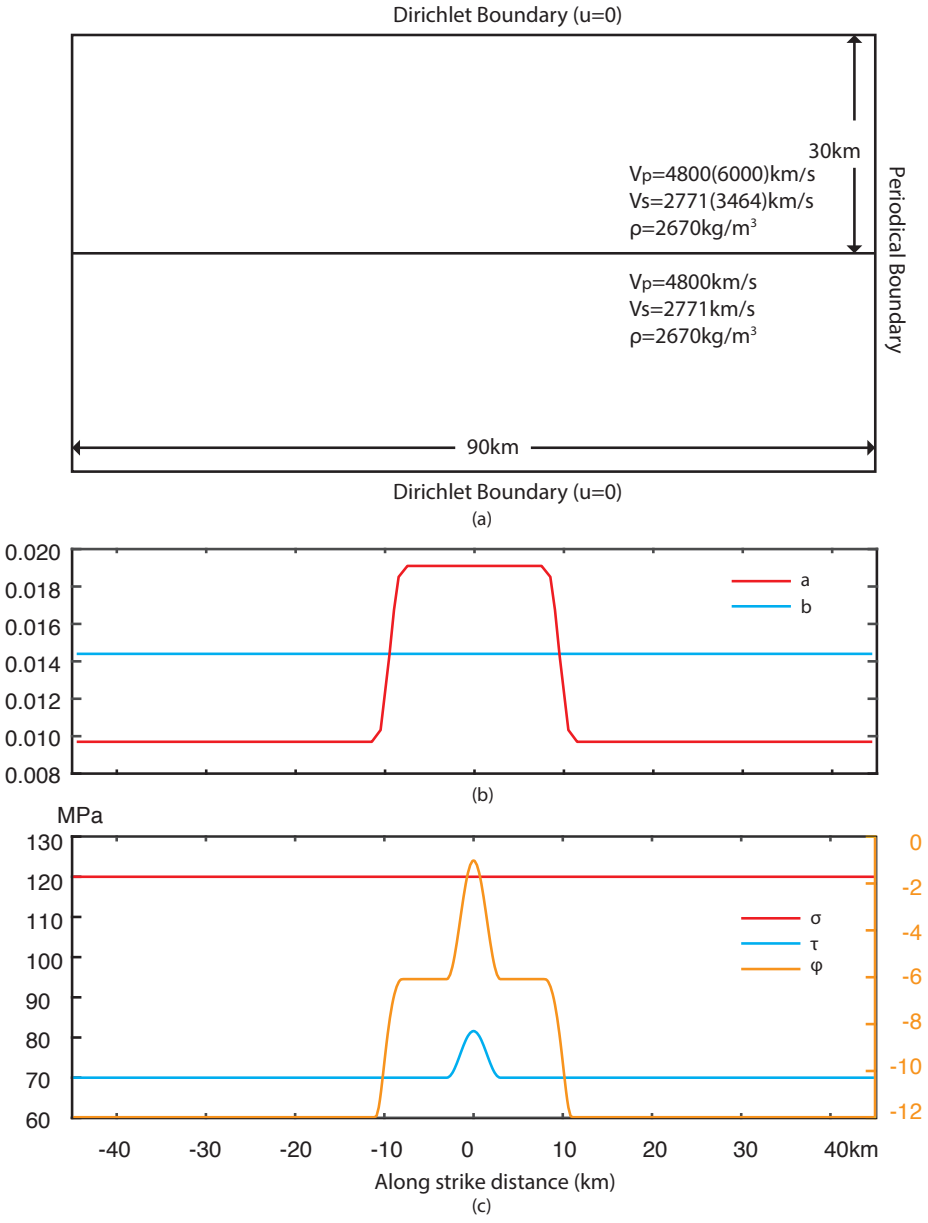


Figure 6.2: Settings of the numerical simulation.(a) Boundary conditions (b) and (c) Initial conditions. In (c), $\phi$ is defined as $\log(\dot{\delta}_0\theta/L_c)$

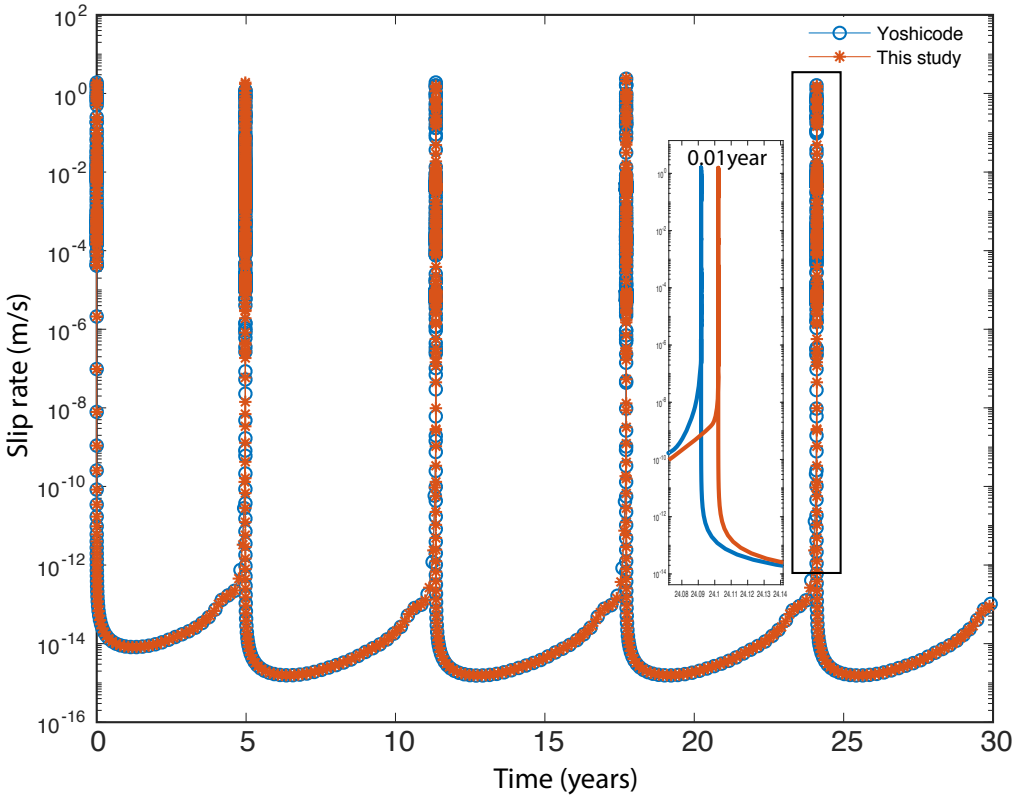


Figure 6.3: Comparison of slip rate at $x = 0$ for the two methods. After 4 seismic cycles, the two methods have a timing difference of 0.01 year.

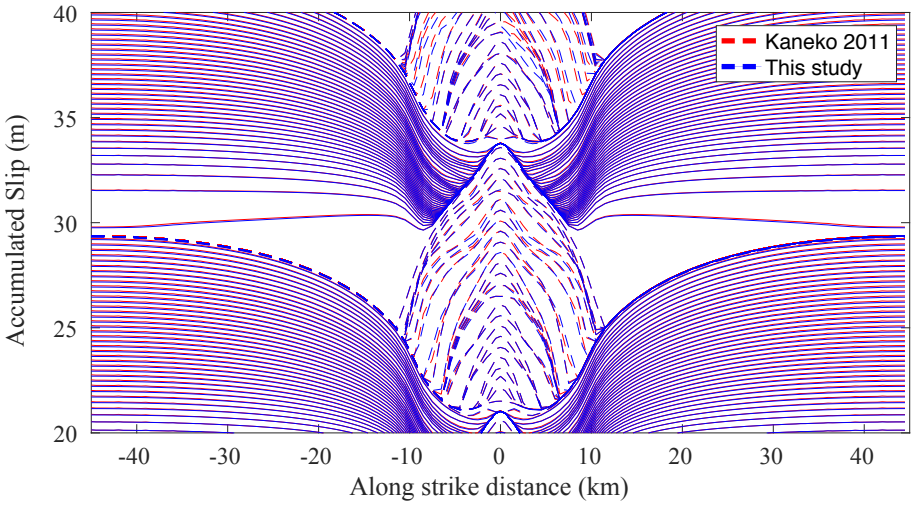


Figure 6.4: Slip comparison between the two methods. Solid lines are slip during the interseismic period which are plotted per $5 \times 10^6$ seconds. The dashed lines are slip plot during seismic events. They are plotted per 0.5 mm slip occurring at $x = 0$.

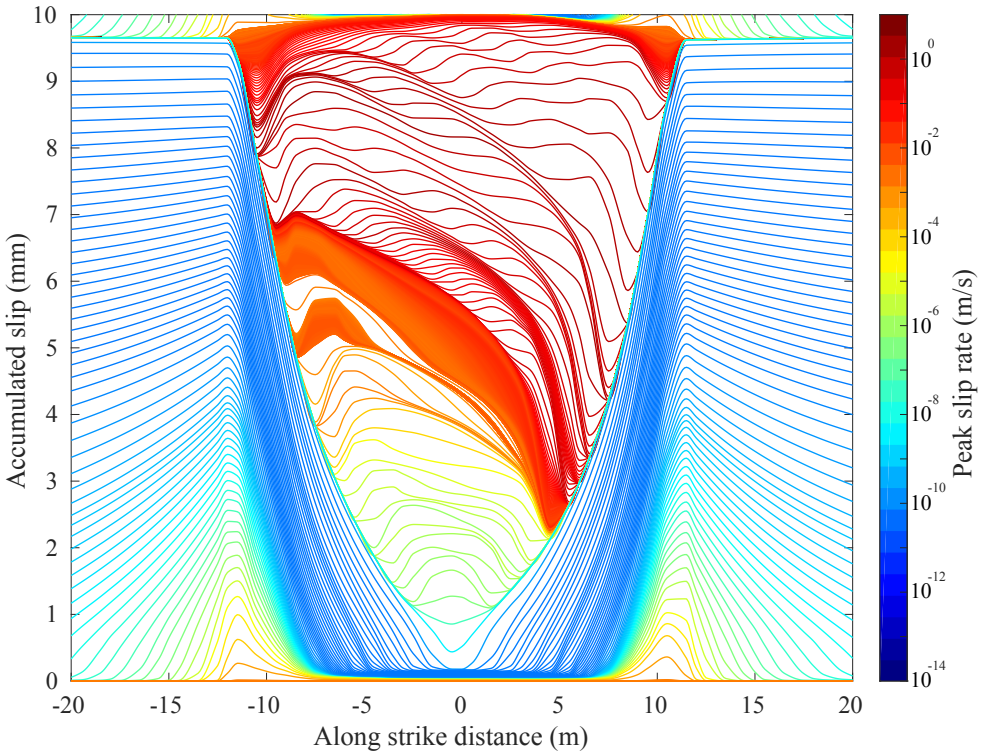


Figure 6.5: The slip profile of a bi-material fault during a full earthquake cycle. The slip is plotted every 10 time steps with the color indicating the maximum slip rate on the fault at that time step.

at the second and third cycle are plotted. There is some mismatch in the seismic event towards the end of the third cycle (between 15 and 20 years). Some plausible explanations are: 1) we apply normal stress coupling in our new method which may generate some small perturbation; 2) We apply conjugate gradient method (CG) to solve for velocity field while the Kaneko 2011 method use CG to solve for displacement field. It's difficult to set consistent CG error bounds for both methods. Given the problem is highly non-linear, small perturbation accumulation may lead to noticeable difference as time elapses. The Kaneko 2011 method has been benchmarked with the boundary integral method. So this bechmark shows that our new method can produce consistent results as the Kaneko 2011 method when the case is reduced to a symmetric one.

**Modeling earthquake cycle on a bi-material fault**

One usage of our new algorithm is to conduct earthquake cycle modeling on bi-material faults. The model setting is similar to the previous settings for the bench-

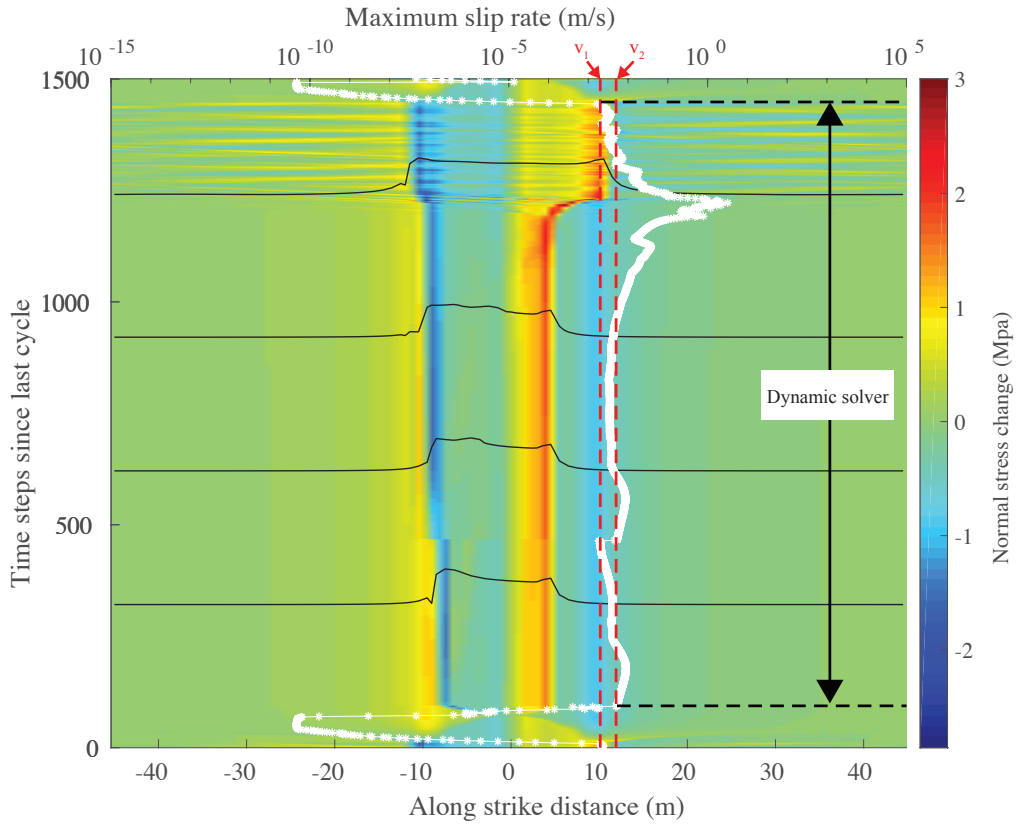


Figure 6.6: The normal stress change during a full earthquake cycle. Note that the vertical axis is not time but the number of time steps which is not linear with time. The white asterisk line is the plot of maximum slip rate. The black lines cross the whole domain is the log plot of slip velocity. $v_1$, $v_2$ is the critical velocity for transition from dynamic solver to quasi-static solver and the other way around.

mark test except that half of the domain has faster $V_p$ and $V_s$ (see Figure 6.2 values in the bracket for the upper half.) The fault slip profile of one full cycle is shown in Figure 6.5. Previous work have been done on the cycle simulation of a long rupture (Erickson and Day, 2016) where the rupture length is much larger than the critical nucleation size $h^*$. We here present the cycle simulation for the case when fault size is similar to $h^*$. There is normal stress reduction in $x < 0$ and increase in $x > 0$ due to the bimaterial effect that favors slip in the slip direction of the compliant medium(Figure 6.6). The consequent results of this normal stress change is that more slip is dissipated as slow slip (slip rate $|\dot{\delta}| < 0.01m/s$) in the $x < 0$ part and more slip is reserved for dynamic rupture in the other side. In Figure 6.6, I plot the normal stress change, together with maximum slip rate (white curve). The black lines that cross the whole fault length are the log plots of slip rate at different

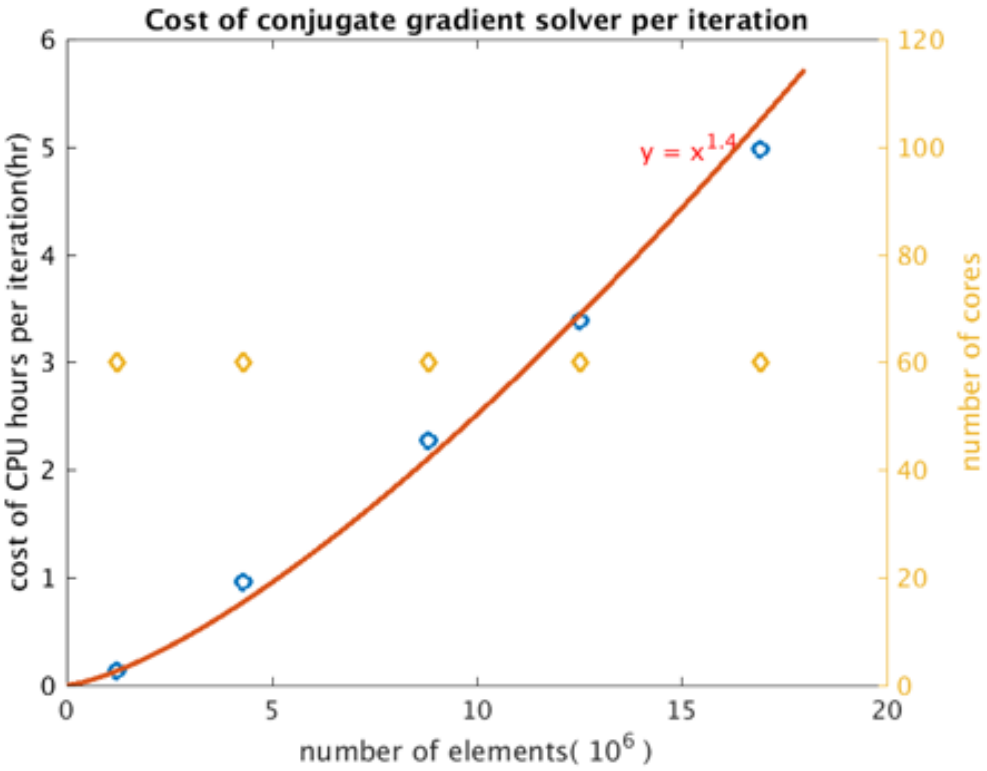


Figure 6.7: Plot of CPU hour cost with respect to number of elements in the domain and fitted with a power relation

snapshots. The two red dashed line are the critical velocity for the transition from quasi-static solver to dynamic solver ($v_2$) and the other way back ($v_1$).

## 6.6 Conclusion

Previous work has shown that the direct coupling of normal stress $\sigma$ to the calculation of shear stress may incur non-convergent solution (Ranjith and Rice, 2001; Cochard and Rice, 2000). It is thus suggested to use a second state variable to regularize the evolution of $\sigma$ (Ampuero and Ben-Zion, 2008). This will need to be included into the current code. The algorithm can be further extended for 3D simulations by leveraging the existing 3D spectral element solver (SPECFEM3D) developed by Komatitsch and Tromp (2002). The matrix inversion problem in Equation 6.29 can be solved by conjugate gradient method by iteratively apply the forward operator $DKD^T$ which can be done efficiently in SPECFEM3D with GPU. The conjugate gradient solver has been developed and testes with the solver's time complexity scale with $O(n^{1.4})$ (Figure 6.7) for a typical boundary value problem as described in Equation 6.29 and plotted in Figure 6.8.

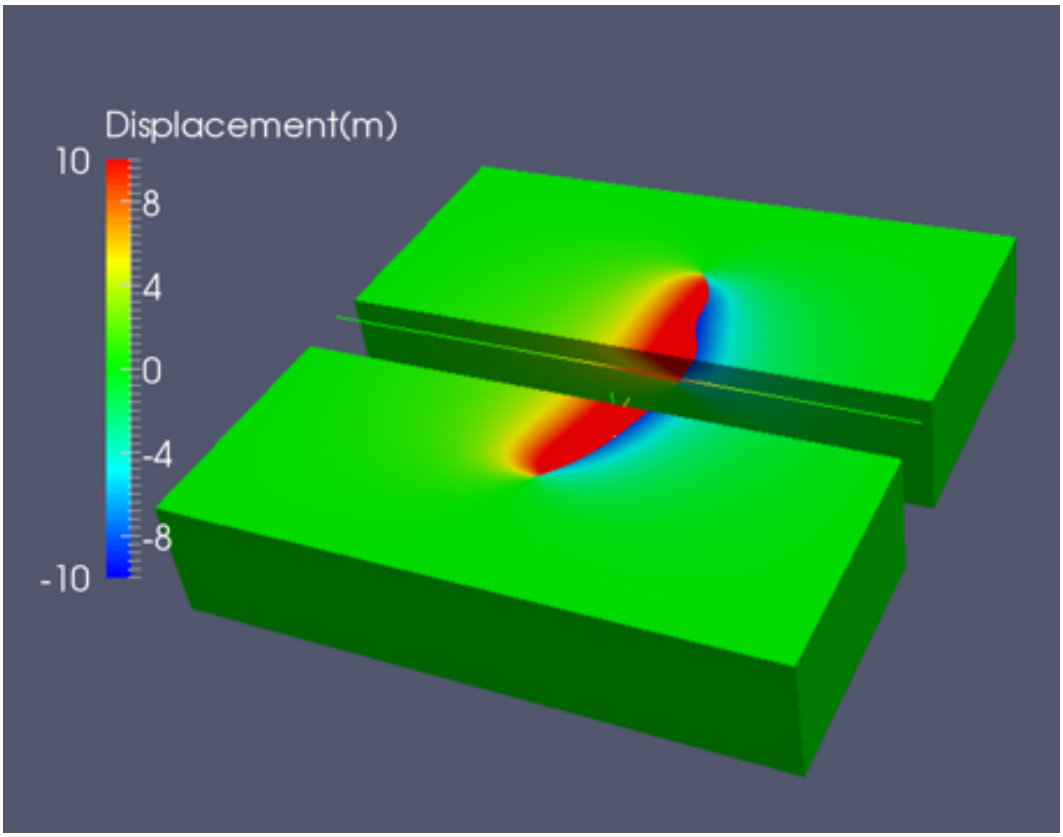


Figure 6.8: An example of a fault boundary value problem with complicated fault geometry.

*Appendix A*

# APPENDIX TO CHAPTER 2

## A.1 Critical step-over distance in the near-field and far-field regimes

We develop an upper bound on $H_c$ based on asymptotic stress analysis near a singular crack tip, ignoring the role of cohesive zone size $L_c$. The stress field at close distance $r$ and azimuth $\theta$ (counter-clockwise, relative to the rupture direction) from a running crack tip is

$$\sigma_{ij}(r,\theta) \approx \sigma_{0,ij}(r,\theta) + \frac{K_d \Sigma_{d,ij}(\theta)}{\sqrt{r}} \tag{A.1}$$

where $K_d$ is the dynamic stress intensity factor which is a function of rupture speed and $\Sigma_{d,ij}(\theta)$ is an angular pattern. Theory (Madariaga, 1977; Madariaga, 1983) and numerical simulations (Madariaga et al., 2006) show that this sudden change of stress intensity factor causes radiation of strong high frequency phases. If arrest is simultaneous along the terminal edge of the first fault, the stopping phase is radiated by a line source of finite length $W$. Hence, in the near field ($r/W \ll 1$) the stopping phase is approximately a cylindrical wave but in the far field ($r/W \gg 1$) it is a spherical wave. This creates two different amplitude-distance decay regimes: the stopping phase amplitude is proportional to $1/\sqrt{r}$ when $r/W \ll 1$ and to $1/r$ when $r/W \gg 1$. The stress field near the crack tip (at distance $r$ and azimuth $\theta$ from the first fault tip) when there is a sudden arrest of the rupture can be decomposed into three parts: 1) the background homogeneous stress $\sigma_{0,ij}$; 2) the static stress field $\sigma_{s,ij}(r,\theta)$ caused by the running rupture right before the rupture arrest $\sigma_{s,ij}(r,\theta) = \frac{K_d \Sigma_{d,ij}(\theta)}{\sqrt{r}}$; 3) The stopping phase caused by the simultaneous arrest of the rupture along the lateral edge. Only the third part is time dependent and we refer to Madariaga (1977) equation (36) which is the solution of S wave stopping phase for 2D in-plane shear rupture. We omit other complicated wave phenomenon while only keeping the S wave part of the stopping phase which we observed to be the major contributing factor. We compact all the other terms of Madariaga (1977) eq(36) into $\Sigma_{sp,ij}(V_r,\theta)$ while highlight the dependence of part 3) on $K_s$ and $r$

$$\sigma_{ij}(r,\theta,t) = \sigma_{0,ij} + \frac{K_d \Sigma_{d,ij}(\theta)}{\sqrt{r}} + \frac{K_s \Sigma_{sp,ij}(V_r,\theta)}{\sqrt{r}} H(t - r/V_s), \tag{A.2}$$

and in the far field

$$\sigma_{ij}(r,\theta,t) = \sigma_{0,ij} + \frac{C_s \Pi_{sp,ij}(Vr,\theta)}{r} H(r - t/V_s), \tag{A.3}$$

$\Sigma_{sp,ij}(V_r,\theta)$ and $\Pi_{sp,ij}(V_r,\theta)$ are near field and far field angular patterns. We have observed the rupture jump to occur after the pass of the stopping phase which means $H(r - t/V_s) = 1$. Since the dynamic wave field is much larger than the static component at large distance, we have omitted the static component in the far field expression. For a 3D rectangular crack with large aspect ratio ($L/W > 0.25$), $K$ at the short edge is very close to that of a mode II crack in 2D with length $W$ (Noda and Kihara, 2002): $K_s, K_d \propto \Delta\tau\sqrt{W}$ if $L \gg W$. We define

$$\kappa_{ij}(V_r,\theta) = \frac{K_d \Sigma_{d,ij}(\theta) + K_s \Sigma_{sp,ij}(V_r,\theta)}{\Delta\tau\sqrt{W}} \tag{A.4}$$

and

$$\xi_{ij}(Vr,\theta) = \frac{C_s \Pi_{sp,ij}(Vr,\theta)}{W\Delta\tau} \tag{A.5}$$

These quantities are dimensionless and have no dependencies on $W$ and $S$ ratio. After inserting these dimensionless quantities, the stress on the second fault is

$$\sigma_{ij}(r,\theta) = \sigma_{0,ij} + \frac{\kappa_{ij}(Vr,\theta)}{\sqrt{r/W}} \tag{A.6}$$

in the near field and

$$\sigma_{ij}(r,\theta) = \sigma_{0,ij} + \frac{\xi_{ij}(Vr,\theta)}{r/W} \tag{A.7}$$

in the far field. A necessary condition for rupture on the second fault is that the shear stress exceeds the static frictional strength:

$$\tau(r_c,\theta_c) > \mu_s \sigma(r_c,\theta_c) \tag{A.8}$$

where fault shear stress is $\tau = \sigma_{xy}$ and normal stress is $\sigma = \sigma_{yy}$. To satisfy this necessary condition with maximum step-over distance

$$H_c = r_c \sin(\theta_c) \tag{A.9}$$

we need to find $r_c$ and $\theta_c$ that maximize $r_c \sin(\theta_c)$ under the constraint A.8. Solving this optimization problem is difficult if $\theta_c$ depends on $S$. However, we have observed that $\theta_c$ is almost constant, with value near 30 degrees, in all our compressional step-over simulations. In dilational step-overs, for most cases with $W > 10$ km nucleation also occurs at a fixed azimuth of around $-120$ degree in the backward direction

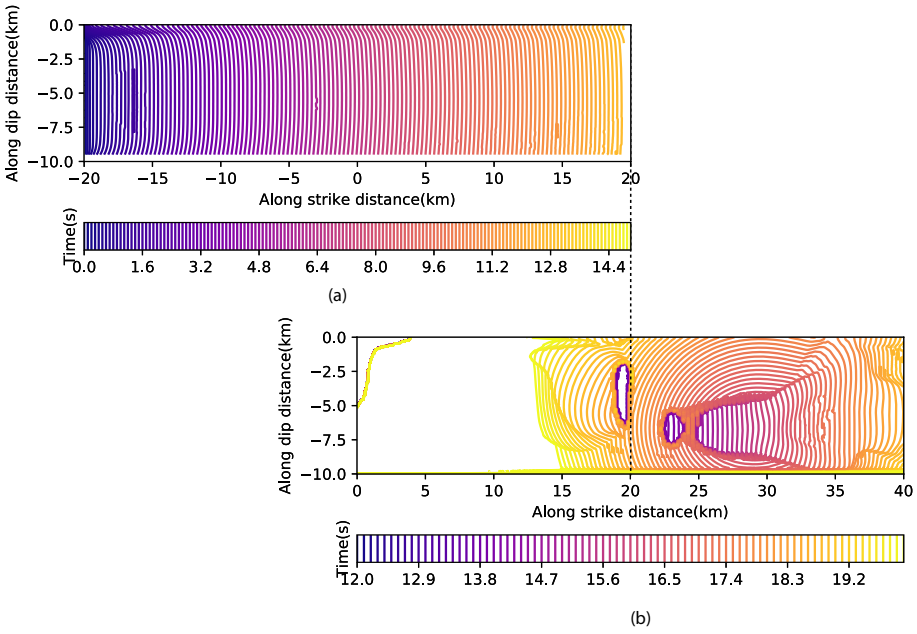


Figure A.1: Dilational step-over jump with three nucleation attempts. Successful nucleation in the forward direction with respect to the primary fault's end point. Seismogenic depth is $W = 10$ km. Rupture time contours on (a) primary fault and (b) secondary fault. The fault overlap section is $0 < x < 20$ km.

(Figure A.2), which is consistent with previous 2D simulations (Harris and Day, 1999). There are exceptions when $W < 10$ km in which the backward nucleation fails to develop into a sustained rupture (Figure A.1). Assuming a fixed $\theta_c$, the problem is reduced to finding the largest $H_c$ that satisfies the following relations:

$$\tau_0 + \Delta\tau \frac{\kappa_{xy}(V_r, \theta_c)(\sqrt{\sin(\theta_c)})}{\sqrt{H_c/W}} > \mu_s \left( \sigma_0 + \frac{\kappa_{yy}(V_r, \theta_c)\sqrt{\sin(\theta_c)}}{\sqrt{H_c/W}} \right) \tag{A.10}$$

in the near field and

$$\tau_0 + \Delta\tau \frac{\xi_{xy}(V_r, \theta_c)\sin(\theta_c)}{H_c/W} > \mu_s \left( \sigma_0 + \frac{\xi_{yy}(V_r, \theta_c)\sin(\theta_c)}{Hc/W} \right) \tag{A.11}$$

in the far field. The solution is

$$H_c/W = \frac{(\mu_s \kappa_{yy}(V_r, \theta_c) - \kappa_{xy}(V_r, \theta_c))^2 sin(\theta_c)}{S^2} \tag{A.12}$$

in the near field and

$$H_c/W = \frac{(\mu_s \xi_{yy}(V_r, \theta_c) - \xi_{xy}(V_r, \theta_c))sin(\theta_c)}{S} \tag{A.13}$$

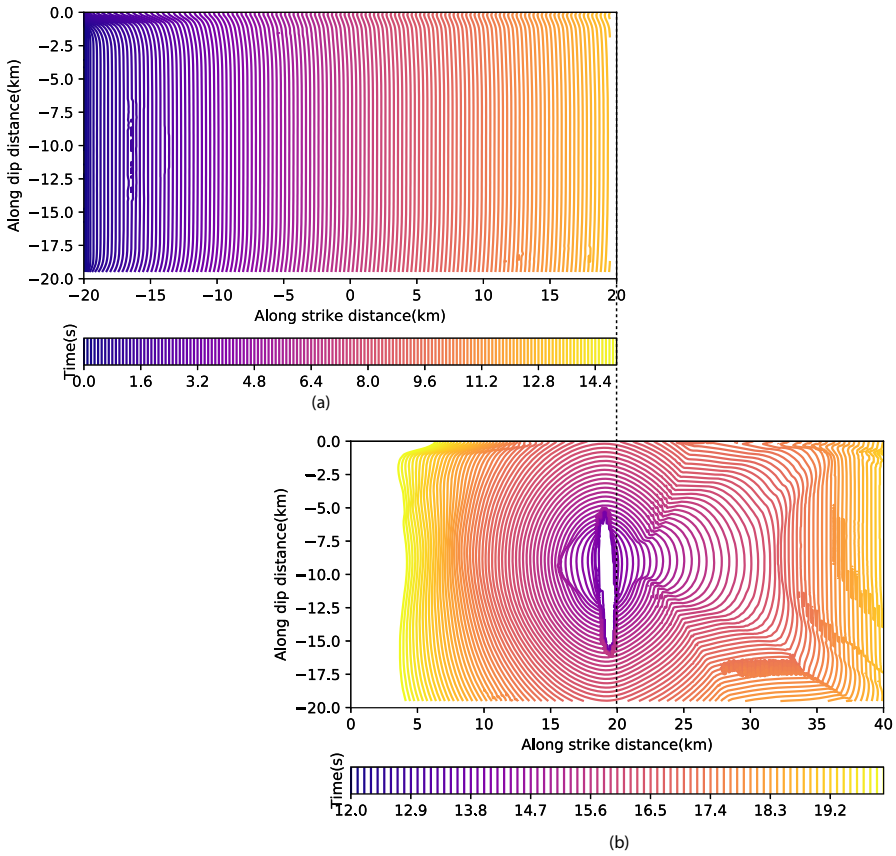


Figure A.2: Nucleation in the backward direction for a dilational stepover with $W = 20$ km.

in the far field.

Rupture speed is very similar in all our examples (Figure 2.5). Within that range, $V_r/V_s > 0.8$, rupture speed does not affect significantly the radiation amplitude in the azimuths we are interested in, as shown in appendix B. Hence $Hc/W$ is not significantly affected by $Vr$.

## A.2 Effect of $V_r$ on the amplitude of stopping phases

The first motion velocity amplitude of the S wave stopping phase of a Mode II crack is (equation (36) of (Madariaga, 1977)):

$$\frac{u^s(r,\theta,t)}{\partial t} = \frac{K_0}{\mu} V_r \frac{1}{\sqrt{r}} F_s(V_r,\theta) H(t - r/V_s) \tag{A.14}$$

where

$$F_s(V_r,\theta) = \frac{\kappa^3 cos(2\theta)cos(\theta/2)}{2(\kappa^2-1)(1-V_r/V_s cos\theta)(q_R+\kappa cos\theta)S(cos\theta/V_s)} \tag{A.15}$$

and $q_R$ is the Rayleigh function which depends on $V_r$ and $\kappa = V_p/V_s$. So

$$u^s_\theta(r,\psi,t) = \frac{K_0}{\mu}V_r\frac{1}{\sqrt{r}}F_s(V_r,\theta)R(t-r/V_s) \tag{A.16}$$

where $R(t) = \max(0,t)$ is the ramp function. Then

$$\frac{\partial u^s_\theta}{\partial r} = -\frac{1}{V_s}\frac{\partial u^s_\theta}{\partial t} - \frac{1}{2}\frac{K_0}{\mu}V_r\frac{1}{r^{3/2}}F_s(V_r,\theta)R(t-r/V_s) \tag{A.17}$$

$$\frac{\partial u^s_\theta}{\partial \theta} = \frac{K_0}{\mu}V_r\frac{1}{\sqrt{r}}F_s(V_r,\theta)R(t-r/V_s) \tag{A.18}$$

At $t = r/V_s$, we have $\frac{\partial u^s_\theta}{\partial t} = -\frac{1}{V_s}\frac{\partial u^s_\theta}{\partial r}$ and $\frac{\partial u^s_\theta}{\partial \theta} = 0$ We convert the strain tensor from cylindrical coordinates to Cartesian coordinates, and by introducing Lame's parameter $\lambda$ and $\mu$, stress can be calculated as:

$$\tau = \sigma_{xy} = \mu cos(2\theta)\frac{\partial u_\theta}{\partial r} \tag{A.19}$$

$$\sigma = \sigma_{yy} = \mu sin(2\theta)\frac{\partial u_\theta}{\partial r} \tag{A.20}$$

The only dependence of $\tau - \mu_s\sigma$ on $V_r$ is in the expression of $\partial u_\theta/\partial r$, via the term

$$f(V_r,\theta) = \frac{V_r/V_s}{(1-V_r/V_s cos\theta)(q_R+cos\theta)} \tag{A.21}$$

We plot the function $f(V_r,\theta)$ for a range of rupture speeds representative of our simulations and for a broad range of azimuths. In our simulations, $\theta = 30^\circ$ and $\theta = 120^\circ$ are the angles $\theta_c$ at which we observe compressional and dilational step-over jumps, respectively (Figure A.3).

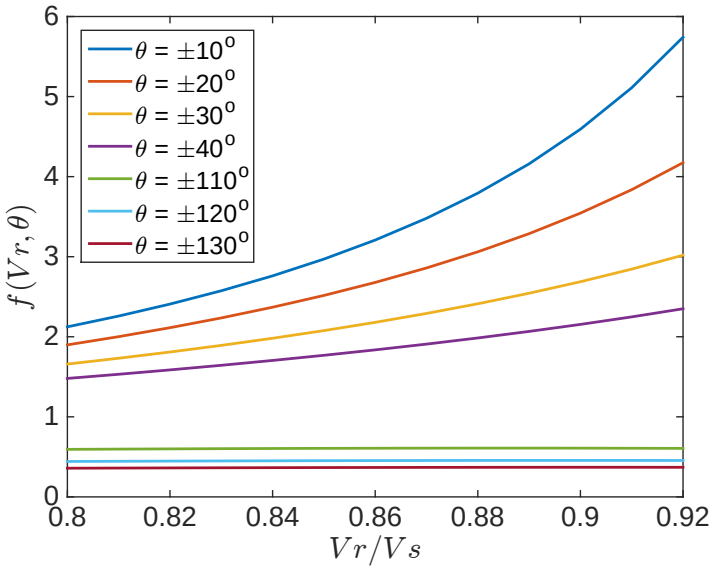


Figure A.3: The dependence of angular pattern on rupture speed $V_r$ at different azimuths. The dependence is smooth and weak within the range of azimuths and speeds we are interested in.

*Appendix B*

# APPENDIX TO CHAPTER 5

## B.1 Interference of beam-forming for a line source

Assume we have single frequency line sources $s = \{s_0, s_1, ...\}$ of length $D \gg \lambda$ with frequency $\omega$. The receivers $r$s are evenly distributed on a ring that is at a distance range $[L_{min}, L_{max}] \gg D$ from the sources (See Figure B.1). The matrix $G(\omega)$ is the propagation matrix from sources to receivers.

$$r = G(\omega)s$$

Beam-forming gives an image of the source in the form $G^*(\omega)G(\omega)s$. We hope $G^*G$ is equal to identity matrix so that beam-forming exactly recovers the source information however it is not. we show that it is only when the two sources $|s_i - s_j| \gg \lambda$, $[G^*G(\omega)]_{ij} \approx 0$. To simplify the analysis we neglect the effect of attenuation and geometric spreading. Then the propagation effect from the j source to the i receiver would simply be

$$\begin{aligned} G^*G(\omega)_{ij} &= \sum_k \exp(i\omega(T(s_i, r_k) - T(s_j, r_k))) \\ &= \int_{L_{min}}^{L_{max}} \int_0^{\pi} \exp(i\omega P(L)|x(s_i) - x(s_j)|cos\theta)\rho(L, \theta)d\theta dL \\ &= \int_{P(L_{min})}^{P(L_{max})} \int_0^{\pi} \exp(i2\pi V_p P(L)\frac{|x(s_i) - x(s_j)|}{\lambda}cos\theta)\rho(L, \theta)(\frac{dL}{dP})d\theta dP \end{aligned} \tag{B.1}$$

Here, $P(L)$ is the slowness at distance $L$ ,$V_p$ is the $P$ wave velocity at the earth surface and $\rho(L, \theta)$ is the receiver density which can be assumed as a constant. We also assume $\frac{dL}{dp}$ to be constant for simplicity. We take $P(L_{min}) = 0.5V_p$ and $P(L_{max}) = 0.3V_p$ which is very close to the situation of receivers at teleseismic distances from 30 °to 90 °. We plot out $[G^*G(\omega)]_{ij}$ as a function of $|x(s_i) - x(s_j)|/\lambda$ which is a dimensionless quantity. Since in a real world back projection, the receivers may not cover the full azimuth range, we also test the effect of limited azimuthal range from 0 °to 45 °. The comparison shows that when receivers cover full azimuth, the impulse response has a width of about $4\lambda$ which can be further expanded when only data from limited azimuthal range is available. The phase pattern is also very complicated which is indicative of potential constructive and

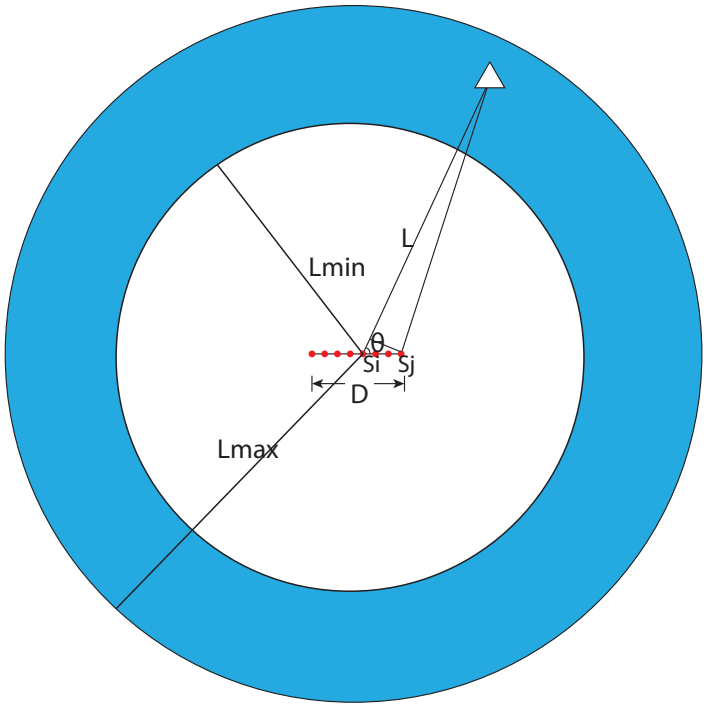


(A)

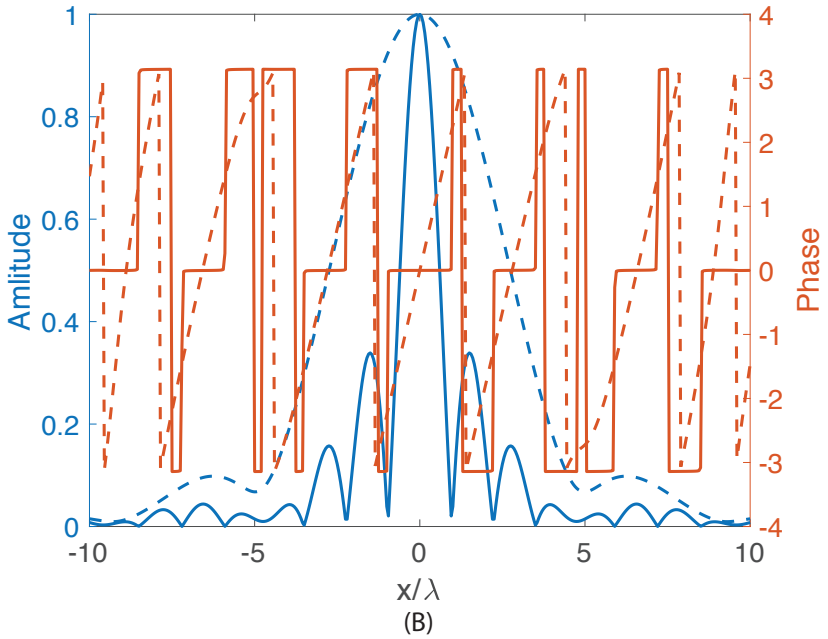


(B)

Figure B.1: Point source response of a single frequency source of wavelength $\lambda$.(B) plots the response with both amplitude (blue) and phase (red) as a function of spatial location of the test sources. We assume that the receivers have slowness from $0.3/V_p$ to $0.5/V_p$. The solid line plot the case with receiver cover an azimuth range from 0 °to 180 °. The dashed line plot the case with receiver cover an azimuth range from 0 °to 45 °.

destructive interference when multiple sources are very close to each other. We thus test the cases of continuous rupture represented by multiple point sources. Each source $s_i$ is represented by an amplitude $A_i$ multiplied by a phase shift computed from rupture time $T_i$:

$$s_i = A_i \exp(i\omega T_i) \tag{B.2}$$

We test three cases with all of them having a rupture length $D = 20\lambda$. The first case has uniform rupture speed $V_r = 0.5V_p$ and amplitude. The second case has spatial varying rupture speed with super-shear rupture interspersed between slow rupture. The third case has uniform rupture speed but spatial varying amplitude. We plot here the beam-forming image of the rupture processes. In the first example, due to destructive interference, there is only energy at the beginning and the end of the rupture. In the second and third example, the energy peaks corresponds to where the change of rupture speed or amplitude occurs.

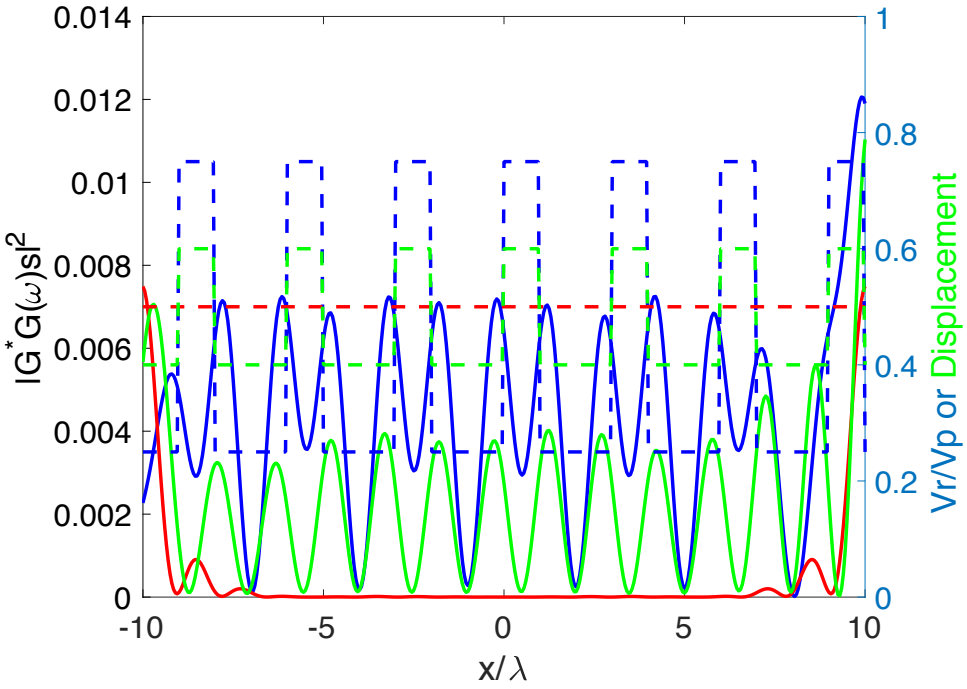


Figure B.2: Beam forming image of three experimental line sources. The red, blue and green solid lines are the beam forming energy (left axis) for a uniform line source , a line source with varying rupture speed and that with varying amplitude respectively. The red dashed line are the rupture speed and amplitude of the uniform rupture. The blue dashed line plots the rupture speed of the line source with varying rupture speed. The green dashed line plots the amplitude of the line source with varying amplitude in displacement.

# BIBLIOGRAPHY


Allmann, Bettina P. and Peter M. Shearer (2009). "Global variations of stress drop for moderate to large earthquakes". In: *Journal of Geophysical Research: Solid Earth* 114.B1. DOI: 10.1029/2008jb005821. URL: https://doi.org/10.1029/2008jb005821.

Ampuero, Jean Paul and Xiaolin Mao (2017). "Upper Limit on Damage Zone Thickness Controlled by Seismogenic Depth". In: pp. 243–253. DOI: 10.1002/9781119156895.ch13. URL: https://doi.org/10.1002/9781119156895.ch13.

Ampuero, J.-P. and Y. Ben-Zion (2008). "Cracks, pulses and macroscopic asymmetry of dynamic rupture on a bimaterial interface with velocity-weakening friction". In: *Geophysical Journal International* 173.2, pp. 674–692. DOI: 10.1111/j.1365-246x.2008.03736.x. URL: https://doi.org/10.1111/j.1365-246x.2008.03736.x.

Ampuero, J.-P., J.-P. Vilotte, and F. J. Sánchez-Sesma (2002). "Nucleation of rupture under slip dependent friction law: Simple models of fault zone". In: *Journal of Geophysical Research: Solid Earth* 107.B12, ESE 2–1–ESE 2–19. DOI: 10.1029/2001jb000452. URL: https://doi.org/10.1029/2001jb000452.

Andrews, D. J. (1976). "Rupture propagation with finite stress in antiplane strain". In: *Journal of Geophysical Research* 81.20, pp. 3575–3582. DOI: 10.1029/jb081i020p03575. URL: https://doi.org/10.1029/jb081i020p03575.

– (1980). "A stochastic fault model: 1. Static case". In: *Journal of Geophysical Research: Solid Earth* 85.B7, pp. 3867–3877. DOI: 10.1029/jb085ib07p03867. URL: https://doi.org/10.1029/jb085ib07p03867.

Andrews, Dudley Joe and Shuo Ma (2016). "Validating a Dynamic Earthquake Model to Produce Realistic Ground Motion". In: *Bulletin of the Seismological Society of America* 106.2, pp. 665–672. DOI: 10.1785/0120150251. URL: https://doi.org/10.1785/0120150251.

Aochi, Hideo (2003). "The role of fault continuity at depth in numerical simulations of earthquake rupture". In:

Avouac, Jean-Philippe et al. (2015). "Lower edge of locked Main Himalayan Thrust unzipped by the 2015 Gorkha earthquake". In: *Nature Geoscience* 8.9, pp. 708–711. DOI: 10.1038/ngeo2518. URL: https://doi.org/10.1038/ngeo2518.

Ben-Zion, Yehuda et al. (2003). "A shallow fault-zone structure illuminated by trapped waves in the Karadere-Duzce branch of the North Anatolian Fault, western Turkey". In: *Geophysical Journal International* 152.3, pp. 699–717. DOI: 10.1046/j.1365-246x.2003.01870.x. URL: https://doi.org/10.1046/j.1365-246x.2003.01870.x.

Biasi, Glenn P. and Steven G. Wesnousky (2016). "Steps and Gaps in Ground Ruptures: Empirical Bounds on Rupture Propagation". In: *Bulletin of the Seismological Society of America* 106.3, pp. 1110–1124. DOI: 10.1785/0120150175. URL: https://doi.org/10.1785/0120150175.

Boatwright, John and George L Choy (1992). "Acceleration source spectra anticipated for large earthquakes in northeastern North America". In: *Bulletin of the Seismological Society of America* 82.2, pp. 660–682.

Brace, W. F. and J. D. Byerlee (1966). "Stick-Slip as a Mechanism for Earthquakes". In: *Science* 153.3739, pp. 990–992. DOI: 10.1126/science.153.3739.990. URL: https://doi.org/10.1126/science.153.3739.990.

Bullen, KE (1965). "Models for the Density and Elasticity of the Earth's Lower Core". In: *Geophysical Journal International* 9.2-3, pp. 233–252. DOI: 10.1111/j.1365-246x.1965.tb02074.x. URL: https://doi.org/10.1111/j.1365-246x.1965.tb02074.x.

Burridge, R. and G. S. Halliday (1971). "Dynamic Shear Cracks with Friction as Models for Shallow Focus Earthquakes". In: *Geophysical Journal International* 25.1-3, pp. 261–283. DOI: 10.1111/j.1365-246x.1971.tb02339.x. URL: https://doi.org/10.1111/j.1365-246x.1971.tb02339.x.

Chen, Min et al. (2007). "Waveform modeling of the slab beneath Japan". In: *Journal of Geophysical Research* 112.B2. DOI: 10.1029/2006jb004394. URL: https://doi.org/10.1029/2006jb004394.

Chen, Ting and Nadia Lapusta (2009). "Scaling of small repeating earthquakes explained by interaction of seismic and aseismic slip in a rate and state fault model". In: *Journal of Geophysical Research: Solid Earth* 114.B1. DOI: 10.1029/2008jb005749. URL: https://doi.org/10.1029/2008jb005749.

Chu, Risheng, Brandon Schmandt, and Don V. Helmberger (2012). "Juan de Fuca subduction zone from a mixture of tomography and waveform modeling". In: *Journal of Geophysical Research: Solid Earth* 117.B3. DOI: 10.1029/2012jb009146. URL: https://doi.org/10.1029/2012jb009146.

Chu, Risheng, Lupei Zhu, and Don V. Helmberger (2009). "Determination of earthquake focal depths and source time functions in central Asia using teleseismicPwaveforms". In: *Geophysical Research Letters* 36.17. DOI: 10.1029/2009gl039494. URL: https://doi.org/10.1029/2009gl039494.

Chu, Risheng et al. (2011). "Initiation of the great Mw 9.0 Tohoku–Oki earthquake". In: *Earth and Planetary Science Letters* 308.3-4, pp. 277–283. DOI: 10.1016/j.epsl.2011.06.031. URL: https://doi.org/10.1016/j.epsl.2011.06.031.

Chu, Risheng et al. (2013). "Inversion of Source Parameters for Moderate Earthquakes Using Short-Period Teleseismic P Waves". In: *Pure and Applied Geophysics* 171.7, pp. 1329–1341. DOI: 10.1007/s00024-013-0719-1. URL: https://doi.org/10.1007/s00024-013-0719-1.

Cochard, A. and R. Madariaga (1996). "Complexity of seismicity due to highly rate-dependent friction". In: *Journal of Geophysical Research: Solid Earth* 101.B11, pp. 25321–25336. DOI: 10.1029/96jb02095. URL: https://doi.org/10.1029/96jb02095.

Cochard, A. and J. R. Rice (2000). "Fault rupture between dissimilar materials: Ill-posedness, regularization, and slip-pulse response". In: *Journal of Geophysical Research: Solid Earth* 105.B11, pp. 25891–25907. DOI: 10.1029/2000jb900230. URL: https://doi.org/10.1029/2000jb900230.

Cochard, Alain and Raul Madariaga (1994). "Dynamic faulting under rate-dependent friction". In: *Pure and Applied Geophysics PAGEOPH* 142.3-4, pp. 419–445. DOI: 10.1007/bf00876049. URL: https://doi.org/10.1007/bf00876049.

Cooke, Michele L. (1997). "Fracture localization along faults with spatially varying friction". In: *Journal of Geophysical Research: Solid Earth* 102.B10, pp. 22425–22434. ISSN: 2156-2202. DOI: 10.1029/97JB01829. URL: http://dx.doi.org/10.1029/97JB01829.

Copley, Alex et al. (2014). "Active faulting in apparently stable peninsular India: Rift inversion and a Holocene-age great earthquake on the Tapti Fault". In: *Journal of Geophysical Research: Solid Earth* 119.8, pp. 6650–6666. DOI: 10.1002/2014jb011294. URL: https://doi.org/10.1002/2014jb011294.

Courant, R., K. Friedrichs, and H. Lewy (1986). "Über die partiellen Differenzengleichungen der mathematischen Physik". In: *Kurt Otto Friedrichs*. Birkhäuser Boston, pp. 53–95. DOI: 10.1007/978-1-4612-5385-3_7. URL: https://doi.org/10.1007/978-1-4612-5385-3_7.

Creager, Kenneth C. and Thomas H. Jordan (1984). "Slab penetration into the lower mantle". In: *Journal of Geophysical Research: Solid Earth* 89.B5, pp. 3031–3049. DOI: 10.1029/jb089ib05p03031. URL: https://doi.org/10.1029/jb089ib05p03031.

Das, S. and K. Aki (1977a). "A numerical study of two-dimensional spontaneous rupture propagation". In: *Geophysical Journal International* 50.3, pp. 643–668. DOI: 10.1111/j.1365-246x.1977.tb01339.x. URL: https://doi.org/10.1111/j.1365-246x.1977.tb01339.x.

Das, Shamita and Keiiti Aki (1977b). "Fault plane with barriers: A versatile earthquake model". In: *Journal of Geophysical Research* 82.36, pp. 5658–5670. DOI: 10.1029/jb082i036p05658. URL: https://doi.org/10.1029/jb082i036p05658.

Davies, D. and B. R. Julian (1972). "A Study of Short Period P-wave Signals from Longshot". In: *Geophysical Journal International* 29.2, pp. 185–202. DOI: 10.1111/j.1365-246x.1972.tb02207.x. URL: https://doi.org/10.1111/j.1365-246x.1972.tb02207.x.

Day, Steven M (1982). "Three-dimensional simulation of spontaneous rupture: the effect of nonuniform prestress". In: *Bulletin of the Seismological Society of America* 72.6A, pp. 1881–1902.

Di Bucci, Daniela et al. (2006). "Seismotectonics of the southern Apennines and Adriatic foreland: Insights on active regional E-W shear zones from analogue modeling". In: *Tectonics* 25.4. TC4015, n/a–n/a. ISSN: 1944-9194. DOI: 10.1029/2005TC001898. URL: http://dx.doi.org/10.1029/2005TC001898.

Dieterich, James (1994). "A constitutive law for rate of earthquake production and its application to earthquake clustering". In: *Journal of Geophysical Research: Solid Earth* 99.B2, pp. 2601–2618. DOI: 10.1029/93jb02581. URL: https://doi.org/10.1029/93jb02581.

Dieterich, James H. (1979). "Modeling of rock friction: 1. Experimental results and constitutive equations". In: *Journal of Geophysical Research* 84.B5, p. 2161. DOI: 10.1029/jb084ib05p02161. URL: https://doi.org/10.1029/jb084ib05p02161.

Dieterich, James H. and Keith B. Richards-Dinger (2010). "Earthquake Recurrence in Simulated Fault Systems". In: *Pure and Applied Geophysics* 167.8-9, pp. 1087–1104. DOI: 10.1007/s00024-010-0094-0. URL: https://doi.org/10.1007/s00024-010-0094-0.

Duan, Benchun and David D. Oglesby (2006). "Heterogeneous fault stresses from previous earthquakes and the effect on dynamics of parallel strike-slip faults". In: *Journal of Geophysical Research: Solid Earth* 111.B5, n/a–n/a. DOI: 10.1029/2005jb004138. URL: https://doi.org/10.1029/2005jb004138.

Dunham, Eric M. (2007). "Conditions governing the occurrence of supershear ruptures under slip-weakening friction". In: *Journal of Geophysical Research* 112.B7. DOI: 10.1029/2006jb004717. URL: https://doi.org/10.1029/2006jb004717.

Dziewonski, Adam M. and Don L. Anderson (1981). "Preliminary reference Earth model". In: *Physics of the Earth and Planetary Interiors* 25.4, pp. 297–356. DOI: 10.1016/0031-9201(81)90046-7. URL: https://doi.org/10.1016/0031-9201%2881%2990046-7.

Elliott, A. J., J. F. Dolan, and D. D. Oglesby (2009). "Evidence from coseismic slip gradients for dynamic control on rupture propagation and arrest through stepovers". In: *Journal of Geophysical Research* 114.B2. DOI: 10.1029/2008jb005969. URL: https://doi.org/10.1029/2008jb005969.

Erickson, Brittany A. and Steven M. Day (2016). "Bimaterial effects in an earthquake cycle model using rate-and-state friction". In: *Journal of Geophysical Research: Solid Earth* 121.4, pp. 2480–2506. DOI: 10.1002/2015jb012470. URL: https://doi.org/10.1002/2015jb012470.

Etopo2 (2006). "2-minute Gridded Global Relief Data (ETOPO2) v2." In: *National Geophysical Data Center, NOAA*. DOI: doi:10.7289/V5J1012Q. URL: https://doi.org/10.7289/V5J1012Q.

Field, Edward H et al. (2014). "Uniform California earthquake rupture forecast, version 3 (UCERF3)—The time-independent model". In: *Bulletin of the Seismological Society of America* 104.3, pp. 1122–1180.

Finzi, Y. and S. Langer (2012a). "Damage in step-overs may enable large cascading earthquakes". In: *Geophysical Research Letters* 39.16, n/a–n/a. DOI: 10.1029/2012gl052436. URL: https://doi.org/10.1029/2012gl052436.

– (2012b). "Predicting rupture arrests, rupture jumps and cascading earthquakes". In: *Journal of Geophysical Research: Solid Earth* 117.B12, n/a–n/a. DOI: 10.1029/2012jb009544. URL: https://doi.org/10.1029/2012jb009544.

Fukahata, Yukitoshi, Yuji Yagi, and Luis Rivera (2013). "Theoretical relationship between back-projection imaging and classical linear inverse solutions". In: *Geophysical Journal International* 196.1, pp. 552–559. DOI: 10.1093/gji/ggt392. URL: https://doi.org/10.1093/gji/ggt392.

Fukuyama, E. (2003). "Estimation of the Critical Slip-Weakening Distance: Theoretical Background". In: *Bulletin of the Seismological Society of America* 93.4, pp. 1835–1840. DOI: 10.1785/0120020184. URL: https://doi.org/10.1785/0120020184.

Galetzka, J. et al. (2015). "Slip pulse and resonance of the Kathmandu basin during the 2015 Gorkha earthquake, Nepal". In: *Science* 349.6252, pp. 1091–1095. DOI: 10.1126/science.aac6383. URL: https://doi.org/10.1126/science.aac6383.

Galis, Martin et al. (2017). "Theoretical estimates of magnitudes of earthquakes induced by pore-pressure perturbations with large aspect ratios". In: *EGU General Assembly Conference Abstracts*. Vol. 19, p. 6111.

Galis, M. et al. (2014). "On the initiation of sustained slip-weakening ruptures by localized stresses". In: *Geophysical Journal International* 200.2, pp. 890–909. DOI: 10.1093/gji/ggu436. URL: https://doi.org/10.1093/gji/ggu436.

Galvez, P. et al. (2014). "Dynamic earthquake rupture modelled with an unstructured 3-D spectral element method applied to the 2011 M9 Tohoku earthquake". In: *Geophysical Journal International* 198.2, pp. 1222–1240. DOI: 10.1093/gji/ggu203. URL: https://doi.org/10.1093/gji/ggu203.

Grandin, Raphaël et al. (2015). "Rupture process of the Mw = 7.9 2015 Gorkha earthquake (Nepal): Insights into Himalayan megathrust segmentation". In: *Geophysical Research Letters* 42.20, pp. 8373–8382. DOI: 10.1002/2015gl066044. URL: https://doi.org/10.1002/2015gl066044.

Graymer, R. W. et al. (2007). "Relatively simple through-going fault planes at large-earthquake depth may be concealed by the surface complexity of strike-slip faults". In: *Geological Society, London, Special Publications* 290.1, pp. 189–201. DOI: 10.1144/sp290.5. URL: https://doi.org/10.1144/sp290.5.

Guatteri, M. (2003). "Strong Ground-Motion Prediction from Stochastic-Dynamic Source Models". In: *Bulletin of the Seismological Society of America* 93.1, pp. 301–313. DOI: 10.1785/0120020006. URL: https://doi.org/10.1785/0120020006.

Gutenberg, Beno and Charles F Richter (1944). "Frequency of earthquakes in California". In: *Bulletin of the Seismological Society of America* 34.4, pp. 185–188.

Hamling, Ian J. et al. (2017). "Complex multifault rupture during the 2016 M w 7.8 Kaikōura earthquake, New Zealand". In: *Science* 356.6334, eaam7194. DOI: 10.1126/science.aam7194. URL: https://doi.org/10.1126/science.aam7194.

Harris, Ruth A., Ralph J. Archuleta, and Steven M. Day (1991). "Fault steps and the dynamic rupture process: 2-D numerical simulations of a spontaneously propagating shear fracture". In: *Geophysical Research Letters* 18.5, pp. 893–896. ISSN: 1944-8007. DOI: 10.1029/91GL01061. URL: http://dx.doi.org/10.1029/91GL01061.

Harris, Ruth A. and Steven M. Day (1999). "Dynamic 3D simulations of earthquakes on En Echelon Faults". In: *Geophysical Research Letters* 26.14, pp. 2089–2092. DOI: 10.1029/1999gl900377. URL: https://doi.org/10.1029/1999gl900377.

Hayes, Gavin P., David J. Wald, and Rebecca L. Johnson (2012). "Slab1.0: A three-dimensional model of global subduction zone geometries". In: *Journal of Geophysical Research: Solid Earth* 117.B1, n/a–n/a. DOI: 10.1029/2011jb008524. URL: https://doi.org/10.1029/2011jb008524.

Helmberger, D. V. and S. Ni (2005). "Approximate 3D Body-Wave Synthetics for Tomographic Models". In: *Bulletin of the Seismological Society of America* 95.1, pp. 212–224. DOI: 10.1785/0120040004. URL: https://doi.org/10.1785/0120040004.

Helmberger, DV (1983). "Theory and application of synthetic seismograms". In: *Earthquakes: observation, theory and interpretation*, pp. 174–222.

Herbert, Justin W. et al. (2014). "How much can off-fault deformation contribute to the slip rate discrepancy within the eastern California shear zone?" In: *Geology* 42.1, pp. 71–75. DOI: 10.1130/g34738.1. URL: https://doi.org/10.1130/g34738.1.

Hillers, G., Y. Ben-Zion, and P. M. Mai (2006). "Seismicity on a fault controlled by rate- and state-dependent friction with spatial variations of the critical slip distance". In: *Journal of Geophysical Research* 111.B1. DOI: 10.1029/2005jb003859. URL: https://doi.org/10.1029/2005jb003859.

Hu, Feng, Zhenguo Zhang, and Xiaofei Chen (2016). "Investigation of earthquake jump distance for strike-slip step overs based on 3-D dynamic rupture simulations in an elastic half-space". In: *Journal of Geophysical Research: Solid Earth* 121.2, pp. 994–1006. DOI: 10.1002/2015jb012696. URL: https://doi.org/10.1002/2015jb012696.

Huang, Yihe and Jean-Paul Ampuero (2011). "Pulse-like ruptures induced by low-velocity fault zones". In: *Journal of Geophysical Research* 116.B12. DOI: 10.1029/2011jb008684. URL: https://doi.org/10.1029/2011jb008684.

Huang, Yihe, Jean-Paul Ampuero, and Don V. Helmberger (2014). "Earthquake ruptures modulated by waves in damaged fault zones". In: *Journal of Geophysical Research: Solid Earth* 119.4. 2013JB010724, pp. 3133–3154. ISSN: 2169-9356. DOI: 10.1002/2013JB010724. URL: http://dx.doi.org/10.1002/2013JB010724.

Ida, Yoshiaki (1972). "Cohesive force across the tip of a longitudinal-shear crack and Griffith's specific surface energy". In: *Journal of Geophysical Research* 77.20, pp. 3796–3805. ISSN: 2156-2202. DOI: 10.1029/JB077i020p03796. URL: http://dx.doi.org/10.1029/JB077i020p03796.

Ide, Satoshi et al. (2007). "A scaling law for slow earthquakes". In: *Nature* 447.7140, pp. 76–79. DOI: 10.1038/nature05780. URL: https://doi.org/10.1038/nature05780.

Ikari, Matt J., Demian M. Saffer, and Chris Marone (2009). "Frictional and hydrologic properties of clay-rich fault gouge". In: *Journal of Geophysical Research* 114.B5. DOI: 10.1029/2008jb006089. URL: https://doi.org/10.1029/2008jb006089.

Ishii, Miaki et al. (2005). "Extent, duration and speed of the 2004 Sumatra–Andaman earthquake imaged by the Hi-Net array". In: *Nature* 435.7044, pp. 933–936. DOI: 10.1038/nature03675. URL: https://doi.org/10.1038/nature03675.

Ji, C. (2002a). "Source Description of the 1999 Hector Mine, California, Earthquake, Part I: Wavelet Domain Inversion Theory and Resolution Analysis". In: *Bulletin of the Seismological Society of America* 92.4, pp. 1192–1207. DOI: 10.1785/0120000916. URL: https://doi.org/10.1785/0120000916.

– (2002b). "Source Description of the 1999 Hector Mine, California, Earthquake, Part II: Complexity of Slip History". In: *Bulletin of the Seismological Society of America* 92.4, pp. 1208–1226. DOI: 10.1785/0120000917. URL: https://doi.org/10.1785/0120000917.

Jiang, J. and N. Lapusta (2016). "Deeper penetration of large earthquakes on seismically quiescent faults". In: *Science* 352.6291, pp. 1293–1297. DOI: 10.1126/science.aaf1496. URL: https://doi.org/10.1126/science.aaf1496.

Joussineau, Ghislain de and Atilla Aydin (2007). "The evolution of the damage zone with fault growth in sandstone and its multiscale characteristics". In: *Journal of Geophysical Research* 112.B12. DOI: 10.1029/2006jb004711. URL: https://doi.org/10.1029/2006jb004711.

Kagan, Yan Y. (2010a). "Earthquake size distribution: Power-law with exponent ?" In: *Tectonophysics* 490.1-2, pp. 103–114. DOI: 10.1016/j.tecto.2010.04.034. URL: https://doi.org/10.1016/j.tecto.2010.04.034.

– (2010b). "Earthquake size distribution: Power-law with exponent 1/2?" In: *Tectonophysics* 490.1-2, pp. 103–114. DOI: 10.1016/j.tecto.2010.04.034. URL: https://doi.org/10.1016/j.tecto.2010.04.034.

Kame, Nobuki and Koji Uchida (2008). "Seismic radiation from dynamic coalescence, and the reconstruction of dynamic source parameters on a planar fault". In: *Geophysical Journal International* 174.2, pp. 696–706.

Kaneko, Y., J.-P. Ampuero, and N. Lapusta (2011). "Spectral-element simulations of long-term fault slip: Effect of low-rigidity layers on earthquake-cycle dynamics". In: *Journal of Geophysical Research* 116.B10. DOI: 10.1029/2011jb008395. URL: https://doi.org/10.1029/2011jb008395.

Kaneko, Y., N. Lapusta, and J.-P. Ampuero (2008). "Spectral element modeling of spontaneous earthquake rupture on rate and state faults: Effect of velocity-strengthening friction at shallow depths". In: *Journal of Geophysical Research* 113.B9. DOI: 10.1029/2007jb005553. URL: https://doi.org/10.1029/2007jb005553.

Kato, Naoyuki (2004). "Interaction of slip on asperities: Numerical simulation of seismic cycles on a two-dimensional planar fault with nonuniform frictional property". In: *Journal of Geophysical Research* 109.B12. DOI: 10.1029/2004jb003001. URL: https://doi.org/10.1029/2004jb003001.

– (2009). "A possible explanation for difference in stress drop between intraplate and interplate earthquakes". In: *Geophysical Research Letters* 36.23. DOI: 10.1029/2009gl040985. URL: https://doi.org/10.1029/2009gl040985.

– (2012). "Dependence of earthquake stress drop on critical slip-weakening distance". In: *Journal of Geophysical Research: Solid Earth* 117.B1, n/a–n/a. DOI: 10.1029/2011jb008359. URL: https://doi.org/10.1029/2011jb008359.

Kerr, Ann U (1985). *VELA program. A twenty-five year review of basic research*. Tech. rep. Defense Advanced Research Projects Agency, Arlington, VA (USA).

Ko, Justin Yen-Ting et al. (2017). "Lower Mantle Substructure Embedded in the Farallon Plate: The Hess Conjugate". In: *Geophysical Research Letters* 44.20, pp. 10, 216–10, 225. DOI: 10.1002/2017gl075032. URL: https://doi.org/10.1002/2017gl075032.

Koketsu, Kazuki et al. (2016). "Widespread ground motion distribution caused by rupture directivity during the 2015 Gorkha, Nepal earthquake". In: *Scientific Reports* 6.1. DOI: 10.1038/srep28536. URL: https://doi.org/10.1038/srep28536.

Komatitsch, Dimitri and Jeroen Tromp (1999). "Introduction to the spectral element method for three-dimensional seismic wave propagation". In: *Geophysical Journal International* 139.3, p. 806. DOI: 10.1046/j.1365-246x.1999.00967.x. URL: http://dx.doi.org/10.1046/j.1365-246x.1999.00967.x.

– (2002). "Spectral-element simulations of global seismic wave propagation-I. Validation". In: *Geophysical Journal International* 149.2, pp. 390–412. DOI: 10.1046/j.1365-246x.2002.01653.x. URL: https://doi.org/10.1046/j.1365-246x.2002.01653.x.

Komatitsch, Dimitri and Jean-Pierre Vilotte (1998). "The spectral element method: an efficient tool to simulate the seismic response of 2D and 3D geological structures". In: *Bulletin of the seismological society of America* 88.2, pp. 368–392.

Komatitsch, Dimitri et al. (2010). "Modeling the propagation of elastic waves using spectral elements on a cluster of 192 GPUs". In: *Computer Science - Research and Development* 25.1-2, pp. 75–82. DOI: 10.1007/s00450-010-0109-1. URL: https://doi.org/10.1007/s00450-010-0109-1.

Kostrov, B.V. (1964). "Selfsimilar problems of propagation of shear cracks". In: *Journal of Applied Mathematics and Mechanics* 28.5, pp. 1077–1087. DOI: 10.1016/0021-8928(64)90010-3. URL: https://doi.org/10.1016/0021-8928%2864%2990010-3.

Langston, Charles A. and Donald V. Helmberger (2007). "A Procedure for Modelling Shallow Dislocation Sources". In: *Geophysical Journal of the Royal Astronomical Society* 42.1, pp. 117–130. DOI: 10.1111/j.1365-246x.1975.tb05854.x. URL: https://doi.org/10.1111/j.1365-246x.1975.tb05854.x.

Lapusta, Nadia and Yi Liu (2009). "Three-dimensional boundary integral modeling of spontaneous earthquake sequences and aseismic slip". In: *Journal of Geophysical Research* 114.B9. DOI: 10.1029/2008jb005934. URL: https://doi.org/10.1029/2008jb005934.

Lay, Thorne et al. (2012). "Depth-varying rupture properties of subduction zone megathrust faults". In: *Journal of Geophysical Research: Solid Earth* 117.B4, n/a–n/a. DOI: 10.1029/2011jb009133. URL: https://doi.org/10.1029/2011jb009133.

Lay, Thorne et al. (2017). "Assessment of teleseismically-determined source parameters for the April 25, 2015 M W 7.9 Gorkha, Nepal earthquake and the May 12, 2015 M W 7.2 aftershock". In: *Tectonophysics* 714-715, pp. 4–20. DOI: 10.1016/j.tecto.2016.05.023. URL: https://doi.org/10.1016/j.tecto.2016.05.023.

Lewis, Michael A. and Yehuda Ben-Zion (2010). "Diversity of fault zone damage and trapping structures in the Parkfield section of the San Andreas Fault from comprehensive analysis of near fault seismograms". In: *Geophysical Journal International* 183.3, pp. 1579–1595. DOI: 10.1111/j.1365-246x.2010.04816.x. URL: https://doi.org/10.1111/j.1365-246x.2010.04816.x.

Li, Dunzhu et al. (2014). "Global synthetic seismograms using a 2-D finite-difference method". In: *Geophysical Journal International* 197.2, pp. 1166–1183. DOI: 10.1093/gji/ggu050. URL: https://doi.org/10.1093/gji/ggu050.

Liu, P., R. J. Archuleta, and S. H. Hartzell (2006). "Prediction of Broadband Ground-Motion Time Histories: Hybrid Low/High- Frequency Method with Correlated Random Source Parameters". In: *Bulletin of the Seismological Society of America* 96.6, pp. 2118–2130. DOI: 10.1785/0120060036. URL: https://doi.org/10.1785/0120060036.

Liu, Yajing and J. Rice (2005). "Aseismic slip transients emerge spontaneously in three-dimensional rate and state modeling of subduction earthquake sequences". In: *Journal of Geophysical Research* 110.B8. DOI: 10.1029/2004jb003424. URL: https://doi.org/10.1029/2004jb003424.

Lozos, J. C., J. H. Dieterich, and D. D. Oglesby (2014a). "The Effects of d0 on Rupture Propagation on Fault Stepovers". In: *Bulletin of the Seismological Society of America* 104.4, pp. 1947–1953. DOI: 10.1785/0120130305. URL: https://doi.org/10.1785/0120130305.

Lozos, Julian C. et al. (2014b). "Rupture Propagation and Ground Motion of Strike-Slip Stepovers with Intermediate Fault Segments". In: *Bulletin of the Seismological Society of America* 105.1, pp. 387–399. DOI: 10.1785/0120140114. URL: https://doi.org/10.1785/0120140114.

Lu, Chang and Stephen P. Grand (2016). "The effect of subducting slabs in global shear wave tomography". In: *Geophysical Journal International* 205.2, pp. 1074–1085. DOI: 10.1093/gji/ggw072. URL: https://doi.org/10.1093/gji/ggw072.

Lui, Semechah K. Y. et al. (2015). "Interrogation of the Megathrust Zone in the Tohoku-Oki Seismic Region by Waveform Complexity: Intraslab Earthquake Rupture and Reactivation of Subducted Normal Faults". In: *Pure and Applied Geophysics* 172.12, pp. 3425–3437. DOI: 10.1007/s00024-015-1042-9. URL: https://doi.org/10.1007/s00024-015-1042-9.

Luo, Yingdi and Jean-Paul Ampuero (2017). "Stability of faults with heterogeneous friction properties and effective normal stress". In: *Tectonophysics*. DOI: 10.1016/j.tecto.2017.11.006. URL: https://doi.org/10.1016/j.tecto.2017.11.006.

Luo, Yingdi et al. (2017a). *QDYN: a Quasi-DYNamic earthquake simulator (v1.1)*. DOI: 10.5281/zenodo.322459. URL: https://doi.org/10.5281/zenodo.322459.

Luo, Yingdi et al. (2017b). "Surface Rupture Effects on Earthquake Moment-Area Scaling Relations". In: *Pure and Applied Geophysics* 174.9, pp. 3331–3342. DOI: 10.1007/s00024-017-1467-4. URL: https://doi.org/10.1007/s00024-017-1467-4.

Madariaga, R. (1977). "High-frequency radiation from crack (stress drop) models of earthquake faulting". In: *Geophysical Journal International* 51.3, pp. 625–651. DOI: 10.1111/j.1365-246x.1977.tb04211.x. URL: https://doi.org/10.1111/j.1365-246x.1977.tb04211.x.

– (1983). "High frequency radiation from dynamic earthquake fault models". In: *Ann. Geophys.,* 1, pp. 17–23.

Madariaga, R., J. P. Ampuero, and M. Adda-Bedia (2006). "Seismic radiation from simple models of earthquakes". In: pp. 223–236. DOI: 10.1029/170gm23. URL: https://doi.org/10.1029/170gm23.

Madariaga, Raul (1976). "Dynamics of an expanding circular fault". In: *Bulletin of the Seismological Society of America* 66.3, p. 639. eprint: /gsw/content_public/journal/bssa/66/3/0037110666030001/3/bssa0660030639.pdf.

Madariaga, Raul and Kim B. Olsen (2000). "Criticality of Rupture Dynamics in 3-D". In: *Microscopic and Macroscopic Simulation: Towards Predictive Modelling of the Earthquake Process*. Birkhäuser Basel, pp. 1981–2001. DOI: 10.1007/978-3-0348-7695-7_10. URL: https://doi.org/10.1007/978-3-0348-7695-7_10.

Mai, P. Martin and Gregory C. Beroza (2002). "A spatial random field model to characterize complexity in earthquake slip". In: *Journal of Geophysical Research: Solid Earth* 107.B11, ESE 10–1–ESE 10–21. DOI: 10.1029/2001jb000588. URL: https://doi.org/10.1029/2001jb000588.

Marone, Chris (1998). "LABORATORY-DERIVED FRICTION LAWS AND THEIR APPLICATION TO SEISMIC FAULTING". In: *Annual Review of Earth and Planetary Sciences* 26.1, pp. 643–696. DOI: 10.1146/annurev.earth.26.1.643. URL: https://doi.org/10.1146/annurev.earth.26.1.643.

Marone, Chris and C. H. Scholz (1988). "The depth of seismic faulting and the upper transition from stable to unstable slip regimes". In: *Geophysical Research Letters* 15.6, pp. 621–624. DOI: 10.1029/gl015i006p00621. URL: https://doi.org/10.1029/gl015i006p00621.

Meng, Lingsen, Asaf Inbal, and Jean-Paul Ampuero (2011). "A window into the complexity of the dynamic rupture of the 2011 Mw 9 Tohoku-Oki earthquake". In: *Geophysical Research Letters* 38.7, n/a–n/a. DOI: 10.1029/2011gl048118. URL: https://doi.org/10.1029/2011gl048118.

Meng, L. et al. (2012). “Earthquake in a Maze: Compressional Rupture Branching During the 2012 Mw 8.6 Sumatra Earthquake”. In: *Science* 337.6095, pp. 724–726. DOI: 10.1126/science.1224030. URL: https://doi.org/10.1126/science.1224030.

Michel, Sylvain et al. (2017). “Pulse-like partial ruptures and high-frequency radiation at creeping-locked transition during megathrust earthquakes”. In: *Geophysical Research Letters* 44.16, pp. 8345–8351.

Mikumo, T. (2003). “Stress-Breakdown Time and Slip-Weakening Distance Inferred from Slip-Velocity Functions on Earthquake Faults”. In: *Bulletin of the Seismological Society of America* 93.1, pp. 264–282. DOI: 10.1785/0120020082. URL: https://doi.org/10.1785/0120020082.

Monsalve, G et al. (2008). “Seismic structure of the crust and the upper mantle beneath the Himalayas: Evidence for eclogitization of lower crustal rocks in the Indian Plate”. In: *Journal of Geophysical Research: Solid Earth* 113.B8.

Myers, Rodrick and Atilla Aydin (2004). “The evolution of faults formed by shearing across joint zones in sandstone”. In: *Journal of Structural Geology* 26.5, pp. 947–966. DOI: 10.1016/j.jsg.2003.07.008. URL: https://doi.org/10.1016/j.jsg.2003.07.008.

Naylor, M.A, G Mandl, and C.H.K Supesteijn (1986). “Fault geometries in basement-induced wrench faulting under different initial stress states”. In: *Journal of Structural Geology* 8.7, pp. 737–752. DOI: 10.1016/0191-8141(86)90022-2. URL: https://doi.org/10.1016/0191-8141%2886%2990022-2.

Ni, S. (2003). “A Comparison of Synthetic Seismograms for 2D Structures: Semi-analytical versus Numerical”. In: *Bulletin of the Seismological Society of America* 93.6, pp. 2752–2757. DOI: 10.1785/0120030011. URL: https://doi.org/10.1785/0120030011.

Ni, Sidao, Don V. Helmberger, and Jeroen Tromp (2005). “Three-dimensional structure of the African superplume from waveform modelling”. In: *Geophysical Journal International* 161.2, pp. 283–294. DOI: 10.1111/j.1365-246X.2005.02508.x. eprint: /oup/backfile/content_public/journal/gji/161/2/10.1111/j.1365-246x.2005.02508.x/3/161-2-283.pdf. URL: http://dx.doi.org/10.1111/j.1365-246X.2005.02508.x.

Noda, Hiroyuki, Eric M. Dunham, and James R. Rice (2009). “Earthquake ruptures with thermal weakening and the operation of major faults at low overall stress levels”. In: *Journal of Geophysical Research* 114.B7. DOI: 10.1029/2008jb006143. URL: https://doi.org/10.1029/2008jb006143.

Noda, Hiroyuki and Nadia Lapusta (2013). “Stable creeping fault segments can become destructive as a result of dynamic weakening”. In: *Nature* 493.7433, pp. 518–521. DOI: 10.1038/nature11703. URL: https://doi.org/10.1038/nature11703.

Noda, Hiroyuki, Masao Nakatani, and Takane Hori (2013). "Large nucleation before large earthquakes is sometimes skipped due to cascade-up-Implications from a rate and state simulation of faults with hierarchical asperities". In: *Journal of Geophysical Research: Solid Earth* 118.6, pp. 2924–2952. DOI: 10.1002/jgrb.50211. URL: https://doi.org/10.1002/jgrb.50211.

Noda, N.-A. and T.-A. Kihara (2002). "Variation of the stress intensity factor along the front of a 3-D rectangular crack subjected to mixed-mode load". In: *Archive of Applied Mechanics (Ingenieur Archiv)* 72.8, pp. 599–614. DOI: 10.1007/s00419-002-0232-y. URL: https://doi.org/10.1007/s00419-002-0232-y.

Obayashi, Masayuki et al. (2013). "Finite frequency whole mantlePwave tomography: Improvement of subducted slab images". In: *Geophysical Research Letters* 40.21, pp. 5652–5657. DOI: 10.1002/2013gl057401. URL: https://doi.org/10.1002/2013gl057401.

Oglesby, D. (2008). "Rupture Termination and Jump on Parallel Offset Faults". In: *Bulletin of the Seismological Society of America* 98.1, pp. 440–447. DOI: 10.1785/0120070163. URL: https://doi.org/10.1785/0120070163.

Oglesby, D. D. (2005). "The Dynamics of Strike-Slip Step-Overs with Linking Dip-Slip Faults". In: *Bulletin of the Seismological Society of America* 95.5, pp. 1604–1622. DOI: 10.1785/0120050058. URL: https://doi.org/10.1785/0120050058.

Oskin, M. E. et al. (2012). "Near-Field Deformation from the El Mayor-Cucapah Earthquake Revealed by Differential LIDAR". In: *Science* 335.6069, pp. 702–705. DOI: 10.1126/science.1213778. URL: https://doi.org/10.1126/science.1213778.

Palmer, A. C. and J. R. Rice (1973). "The Growth of Slip Surfaces in the Progressive Failure of Over-Consolidated Clay". In: vol. 332. 1591. The Royal Society, pp. 527–548. DOI: 10.1098/rspa.1973.0040. URL: https://doi.org/10.1098/rspa.1973.0040.

Parsons, T. et al. (2012). "Possible Earthquake Rupture Connections on Mapped California Faults Ranked by Calculated Coulomb Linking Stresses". In: *Bulletin of the Seismological Society of America* 102.6, pp. 2667–2676. DOI: 10.1785/0120110349. URL: https://doi.org/10.1785/0120110349.

Pipping, Elias et al. (2016). "On the efficient and reliable numerical solution of rate-and-state friction problems". In: *Geophysical Journal International* 204.3, pp. 1858–1866. DOI: 10.1093/gji/ggv512. URL: https://doi.org/10.1093/gji/ggv512.

Poliakov, Alexei N. B., Renata Dmowska, and James R. Rice (2002). "Dynamic shear rupture interactions with fault bends and off-axis secondary faulting". In: *Journal of Geophysical Research: Solid Earth* 107.B11, ESE 6–1–ESE 6–18. DOI: 10.1029/2001jb000572. URL: https://doi.org/10.1029/2001jb000572.

Rajaure, S. et al. (2017). "Characterizing the Kathmandu Valley sediment response through strong motion recordings of the 2015 Gorkha earthquake sequence". In: *Tectonophysics* 714-715, pp. 146–157. DOI: 10.1016/j.tecto.2016.09.030. URL: https://doi.org/10.1016/j.tecto.2016.09.030.

Ranjith, K and J Rice (2001). "Slip dynamics at an interface between dissimilar materials". In: *Journal of the Mechanics and Physics of Solids* 49.2, pp. 341–361. DOI: 10.1016/s0022-5096(00)00029-6. URL: https://doi.org/10.1016/s0022-5096%2800%2900029-6.

Revenaugh, Justin and Thomas H. Jordan (1991). "Mantle layering fromScSreverberations: 1. Waveform inversion of zeroth-order reverberations". In: *Journal of Geophysical Research: Solid Earth* 96.B12, pp. 19749–19762. DOI: 10.1029/91jb01659. URL: https://doi.org/10.1029/91jb01659.

Rice, James R. (1993). "Spatio-temporal complexity of slip on a fault". In: *Journal of Geophysical Research* 98.B6, p. 9885. DOI: 10.1029/93jb00191. URL: https://doi.org/10.1029/93jb00191.

– (2006). "Heating and weakening of faults during earthquake slip". In: *Journal of Geophysical Research: Solid Earth* 111.B5, n/a–n/a. DOI: 10.1029/2005jb004006. URL: https://doi.org/10.1029/2005jb004006.

Rice, JR and A L_ Ruina (1983). "Stability of steady frictional slipping". In: *Journal of applied mechanics* 50.2, pp. 343–349.

Ripperger, J., P. M. Mai, and J.-P. Ampuero (2008). "Variability of Near-Field Ground Motion from Dynamic Earthquake Rupture Simulations". In: *Bulletin of the Seismological Society of America* 98.3, pp. 1207–1228. DOI: 10.1785/0120070076. URL: https://doi.org/10.1785/0120070076.

Rubin, A. M. and J.-P. Ampuero (2005). "Earthquake nucleation on (aging) rate and state faults". In: *Journal of Geophysical Research: Solid Earth* 110.B11. DOI: 10.1029/2005jb003686. URL: https://doi.org/10.1029/2005jb003686.

Ruina, Andy (1983). "Slip instability and state variable friction laws". In: *Journal of Geophysical Research: Solid Earth* 88.B12, pp. 10359–10370. DOI: 10.1029/jb088ib12p10359. URL: https://doi.org/10.1029/jb088ib12p10359.

Rundle, John B., W. Klein, and Susanna Gross (1999). "Physical Basis for Statistical Patterns in Complex Earthquake Populations: Models, Predictions and Tests". In: *Seismicity Patterns, their Statistical Significance and Physical Meaning*. Birkhäuser Basel, pp. 575–607. DOI: 10.1007/978-3-0348-8677-2_17. URL: https://doi.org/10.1007/978-3-0348-8677-2_17.

Rupakhety, R., S. Olafsson, and B. Halldorsson (2017). "The 2015 Mw 7.8 Gorkha Earthquake in Nepal and its aftershocks: analysis of strong ground motion". In: *Bulletin of Earthquake Engineering* 15.7, pp. 2587–2616. DOI: 10.1007/s10518-017-0084-z. URL: https://doi.org/10.1007/s10518-017-0084-z.

Ryan, Kenny J. and David D. Oglesby (2014). "Dynamically modeling fault step overs using various friction laws". In: *Journal of Geophysical Research: Solid Earth* 119.7, pp. 5814–5829. DOI: 10.1002/2014jb011151. URL: https://doi.org/10.1002/2014jb011151.

Saikia, Chandan K and DV Helmberger (1997). "Approximation of rupture directivity in regional phases using upgoing and downgoing wave fields". In: *Bulletin of the Seismological Society of America* 87.4, pp. 987–998.

Sato, M. et al. (2011). "Displacement Above the Hypocenter of the 2011 Tohoku-Oki Earthquake". In: *Science* 332.6036, pp. 1395–1395. DOI: 10.1126/science.1207401. URL: https://doi.org/10.1126/science.1207401.

Schmandt, Brandon and Eugene Humphreys (2010). "Complex subduction and small-scale convection revealed by body-wave tomography of the western United States upper mantle". In: *Earth and Planetary Science Letters* 297.3-4, pp. 435–445. DOI: 10.1016/j.epsl.2010.06.047. URL: https://doi.org/10.1016/j.epsl.2010.06.047.

Scholz, Christopher H, CA Aviles, and Steven G Wesnousky (1986). "Scaling differences between large interplate and intraplate earthquakes". In: *Bulletin of the Seismological Society of America* 76.1, pp. 65–70.

Shaw, Bruce E. and James H. Dieterich (2007). "Probabilities for jumping fault segment stepovers". In: *Geophysical Research Letters* 34.1. DOI: 10.1029/2006gl027980. URL: https://doi.org/10.1029/2006gl027980.

Shi, Zheqiang and Steven M. Day (2013). "Rupture dynamics and ground motion from 3-D rough-fault simulations". In: *Journal of Geophysical Research: Solid Earth* 118.3, pp. 1122–1141. DOI: 10.1002/jgrb.50094. URL: https://doi.org/10.1002/jgrb.50094.

Shibazaki, Bunichiro and Mitsuhiro Matsu'ura (1992). "Spontaneous processes for nucleation, dynamic propagation, and stop of earthquake rupture". In: *Geophysical Research Letters* 19.12, pp. 1189–1192. DOI: 10.1029/92gl01072. URL: https://doi.org/10.1029/92gl01072.

Sieh, K. et al. (1993). "Near-Field Investigations of the Landers Earthquake Sequence, April to July 1992". In: *Science* 260.5105, pp. 171–176. DOI: 10.1126/science.260.5105.171. URL: https://doi.org/10.1126/science.260.5105.171.

Simmons, N. A. et al. (2012). "LLNL-G3Dv3: Global P wave tomography model for improved regional and teleseismic travel time prediction". In: *Journal of Geophysical Research: Solid Earth* 117.B10. DOI: 10.1029/2012jb009525. URL: https://doi.org/10.1029/2012jb009525.

Simmons, N. A. et al. (2015). "Evidence for long-lived subduction of an ancient tectonic plate beneath the southern Indian Ocean". In: *Geophysical Research Letters* 42.21, pp. 9270–9278. DOI: 10.1002/2015gl066237. URL: https://doi.org/10.1002/2015gl066237.

Simons, M. et al. (2011). "The 2011 Magnitude 9.0 Tohoku-Oki Earthquake: Mosaicking the Megathrust from Seconds to Centuries". In: *Science* 332.6036, pp. 1421–1425. DOI: 10.1126/science.1206731. URL: https://doi.org/10.1126/science.1206731.

Stuart, William D. (1979). "Strain softening prior to two-dimensional strike slip earthquakes". In: *Journal of Geophysical Research* 84.B3, p. 1063. DOI: 10.1029/jb084ib03p01063. URL: https://doi.org/10.1029/jb084ib03p01063.

Stuart, William D. and Gerald M. Mavko (1979). "Earthquake instability on a strike-slip fault". In: *Journal of Geophysical Research* 84.B5, p. 2153. DOI: 10.1029/jb084ib05p02153. URL: https://doi.org/10.1029/jb084ib05p02153.

Sun, Daoyuan and Don Helmberger (2010). "Upper-mantle structures beneath USArray derived from waveform complexity". In: *Geophysical Journal International* 184.1, pp. 416–438. DOI: 10.1111/j.1365-246x.2010.04847.x. URL: https://doi.org/10.1111/j.1365-246x.2010.04847.x.

Sun, Daoyuan et al. (2016). "Major disruption of D" beneath Alaska". In: *Journal of Geophysical Research: Solid Earth* 121.5, pp. 3534–3556. DOI: 10.1002/2015jb012534. URL: https://doi.org/10.1002/2015jb012534.

Takai, Nobuo et al. (2016). "Strong ground motion in the Kathmandu Valley during the 2015 Gorkha, Nepal, earthquake". In: *Earth, Planets and Space* 68.1. DOI: 10.1186/s40623-016-0383-7. URL: https://doi.org/10.1186/s40623-016-0383-7.

Uenishi, Koji and James R. Rice (2003). "Universal nucleation length for slip-weakening rupture instability under nonuniform fault loading". In: *Journal of Geophysical Research: Solid Earth* 108.B1. DOI: 10.1029/2001jb001681. URL: https://doi.org/10.1029/2001jb001681.

Wald, David J and Thomas H Heaton (1994). "Spatial and temporal distribution of slip for the 1992 Landers, California, earthquake". In: *Bulletin of the Seismological Society of America* 84.3, pp. 668–691.

Wang, Tao, Justin Revenaugh, and Xiaodong Song (2014). "Two-dimensional/three-dimensional waveform modeling of subducting slab and transition zone beneath Northeast Asia". In: *Journal of Geophysical Research: Solid Earth* 119.6, pp. 4766–4786. DOI: 10.1002/2014jb011058. URL: https://doi.org/10.1002/2014jb011058.

Wei, Shengji et al. (2011). "Superficial simplicity of the 2010 El Mayor–Cucapah earthquake of Baja California in Mexico". In: *Nature Geoscience* 4.9, pp. 615–618. DOI: 10.1038/ngeo1213. URL: https://doi.org/10.1038/ngeo1213.

Wei, Shengji et al. (2012). "Locating earthquakes with surface waves and centroid moment tensor estimation". In: *Journal of Geophysical Research: Solid Earth* 117.B4, n/a–n/a. DOI: 10.1029/2011jb008501. URL: https://doi.org/10.1029/2011jb008501.

Wei, Shengji et al. (2013). "Rupture complexity of theMw8.3 sea of okhotsk earthquake: Rapid triggering of complementary earthquakes?" In: *Geophysical Research Letters* 40.19, pp. 5034–5039. DOI: 10.1002/grl.50977. URL: https://doi.org/10.1002/grl.50977.

Weng, Huihui and Hongfeng Yang (2017). "Seismogenic width controls aspect ratios of earthquake ruptures". In: *Geophysical Research Letters* 44.6, pp. 2725–2732. DOI: 10.1002/2016gl072168. URL: https://doi.org/10.1002/2016gl072168.

Wesnousky, S. G. and G. P. Biasi (2011). "The Length to Which an Earthquake Will Go to Rupture". In: *Bulletin of the Seismological Society of America* 101.4, pp. 1948–1950. DOI: 10.1785/0120110013. URL: https://doi.org/10.1785/0120110013.

Wesnousky, Steven G. (2006). "Predicting the endpoints of earthquake ruptures". In: *Nature* 444.7117, pp. 358–360. DOI: 10.1038/nature05275. URL: https://doi.org/10.1038/nature05275.

Xu, Xiwei et al. (2006). "Reevaluation of surface rupture parameters and faulting segmentation of the 2001 Kunlunshan earthquake (Mw7.8), northern Tibetan Plateau, China". In: *Journal of Geophysical Research: Solid Earth* 111.B5. DOI: 10.1029/2004jb003488. URL: https://doi.org/10.1029/2004jb003488.

Yagi, Yuji and Ryo Okuwaki (2015). "Integrated seismic source model of the 2015 Gorkha, Nepal, earthquake". In: *Geophysical Research Letters* 42.15, pp. 6229–6235. DOI: 10.1002/2015gl064995. URL: https://doi.org/10.1002/2015gl064995.

Yıkılmaz, M. B. et al. (2014). "Critical Jump Distance for Propagating Earthquake Ruptures Across Step-Overs". In: *Pure and Applied Geophysics* 172.8, pp. 2195–2201. DOI: 10.1007/s00024-014-0786-y. URL: https://doi.org/10.1007/s00024-014-0786-y.

Yue, Han, Thorne Lay, and Keith D. Koper (2012). "En échelon and orthogonal fault ruptures of the 11 April 2012 great intraplate earthquakes". In: *Nature* 490.7419, pp. 245–249. DOI: 10.1038/nature11492. URL: https://doi.org/10.1038/nature11492.

Yue, Han et al. (2017). "Depth varying rupture properties during the 2015 Mw 7.8 Gorkha (Nepal) earthquake". In: *Tectonophysics* 714-715, pp. 44–54. DOI: 10.1016/j.tecto.2016.07.005. URL: https://doi.org/10.1016/j.tecto.2016.07.005.

Zhan, Zhongwen, Donald V. Helmberger, and Dunzhu Li (2014a). "Imaging subducted slab structure beneath the Sea of Okhotsk with teleseismic waveforms". In: *Physics of the Earth and Planetary Interiors* 232, pp. 30–35. DOI: 10.1016/j.pepi.2014.03.008. URL: https://doi.org/10.1016/j.pepi.2014.03.008.

Zhan, Zhongwen et al. (2012). “Anomalously steep dips of earthquakes in the 2011 Tohoku-Oki source region and possible explanations”. In: *Earth and Planetary Science Letters* 353-354, pp. 121–133. DOI: 10.1016/j.epsl.2012.07.038. URL: https://doi.org/10.1016/j.epsl.2012.07.038.

Zhan, Z. et al. (2014b). “Supershear rupture in a Mw 6.7 aftershock of the 2013 Sea of Okhotsk earthquake”. In: *Science* 345.6193, pp. 204–207. DOI: 10.1126/science.1252717. URL: https://doi.org/10.1126/science.1252717.

Zhao, Dapeng, Akira Hasegawa, and Hiroo Kanamori (1994). “Deep structure of Japan subduction zone as derived from local, regional, and teleseismic events”. In: *Journal of Geophysical Research: Solid Earth* 99.B11, pp. 22313–22329. DOI: 10.1029/94jb01149. URL: https://doi.org/10.1029/94jb01149.

Zhou, Yu et al. (2016). “Mapping 3D fault geometry in earthquakes using high-resolution topography: Examples from the 2010 El Mayor-Cucapah (Mexico) and 2013 Balochistan (Pakistan) earthquakes”. In: *Geophysical Research Letters* 43.7, pp. 3134–3142. DOI: 10.1002/2016gl067899. URL: https://doi.org/10.1002/2016gl067899.

Zhu, Lupei and Donald V Helmberger (1996). “Advancement in source estimation techniques using broadband regional seismograms”. In: *Bulletin of the Seismological Society of America* 86.5, pp. 1634–1641.

Zuza, Andrew V. et al. (2017). “Spacing and strength of active continental strike-slip faults”. In: *Earth and Planetary Science Letters* 457, pp. 49–62. DOI: 10.1016/j.epsl.2016.09.041. URL: https://doi.org/10.1016/j.epsl.2016.09.041.